

**ANALYSIS, MODELING, AND DIAGNOSTICS OF ADJACENT AND  
NONADJACENT BROKEN ROTOR BARS IN SQUIRREL-CAGE  
INDUCTION MACHINES**

by

Gennadi Y. Sizov, B.S.E.E.

A Thesis Submitted to the Faculty  
of the Graduate School,  
Marquette University,  
in Partial Fulfillment of  
the Requirements for  
the Degree of  
Master of Science in Electrical and Computer Engineering

Milwaukee, Wisconsin  
December, 2007

## ABSTRACT

---

**I**N this thesis, faults associated with squirrel-cage rotor structures will be considered. More specifically, diagnostics of adjacent and nonadjacent squirrel-cage rotor bar breakages will be addressed. Effects of such faults on machine performance will be studied through a number of modeling approaches. Namely, an example of a simple 8-bar squirrel-cage induction machine will be used to visualize the effects of both adjacent and nonadjacent rotor bar faults on the magnetic field distribution in the induction machine. Then, more sophisticated models such as the magnetic equivalent circuit, and time-stepping finite element models of a case-study 5-hp induction machine will be developed. These models will be used to verify the assumptions used in the simple 8-bar example as well as to provide a more detailed picture of the fault effects on the motor performance. A number of both adjacent and nonadjacent fault scenarios will be considered. It will be shown that some nonadjacent rotor bar breakages may result in the masking of the commonly used indices of fault signals, hence, leading to possible misdiagnosis of the machine. It will also be shown that secondary effects that appear during such nonadjacent rotor faults can be utilized for purposes of fault identification using conventional rotor fault diagnostic approaches with modified indices. Moreover, a new rotor fault diagnostics technique based on the vibration signal obtained using a low-cost piezoelectric vibration sensor will be introduced. This technique will be used for successful diagnostics of both adjacent and nonadjacent squirrel-cage rotor faults. Both of these findings show a good deal of promise in practical applications.

## ACKNOWLEDGMENT

---

I wish to express special gratitude to my family members and friends for their encouragement and support throughout this endeavor. I would like to thank my wife, Olga, for her love and belief in my skills. Moreover, I would like to dedicate this work to the memory of my mother, Irina, who enriched my life with love and care that only a mother can provide; may she rest in peace.

I would like to express my sincere and deep appreciation to my advisor, Dr. Nabeel A.O. Demerdash, for his never ending support, encouragement, and valuable discussions. I should acknowledge members of the examination committee, Dr. Edwin E. Yaz, and Dr. Behrooz Mirafzal, for their careful review of this work and valuable feedback, as well as useful suggestions that helped to make this work complete.

I would also like to acknowledge United States Department of Education Graduate Assistance in Areas of National Need (GAANN) Doctoral Fellowship Program, award number P200A010104, for providing the opportunity to carryout this work.

Finally, I wish to express special thanks to my laboratory teammates and friends, Chia-Chou Yeh, Ahmed Sayed-Ahmed, and Anushree Kadaba, for their discussions, and suggestions about my research topic. However, more importantly, I would like to thank them for their motivation throughout this work.

## TABLE OF CONTENTS

---

List of Figures .....	v
List of Tables .....	xi
 <b>Chapter 1: Introduction</b>	
1.1 Background .....	1
1.2 Literature Review .....	3
1.2.1 Bearing Faults .....	3
1.2.2 Stator Faults .....	7
1.2.3 Rotor Faults .....	9
1.3 Thesis Contribution .....	10
1.4 Thesis Organization .....	11
 <b>Chapter 2: Rotor Fault Analysis</b>	
2.1 Introduction .....	12
2.2 Rotor with One Broken Bar .....	14
2.3 Rotor with Nonadjacent Bar Breakages .....	17
2.3.1 Half Pole-Pitch .....	17
2.3.2 One Pole-Pitch .....	19
 <b>Chapter 3: Induction Machine Modeling</b>	
3.1 Introduction .....	22
3.2 Magnetic Equivalent Circuit Model .....	25
3.3 Finite Element Model .....	54
3.4 Model Validation .....	58
 <b>Chapter 4: Rotor Fault Diagnostics</b>	
4.1 Introduction .....	63
4.2 Motor Current Signature Analysis (MCSA) .....	63
4.3 Magnetic Field Pendulous Oscillation (MFPO) .....	67

<b>Chapter 5: Application of Piezoelectric Sensors to Motor Fault Diagnostics</b>	
5.1 Introduction .....	75
5.2 Polyvinylidene Fluoride (PVDF) Piezoelectric Material .....	77
5.3 Motor Fault Diagnostics Using Piezoelectric Vibration Sensor .....	82
<b>Chapter 6: Experimental and Simulation Results</b>	
6.1 Introduction .....	90
6.2 Rotor Bar Breakages Separated by Half Pole-Pitch .....	90
6.2.1 Two Broken Bars Separated by Half Pole-Pitch .....	91
6.2.2 $N$ Broken Bars Separated by Half Pole-Pitch .....	96
6.3 Rotor Bar Breakages Separated by One Pole-Pitch .....	99
6.3.1 Two Broken Bars Separated by One Pole-Pitch .....	99
6.3.2 $N$ Broken Bars Separated by One Pole-Pitch .....	102
<b>Chapter 7: Conclusions</b>	
7.1 Summary and Conclusions .....	104
7.2 Recommendations for Future Work .....	105
<b>References</b> .....	106
<b>Appendix: MEC Parameter Calculation</b> .....	117

## LIST OF FIGURES

---

1-1	Induction motor fault occurrence data .....	3
1-2	Main bearing failure mechanisms .....	4
1-3	Bearing raceway showing signs of pitting due to bearing currents .....	6
1-4	Bearing raceway with the signs of fluting .....	6
2-1	Simple 8-bar squirrel-cage rotor (Healthy) .....	13
2-2	Rotor current sheet (Healthy) .....	13
2-3	Simple 8-bar squirrel-cage rotor (Broken bar at location 4) .....	16
2-4	Rotor current sheet (Broken bar at location 4) .....	16
2-5	Simple 8-bar squirrel-cage rotor (Broken bars at locations 2 and 4) .....	18
2-6	Rotor current sheet (Broken bars at locations 2 and 4) .....	19
2-7	Simple 8-bar squirrel-cage rotor (Broken bars at locations 4 and 8) .....	20
2-8	Rotor current sheet (Broken bars at locations 4 and 8) .....	20
3-1	Simple magnetic device .....	27
3-2	Magnetic equivalent circuit representation of a simple magnetic device .....	29
3-3	Cross-section of the 5-hp squirrel-cage induction machine .....	30
3-4	Stator winding layout of the 5-hp squirrel-cage induction machine .....	30
3-5	Stator slot of the 5-hp induction machine .....	31
3-6	Rotor slot of the 5-hp induction machine .....	31
3-7	MEC representation of a double-layer stator winding .....	33
3-8	Simplified MEC representation of a double-layer stator winding .....	33
3-9	MEC representation of a rotor slot (with deep-bar effect) .....	36
3-10	Simplified MEC representation of a rotor slot (without deep-bar effect) .....	36
3-11	MEC representation of the 5-hp induction machine (with closed rotor slot) .....	38
3-12	Block diagram of a squirrel-cage induction machine MEC model (without Mechanical System) .....	45
3-13	Stator winding layout and mmf distribution of phases a, b, and c over one pole span .....	46
3-14	Rotor squirrel-cage showing rotor loop currents and teeth fluxes .....	49
3-15	Block diagram of a complete squirrel-cage induction machine MEC model .....	53

3-16	Cross-section of the 5-hp squirrel-cage induction machine with finite element grid .....	58
3-17	Time-domain profile of phase-a current (MEC) .....	60
3-18	Frequency spectrum profile of phase-a current (MEC) .....	60
3-19	Time-domain profile of phase-a current (TSFE) .....	60
3-20	Frequency spectrum profile of phase-a current (TSFE) .....	60
3-21	Time-domain profile of phase-a current (Experimental Test) .....	60
3-22	Frequency spectrum profile of phase-a current (Experimental Test) .....	60
3-23	Pendulous Oscillation, $\Delta\delta_1=1.5^\circ$ (MEC) .....	61
3-24	Pendulous Oscillation, $\Delta\delta_1=1.8^\circ$ (TSFE) .....	62
3-25	Pendulous Oscillation, $\Delta\delta_1=1.6^\circ$ (Experimental Test) .....	62
4-1	Stator line current spectrum of 5-hp induction machine under healthy full-load conditions (from Experimental Test) .....	65
4-2	Stator line current spectrum of 5-hp induction machine under healthy full-load conditions (from MEC Simulation) .....	65
4-3	Stator line current spectrum of 5-hp induction machine under one broken bar full-load conditions (from Experimental Test) .....	65
4-4	Stator line current spectrum of 5-hp induction machine under one broken bar full-load conditions (from MEC Simulation) .....	65
4-5	Lower Side-Band component versus number of broken bars under full-load conditions (from Experimental Tests) .....	66
4-6	Lower Side-Band component versus number of broken bars under full-load conditions (from MEC Simulations) .....	66
4-7	Simple 8-bar squirrel-cage rotor (Broken bar at location 4) .....	70
4-8	Rotor current sheet (Broken bar at location 4) .....	70
4-9	Pendulous Oscillation time-domain profile (One broken bar, full-load, MEC Simulation) .....	71
4-10	Rotor current sheet at time instant $t_1$ .....	72
4-11	Rotor current sheet at time instant $t_2$ .....	72
4-12	Rotor current sheet at time instant $t_3$ .....	72
4-13	Rotor current sheet at time instant $t_4$ .....	72
4-14	Rotor current sheet at time instant $t_5$ .....	72

4-15	Rotor current sheet at time instant $t_6$ .....	72
4-16	Rotor current sheet at time instant $t_7$ .....	72
4-17	Rotor current sheet at time instant $t_8$ .....	72
4-18	Swing angle, $\Delta \delta_l$ , versus number of broken bars under full-load conditions (from Experimental Tests) .....	74
4-19	Swing angle, $\Delta \delta_l$ , versus number of broken bars under full-load conditions (from MEC Simulations) .....	74
5-1	Piezoelectric (PVDF) film showing mechanical and electrical axes .....	77
5-2	Piezoelectric (PVDF) film showing electrodes .....	77
5-3	Electric equivalent circuit model of piezoelectric material .....	78
5-4	Electric equivalent circuit model of piezoelectric material connected to a practical circuit .....	79
5-5	High input impedance unity gain buffer (voltage follower) amplifier .....	80
5-6	Piezoelectric PVDF film sensor operated as vibrating beam/cantilever .....	80
5-7	Piezoelectric PVDF film sensor operated in compression mode along axis-3 ....	81
5-8	Experimental setup showing the location of PVDF sensor .....	83
5-9	Vibration signal of 5-hp induction machine under healthy full-load conditions (30Nm, 1164r/min, from Experimental Test) .....	87
5-10	Spectrum of vibration signal of 5-hp induction machine under healthy full-load conditions (30Nm, 1164r/min, from Experimental Test) .....	87
5-11	Vibration signal of 5-hp induction machine under one broken bar full-load conditions (30Nm, 1164r/min, from Experimental Test) .....	88
5-12	Spectrum of vibration signal of 5-hp induction machine under one broken bar full-load conditions (30Nm, 1164r/min, from Experimental Test) .....	88
5-13	Spectrum of vibration signal of 5-hp induction machine under four broken bar full-load conditions (30Nm, 1155r/min, from Experimental Test) .....	89
6-1	Cross-section of a case study 5-hp squirrel-cage induction machine showing locations of nonadjacent bar breakages separated by half pole-pitch, $90^\circ$ e .....	91
6-2	Current frequency spectrum (MCSA) under conditions of two broken bars separated by half pole-pitch, $90^\circ$ electrical (from Experimental Test) .....	92
6-3	Current frequency spectrum (MCSA) under healthy conditions (from Experimental Test) .....	92

6-4	Current frequency spectrum (MCSA) under conditions of two adjacent broken bars (from Experimental Test) .....	92
6-5	Pendulous Oscillation time-domain profile (MFPO) under conditions of two broken bars half pole-pitch, 90° electrical (from Experimental Test) .....	93
6-6	Pendulous Oscillation time-domain profile (MFPO) under healthy conditions (from Experimental Test) .....	93
6-7	Pendulous Oscillation time-domain profile (MFPO) under conditions of two adjacent broken bars (from Experimental Test) .....	93
6-8	Current frequency spectrum (MCSA) two broken bars separated by half pole-pitch, 90° electrical (from Experimental Test) .....	94
6-9	Current frequency spectrum (MCSA) under healthy conditions (from Experimental Test) .....	94
6-10	Current frequency spectrum (MCSA) under conditions of two adjacent broken bars (from Experimental Test) .....	94
6-11	Spectrum of vibration signal of 5-hp induction machine under conditions of two broken bars separated by half pole-pitch, 90° electrical (from Experimental Test) .....	95
6-12	Spectrum of vibration signal of 5-hp induction machine under healthy conditions (from Experimental Test) .....	95
6-13	Spectrum of vibration signal of 5-hp induction machine under one broken bar conditions (from Experimental Test) .....	95
6-14	Cross-section of a case study 5-hp squirrel-cage induction machine showing locations of nonadjacent bar breakages separated by half pole-pitch (90°e) $N=3$ .....	96
6-15	Current frequency spectrum (MCSA) under conditions of three broken bars separated by half pole-pitch, 90° electrical, $N=3$ , (from Experimental Test) .....	97
6-16	Current frequency spectrum (MCSA) under conditions of one broken bar (from Experimental Test) .....	97
6-17	MFPO under conditions of three broken bars half pole-pitch, 90° electrical, $N=3$ , (from Experimental Test) .....	98
6-18	MFPO under conditions of one broken bar (from Experimental Test) .....	98

6-19	Spectrum of vibration signal of 5-hp induction machine under conditions of three broken bars separated by half pole-pitch, $90^\circ$ electrical, $N=3$ , (from Experimental Test) .....	99
6-20	Spectrum of vibration signal of 5-hp induction machine under one broken bar conditions (from Experimental Test) .....	99
6-21	Cross-section of a case study 5-hp squirrel-cage induction machine showing locations of nonadjacent bar breakages separated by one pole-pitch ( $180^\circ$ e) $N=3$ .....	100
6-22	Current frequency spectrum (MCSA) under conditions of two broken bars separated by one pole-pitch, $180^\circ$ electrical (from Experimental Test) .....	101
6-23	Current frequency spectrum (MCSA) under conditions of two adjacent broken bars (from Experimental Test) .....	101
6-24	MFPO under conditions of three broken bars one pole-pitch, $180^\circ$ electrical (from Experimental Test) .....	101
6-25	MFPO under conditions of two adjacent broken bars (from Experimental Test) ..	101
6-26	Current frequency spectrum (MCSA) under conditions of three broken bars separated by one pole-pitch, $180^\circ$ electrical, $N=3$ , (from MEC Simulation) .....	103
6-27	Current frequency spectrum (MCSA) under conditions of three adjacent broken bars (from MEC Simulation) .....	103
6-28	MFPO under conditions of three broken bars one pole-pitch, $180^\circ$ electrical, $N=3$ , (from MEC Simulation) .....	103
6-29	MFPO under conditions of three adjacent broken bars (from MEC Simulation) ..	103
A-1	Rotor slot cross-section .....	117
A-2	Stator and rotor teeth relative position and overlap area .....	118
A-3	Air gap permeance for a pair of stator and rotor teeth .....	119
A-4	Smoothed air gap permeance for a pair of stator and rotor teeth .....	119
A-5	Stator slot with dimensions .....	120
A-6	Stator tooth with various reluctances and permeances .....	120
A-7	Rectangular permeance block .....	121
A-8	Trapezoidal permeance block .....	121

## LIST OF TABLES

---

3-1	Steady-state performance characteristics (MEC, TSFE, and Test) .....	59
3-2	Values of lower side-band component (LSB) and swing angle, $\Delta\delta_l$ , under conditions of one broken rotor bar .....	62
4-1	LSB component under full-load conditions (from Experimental Tests and MEC Simulations) .....	66
4-2	Swing angle, $\Delta\delta_l$ , under full-load conditions (from Experimental Tests and MEC Simulations) .....	74
5-1	Piezoelectric PVDF sensor parameters .....	81
A-1	MEC model parameters of the 5-hp induction motor .....	122

# CHAPTER 1: INTRODUCTION

---

## 1.1 BACKGROUND

**I**NDUCTION MACHINES are perhaps the most popular type of electric machines used in industry today. Since the discovery of the rotating magnetic field phenomenon in 1880s by Nikola Tesla, first described in [1], and its application to ac machinery, and in particular to the induction machine, initially presented in [2], the design of induction machines has been revisited by researchers and engineers, and improved numerous times. The design of the induction machine has been significantly improved in terms of both reliability and cost with the invention of the solid short-circuited rotor structure, also known as the squirrel-cage rotor. Modern squirrel-cage induction machines possess a rugged and relatively simple design, which results in reduced manufacturing and maintenance costs. These squirrel-cage induction machines are now widely used and are the most common type of induction machines found in industry today.

Moreover, due to recent developments in power semiconductor technology induction machines are being utilized in applications that were originally out of reach due to the rather complicated and costly methods that were designed for control of induction machines' speed and torque production. Induction machines supplied by modern semiconductor ac drives have

replaced conventional dc machines in most of applications that have originally been dominated by systems of dc machines. Among other benefits, when compared to conventional brush-type dc machines, induction machines offer a higher degree of reliability, which results in the reduction of overall maintenance costs. Today, induction machines are being utilized in a variety of diverse industries, ranging from mining, process manufacturing, automation applications, heating and air conditioning, transportation, aerospace and marine propulsion applications to the health care industry.

Although modern induction machine possesses relatively high degree of reliability, when compared to the conventional brush-type dc machine, being a practical device with parts and components it is still prone to failures. These failures are commonly divided, based on the main machine components, into three major groups, namely, bearing faults, stator faults, and rotor faults [3-5]. About forty percent of faults associated with induction machines are due to the bearing failures, see the pie-chart of Figure 1-1. This is according to a number of independent studies on induction machine failure statistical data previously reported in the literature [3-5]. Meanwhile, faults associated with stators account for another forty percent of induction machine failures [3-5]. It should be mentioned that, although mechanisms of stator and bearing failures may differ slightly between different types of electric machines, these types of faults are known to be a common problem in other types of electric machines, namely, synchronous, brushless dc, reluctance, etc. Furthermore, failures associated with rotors account for approximately ten percent of induction machine failures [3-5]. However, unlike bearing and stator faults these faults are specific to squirrel-cage induction machines. Again, fault occurrence data presented in [3-5] is summarized in Figure 1-1.

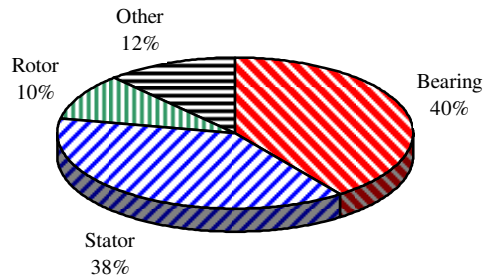


**Figure 1-1.** Induction motor fault occurrence data, [3-5].

The fourth category depicted in Figure 1-1 and entitled “Other” accounts for the faults associated with failures of the external components of the motor-load system or the failures not considered in the studies performed in [3-5].

## 1.2 LITERATURE REVIEW

In this section a more detailed literature review describing some of the causes and mechanisms as well as some diagnostic techniques of the most common induction motor failures will be presented. More specifically, an explanation of the mechanisms of the various failures will be presented and supported through previously performed studies on bearing, stator, and squirrel-cage rotor faults.

### 1.2.1 BEARING FAULTS

Typical bearings used in electric machinery consist of three major components, namely, a set of balls or rollers, raceways, and lubricant. As can be seen from Figure 1-2, there are generally three mechanisms that result in the accelerated failure of a bearing. First, mechanical stresses that result in metal fatigue failures. These failures can result from both normal operating conditions,

as well as abnormal conditions, such as motor-load shaft misalignment and mechanically unbalanced loads, which accelerate the deterioration of the bearings through localized fatigue phenomenon known as flaking [6].

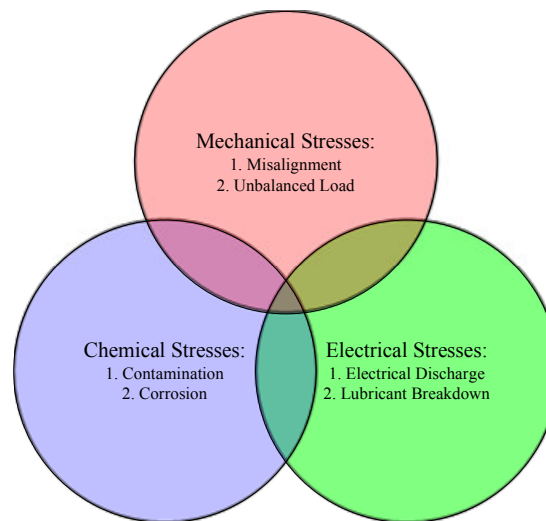


**Figure 1-2.** Main bearing failure mechanisms.

Mechanical stresses can be aggravated through chemical contamination of lubricants, which are used to reduce friction losses between rollers and raceways. Lubricant contamination and bearing corrosion reduce the lifetime of the bearing because of the harsh environments present in most industrial settings. Foreign particles, such as industrial dust and dirt, commonly present in industrial settings may pollute the bearing lubricant resulting in increased wear of bearing's rollers and raceways [6]. In addition, bearing corrosion can be accelerated in the presence of moisture, acids, and other contaminants, which are commonly present in such industrial environments.

Electrical transients are yet another major source of stresses that causes an accelerated time to failure of the bearings used in rotating electric machinery. There are in general two sources of electrical stresses on bearings in induction machines. First, is a low frequency bearing current, typically on the order of the supply fundamental component frequency, produced as a result of a time-varying flux encircling the shaft. This flux is produced by magnetic asymmetries

which are commonly present in such machines [8]. The induced low frequency bearing current may result in excessive bearing heating as well as some possible electrical discharge through the lubricant, which damages both the lubricant and the raceways. The existence of this phenomenon has been well known and documented in previous studies [9-11]. Another source of electrical stresses on the bearings is associated with modern ac adjustable speed drive (ASD) technology. More specifically, high frequency pulse-width modulated (PWM) voltages produced by inverter circuits in such ASDs may induce so-called common-mode or zero-sequence (non-fundamental frequency) ac currents some of which pass through the bearings. There are two sources of the so-called common-mode current in an induction machine supplied by an ac drive. First, the class of three-phase six-switch bridge inverters commonly used in ac drive systems is by itself a source of the common-mode voltage. In other words, in case when an inverter is supplying a wye-connected induction machine, the voltage at the neutral of the machine is not zero, but rather is modulated at the switching frequency of the inverter. This neutral voltage may excite parasitic capacitances between the stator winding and the rotor resulting in the rotor shaft being at a potential other than zero with respect to the motor frame. Another major source of common-mode currents in the induction machines supplied by ac drives became more evident with the recent improvement in the semiconductor devices, such as IGBTs and power MOSFETs, used as switches in modern power electronic applications. Modern devices are capable of switching higher voltages at higher speeds, hence, reducing the switching losses and improving efficiency. This improvement, however, has a major flaw in the sense that it leads to higher  $dv/dt$  rates, hence, exciting any parasitic capacitances, which may be present in the path of the signal. Again, this may result in the increase of the energy transferred to the rotor structure through the capacitive coupling between the stator winding and the rotor surface, hence, leading to possible electrical discharge in the form of arching between bearing rollers and raceways. Arching

produced as the result of electrical discharges between the rollers and the raceways results in the pitting of the bearing raceways, which in turn, in the long run, will result in the phenomenon commonly referred to as fluting [12-16]. This effect of bearing raceway pitting, which results from sudden electrical discharges, is shown in Figure 1-3, the resulting raceway with fluting is depicted in Figure 1-4.

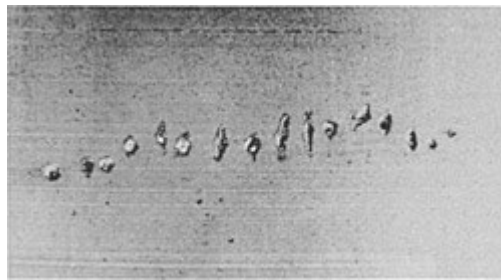


**Figure 1-3.** Bearing raceway showing signs of pitting due to bearing currents, [14].



**Figure 1-4.** Bearing raceway with the signs of fluting, [15].

Moreover, arching that takes place in the bearing chemically deteriorates lubricating properties of the lubricant, which provides the dielectric medium between the rollers and the raceways during the electrical discharge [15], [16]. Therefore, reducing the quality of the lubrication and decreasing the lifetime of the bearing.

Vibration signals are frequently used to diagnose bearing failures [7]. Specific frequency components in the vibration signal can be attributed to specific modes of bearing failures. These frequency components can be deduced from some basic bearing parameters, such as, number of rolling elements, diameter of rolling elements, bearing diameter, etc [7]. Another common approach to bearing fault identification is through the so-called sensorless approach [6]. Here, the vibration signal is detected through the motor currents without the need to install extra vibration sensors, hence, the name sensorless vibration detection. In this method, specific frequency components in the current spectrum can be attributed to the specific bearing problems. Again, similar to the previous approach some prior knowledge of the geometry of the bearing may be required in order to successfully diagnose the bearing [6].

### 1.2.2 STATOR FAULTS

Similar to induction motor bearings, stator windings are subject to electrical, mechanical, and chemical stresses that may result in accelerated winding insulation failures. As mentioned above, stator winding failures account for approximately forty percent of all failures associated with induction machines. Therefore, this resulted in considerable interest among researchers as to the mechanisms behind such stator winding failures [17-20]. Winding insulation is one of the weakest components of the stator winding. Accelerated insulation failures typically result from: mechanical vibrations, thermal and electrical overloading, voltage surges produced by ac drives, as well as chemical contaminants that may interfere with the dielectric properties of the insulating material [17].

Typically, insulation failures can be categorized into three subcategories, namely, inter-turn, phase-to-ground, and phase-to-phase faults. In the case when the motor is supplied by an ac drive the inter-turn insulation failure usually precedes a more serious phase-to-phase or phase-to-

ground fault condition [17]. Moreover, inter-turn faults are more likely to occur in the first few turns of a phase winding. This is because of the higher turn-to-turn voltage gradient in the first few turns of the stator phase winding [18]. In other words, the insulation between the turns in the beginning of the winding is subjected to higher dielectric stresses, since it is responsible for absorption of the initial voltage surge that has a relatively fast rise time, and hence a very high  $dv/dt$  [19]. Inter-turn insulation failure leads to high values of inter-turn circulating short-circuit currents that results in excessive, localized heating, which further damages the winding eventually leading to a complete winding failure.

There are numerous stator winding fault detection and condition monitoring techniques described in the literature [17], [22-31]. Furthermore, stator winding diagnostic techniques can be divided into two major classes, namely, offline insulation diagnostics [17], [22], [23], when the machine is removed from service, and online condition monitoring, where the machine remains in operation and its condition is continuously evaluated [25-30]. The offline diagnostics techniques range from the simplest resistance measurements to more sophisticated high potential and partial discharge methods [17]. Another offline diagnostic technique, which needs to be highlighted, considers the transient produced by the machine under the conditions of disconnecting the supply from the motor terminals [24]. Meanwhile, the online diagnostic methods are based on motor current signature analysis, presented in [25], symmetrical components technique, described in [23], pendulous oscillation method, developed in [27], as well as a number of other techniques employing advanced signal processing concepts, see [28], have been developed. It should be mentioned that other techniques employing specially designed search coils which allow the diagnosing of stator faults have also been proposed in [31].

### 1.2.3 ROTOR FAULTS

In general, there are three major types of faults that can be associated with the squirrel-cage rotor structures, namely, inter-laminar currents, sometimes referred to as inter-bar currents caused by shorts through the rotor core laminations, rotor end-ring connector breakages, and rotor bar breakages. These faults may result from a wide variety of stresses as well as manufacturing defects [32-34]. Squirrel-cage rotor structures are subject to harsh environments both electrically, and mechanically. Frequent overloading, both thermal and electrical, as well as excessive vibrations due to supply voltage unbalances, load variation, and frequent starting transients may result in the accelerated failure of squirrel-cage rotor bars and other structural components [33].

Inter-laminar currents result from the damage to the lamination insulation coating either during the manufacturing process or during the operation of the motor. These inter-laminar currents typically result in excessive rotor heating, which may in turn lead to a rise in the overall motor temperature and, hence, stress other motor components, such as armature winding insulation and motor bearings. Moreover, during normal motor operation inter-laminar currents may account for as much as one third of all stray load losses of the machine, hence, resulting in reduced efficiency [35], [36].

Cracked or broken squirrel-cage bar or end-ring connector may result from frequent motor starting, thermal and electrical overloading, as well as excessive motor vibrations. These faults result in the reduced performance of the machine and may lead to the propagation of the fault, which in turn will result in a complete motor failure. Moreover, these faults produce undesired torque oscillations (pulsations) that may result in undesired effects on the mechanical load, as well as, produce undesired vibrations that may further stress other motor and load components [37].

Spectrum analysis of induction machine line currents, also known as motor current signature analysis (MCSA), is one of the most commonly used rotor fault diagnostic techniques [38-40]. In this technique side-bands adjacent to the supply fundamental frequency component are used to diagnose the extent of the fault. This technique was improved through the application of more advanced signal processing techniques in [41], [42]. A so-called magnetic field pendulous oscillation technique, where time-domain values of motor line currents and voltages are used to generate the corresponding space-vectors and the oscillation of the angle between these space-vectors is used as the fault index, has been introduced in [43-46]. Model reference fault diagnostic techniques, such as the Vienna Monitoring Method, have been described in [47], [48]. Other techniques that use external search coils [49], [50], and air-gap torque profile [51], [52] to diagnose the health of a squirrel-cage rotor have also been successfully described in the literature.

### 1.3 THESIS CONTRIBUTION

In this thesis, faults associated with the rotor of an induction machine will be considered. More specifically, effects of adjacent and nonadjacent bar breakages on rotor fault diagnostics in squirrel-cage induction machines will be studied. It will be shown that some nonadjacent bar breakages may result in the masking of the commonly used fault indices [38-42], [43-46] and, hence, this may lead to possible misdiagnosis of the machine. A discussion of the possible scenarios of these breakages as well as some conclusions regarding the types of squirrel-cage induction machines (number of poles, number of squirrel-cage bars, etc.) that may be more prone to these, nonadjacent types of failures will be presented. This discussion will be supported through both simulation and experimental results. Moreover, the suitability of a simple piezoelectric vibration sensor for motor fault diagnostics will be considered. The major benefit of

a piezoelectric vibration sensor is the fact that it does not require an extra power supply and, hence, eliminates the need and extra costs of extra power supplies and associated wiring. Moreover, piezoelectric type vibration sensors provide excellent sensitivity as well as very high bandwidth.

#### 1.4 THESIS ORGANIZATION

Including this introductory chapter, this thesis is organized in seven chapters. In the second chapter, some basic considerations of squirrel-cage broken-bar faults will be presented. More specifically, a simple two-pole eight-bar squirrel-cage induction machine, used before in [43-46] for analysis of adjacent broken bars, will be used to visualize the effects of bar breakages on the motor magnetic field. Three fault scenarios will be considered, namely, adjacent bar breakages, nonadjacent bar breakages separated by one pole pitch, and nonadjacent bar breakages separated by half pole pitch. It will be shown that some nonadjacent broken-bar patterns may result in the possible masking of such faults. In Chapter 3, more sophisticated rotor fault modeling approaches will be presented. A time-stepping finite element induction motor model of a 6-pole, 5-hp machine will be used to verify the simple analysis presented in Chapter 2. Also, a suitability of a magnetic equivalent circuit model of the same 5-hp motor for emulation of fault conditions presented in Chapter 2 will be considered. In Chapter 4, two previously developed fault diagnostics techniques, described in [38-40], [43-46], will be reviewed and their application to adjacent rotor fault diagnostics will be discussed. In Chapter 5, a simple piezoelectric vibration sensor will be used to diagnose rotor faults. In Chapter 6, the simulation and experimental results of nonadjacent rotor faults, as well as the corresponding analysis and discussion of these results will be presented. Finally, in Chapter 7 conclusions and recommendations will be presented.

## CHAPTER 2: ROTOR FAULT ANALYSIS

---

### 2.1 INTRODUCTION

IN this chapter a very simple minded qualitative analysis of the effects of both adjacent and nonadjacent bar breakages on the magnetic field distribution of the induction machine will be presented. Consider a simple 2-pole induction machine with a squirrel-cage rotor shown in Figure 2-1. For simplicity of argument an 8-bar squirrel-cage design is utilized in this analysis. Also, shown in Figure 2-1 are the axes of the rotor current sheet represented by the rotating rotor current sheet vector,  $\vec{I}_{cr}$ , and the rotor magnetomotive force represented by the rotating rotor mmf vector,  $\vec{\mathcal{F}}_{mr}$ , in ampere-turns per pole. Depicted in Figure 2-2 is the current sheet produced by the individual squirrel-cage bar currents. This current sheet moves in space at synchronous speed,  $\omega_{syn}$ , whereas the rotor is moving at the rotor speed,  $\omega_r$ . Hence, the relative speed between the rotor current sheet and the squirrel-cage is equal to the slip speed. Accordingly, Figures 2-1 and 2-2 provide a snap-shot view of the current sheet and the rotor mmf position relative to the squirrel-cage at a given time instant. As can be seen from Figure 2-2, the current sheet axis is aligned with two bars carrying maximum positive and negative currents, at locations 3 and 7, whereas the rotor mmf axis, which has the same orientation as the rotor mmf vector,  $\vec{\mathcal{F}}_{mr}$ , is ninety degrees behind the current sheet axis and is aligned with the bars carrying zero current, at locations 1 and 5, respectively.

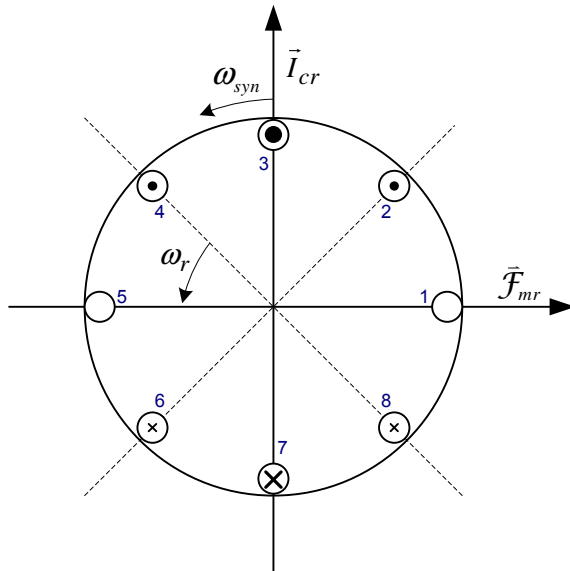


Figure 2-1. Simple 8-bar squirrel-cage rotor (Healthy).

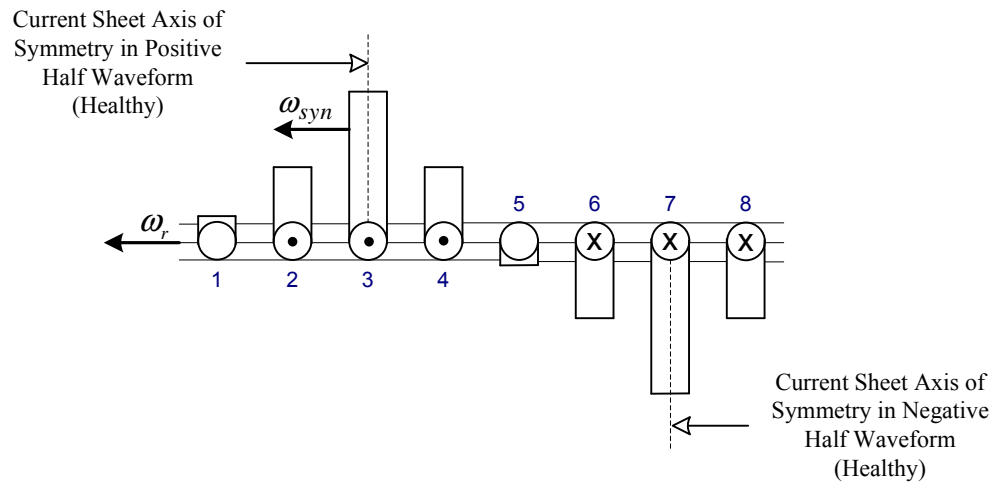


Figure 2-2. Rotor current sheet (Healthy).

There will be two simplifying assumptions used throughout this chapter. First, the bar currents are sinusoidally time-varying, resulting in a sinusoidally space-distributed current sheet. Second, there will be no axial flux produced as a result of a bar breakage fault in the machine. In other words, the magnetic field is strictly two-dimensional, which means that the currents out of the bars and into the bars must sum to zero. This assumption stems directly from Gauss's Law for magnetism expressed as follows:

$$\oint_{\text{surface}} \vec{B}_r \cdot d\vec{A} = 0 \quad (2.1)$$

where,  $\vec{B}_r$ , is the radial mid-airgap flux density vector and,  $d\vec{A}$  is the vector of differential surface area at the mid-airgap. For this squirrel-cage rotor (2.1) can be rewritten as follows:

$$\oint_{\text{surface}} \vec{B}_r \cdot d\vec{A} = \mu_0 \oint_{\text{surface}} \frac{\vec{F}_{mr}}{h_g} \cdot d\vec{A} = 0 \quad (2.2)$$

where,  $h_g$ , is the airgap height. The expression provided in (2.2) can also be written using

Ampere's Law, where the magnetic field produced by the rotor,  $\vec{H}_r = \frac{\vec{F}_{mr}}{h_g}$ , is integrated over

closed path represented by a circle at mid-airgap radius as follows [46]:

$$\oint_{\text{surface}} \vec{B}_r \cdot d\vec{A} = \mu_0 \oint_{\text{surface}} \frac{\vec{F}_{mr}}{h_g} \cdot d\vec{A} = \mu_0 \oint_{\text{surface}} \frac{\sum (NI_{bar}) \hat{r}}{2h_g} \cdot (dA) \hat{r} = 0 \quad (2.3)$$

where,  $N$ , is the number of rotor turns, which is equal to one per bar in a squirrel-cage rotor, and  $I_{bar}$  are the currents carried by each of the rotor bars. That is, the number of rotor current loops is equal to the number of rotor bars in a squirrel-cage rotor.

## 2.2 ROTOR WITH ONE BROKEN BAR

Here, the effects of one broken bar on the current sheet and rotor mmf are considered. As one can see from Figure 2-3 there are four possible locations 1, 3, 5, and 7 where bar breakage will not result in any dislocation of the current sheet axis and hence will not produce a rotor mmf reorientation. When the broken bar reaches location 1 or 5 it does not result in any shift of the current sheet axis because the current that is supposed to be carried by the healthy bar at this location is negligible. Moreover, when the broken bar reaches location 3 or 7 it does not produce any axis shift due to the fact that the currents in the remaining (healthy) bars will redistribute to preserve the original, healthy, axis location. Accordingly, the remaining four locations of the bar breakage, namely 2, 4, 6, and 8, will result in a current sheet axis shift which in turn will produce a shift in rotor mmf (or magnetic field) axis. It should be noted that the fact that there are four instances in a slip cycle where the current sheet axis aligns with a healthy current sheet axis leads to the oscillation around the healthy axis at twice the slip frequency. Depicted in Figure 2-4 is the corresponding current sheet under the conditions of one broken rotor bar at a time instant when the broken bar reaches location 4. From Figure 2-4 one should notice that when the breakage reaches location 4 it results in the shift of the so-called magnetic axis of symmetry in the positive half waveform of the current sheet by the angle,  $\Delta\gamma$ , which in turn results in the shift of both the overall current sheet and mmf axes by  $\Delta\delta$ . The maximum shift of the rotor mmf axis,  $\Delta\delta$ , was defined in [43-46] as the swing angle and can be calculated through computation of voltage and current space vectors using standard line current and voltage measurements [43-46]. As was mentioned earlier this shifting of the current sheet and mmf axes takes place four times during one slip cycle and reaches its maximum absolute value at four locations, namely 2, 4, 6, and 8.



## 2.3 ROTOR WITH NONADJACENT BAR BREAKAGES

In this section nonadjacent bar breakages will be considered. More specifically, breakages separated by a half pole-pitch and one pole-pitch are being considered here, where a pole-pitch measure is considered to be equal to the number of rotor bars per pole. It will be shown that these two nonadjacent breakage scenarios represent two special cases that will provide the basis for understanding the effects of other nonadjacent rotor bar breakages on motor performance, and ease or difficulty in diagnosing such bar breakages.

### 2.3.1 HALF POLE-PITCH

Here, the effects of two broken bars, separated by a half pole-pitch ( $90^\circ$  electrical), on the rotor current sheet and rotor mmf will be considered. Using the example of the simple 8-bar cage, the effects of two nonadjacent breakages separated by  $90^\circ$  are shown in Figure 2-5. At the time instant depicted in Figures 2-5 and 2-6 the broken bars are at location 2 and 4. As one can see from Figures 2-5 and 2-6 the current sheet axis in the positive half waveform in the case of two broken bars separated by half a pole-pitch is congruent with the current sheet axis in the positive half waveform of the healthy case. Moreover, the axes of the current sheet and mmf will remain congruent with the axes of the healthy case throughout a slip cycle producing no detectable rotor mmf oscillation as a result of the fault, hence, significantly reducing chances to successfully diagnose such a fault. This fault scenario represents the first special case of nonadjacent rotor faults. Moreover, chances of successful diagnosis, when the separation between the nonadjacent bar breakages approaches half pole-pitch, are significantly reduced. It should be noted that a similar masking effect on the fault indices of motor current signature analysis as well as on one of the model reference diagnostic techniques known as Vienna Method has been observed earlier in [42] and [48], respectively. However, the explanation of the mechanisms behind the masking

effect presented in [48] leaves something to be desired in the sense that it is claimed that the maximum disturbance of the rotor magnetic field occurs when the broken bar is at location, where in the healthy case, this bar is supposed to carry the highest current. Referring back to Figure 2-2 that would mean that the maximum detectable disturbance of the rotor magnetic field will occur at location 3 or 7, however, it is not the case as was shown in the previous section. Moreover, more concrete evidence verifying the analysis presented in this chapter will be presented in the following chapters both from time-stepping finite element and magnetic equivalent circuit models, as well as from experimental results.

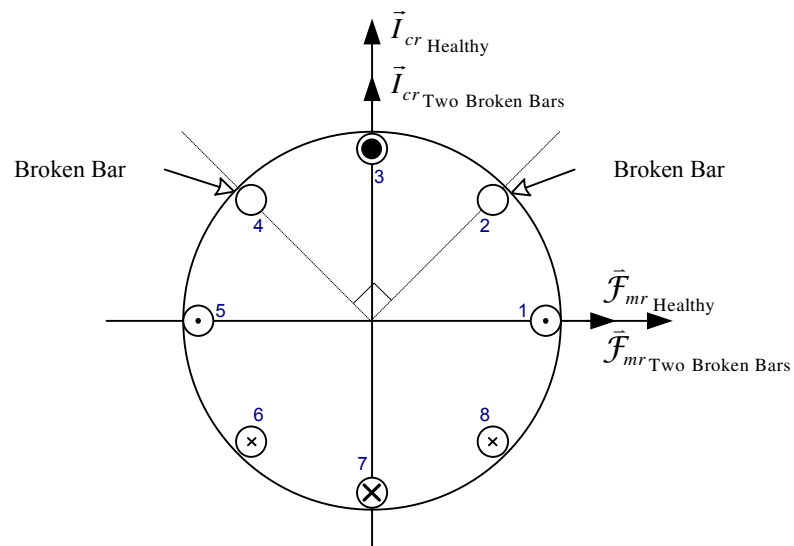


**Figure 2-5.** Simple 8-bar squirrel-cage rotor (Broken bars at locations 2 and 4).

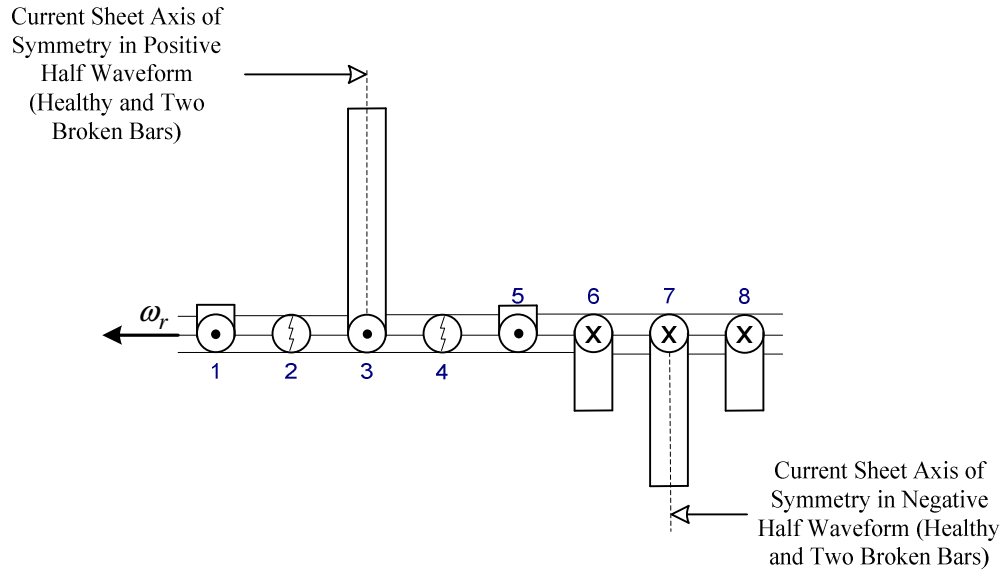


**Figure 2-6.** Rotor current sheet (Broken bars at locations 2 and 4).

### 2.3.2 ONE POLE-PITCH

Here, the effects of two broken bars, separated by one pole-pitch ( $180^\circ$  electrical), on the rotor current sheet and rotor mmf will be considered. As can be seen from Figures 2-7 and 2-8 the current sheet symmetry axes in the positive and negative half waveforms in the case of two broken bars separated by one pole-pitch are shifted by an angle,  $\Delta\gamma$ , from the healthy axes resulting in the overall shift of the rotor mmf. Hence, two breakages separated by one pole-pitch will result in the oscillation of the rotor mmf with a maximum value of the swing angle equal to  $\Delta\delta = \Delta\gamma$ . It can also be shown that this shift is identical to the shift produced by the two adjacent bar breakages, hence, resulting in the same values of fault indices. This fault scenario represents the second special case of nonadjacent rotor faults. In the case when the separation between the nonadjacent bar breakages approaches one pole-pitch, the rotor mmf appears to be disturbed in the same way as in the case of an adjacent fault. Accordingly, from this simple analysis it appears that there will be no masking effect manifested in the case when bar breakages are separated by a complete pole-pitch.

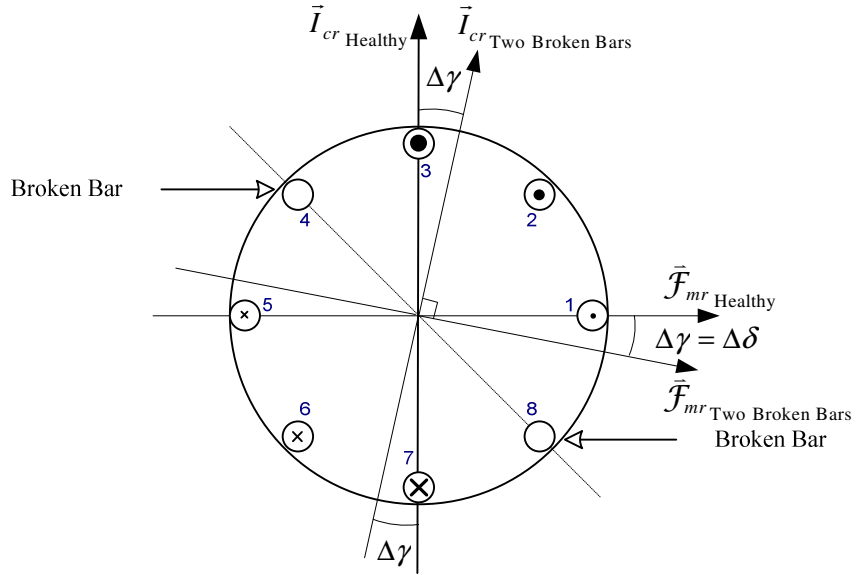


Figure 2-7. Simple 8-bar squirrel-cage rotor (Broken bars at locations 4 and 8).

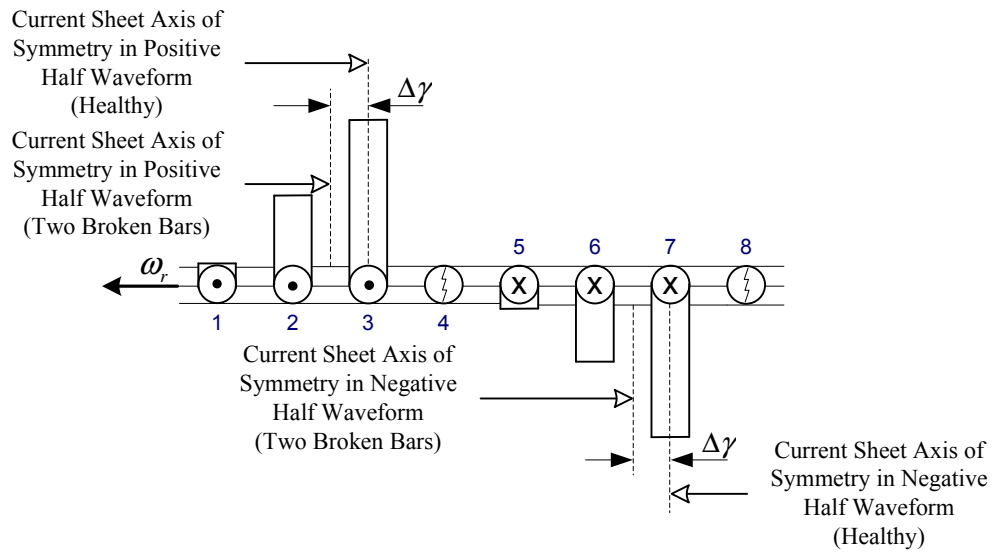


Figure 2-8. Rotor current sheet (Broken bars at locations 4 and 8).

In summary, this chapter presented a simple model that can be used to visualize effects produced by rotor bar breakages on the squirrel-cage rotor spatial current distribution and the corresponding rotor mmf. It should be stressed that this simple qualitative approach to rotor fault visualization resulted from extensive fault simulation using magnetic equivalent circuit models (MEC) and time-stepping finite element (TSFE) analysis, details of which will be given in a later chapter of this thesis. Moreover, from the analysis presented above, it should be observed that a rotor bar breakage results in a slight reduction of the magnitude of rotor mmf, however, more importantly it results in the oscillation of the rotor mmf, which in turn produces the detectable magnetic field disturbance. This field disturbance may manifest itself in a number of ways that can be used to detect such a fault. More specifically, it reflects itself in the stator currents by modulating the amplitudes of line currents. It also produces detectable torque oscillations, which may in turn result in consequent speed oscillations. More on these aspects will be discussed in later chapters.

## CHAPTER 3: INDUCTION MACHINE MODELING

---

### 3.1 INTRODUCTION

**N**UMEROUS induction machine models have been developed over the years [53-74]. These models range from the simplest T-equivalent circuit models, described in [53-55], and [60], to more sophisticated ones such as: multiple coupled circuit models where inductances are calculated using the winding function approach [61-66], magnetic equivalent circuit models, also known as the permeance network models, [67-74], and the finite element models [34], [75], [76]. Application of the specific model to a specific task depends on the level of desired accuracy, computational time, as well as on the complexity of the physical phenomena that need to be studied and included in the solution.

For example, the T-equivalent circuit model can be used to simulate the machine under steady-state conditions. However, when such a model is used to simulate the starting transient or sudden load change scenarios it can only provide one with an average solution. Moreover, the validity of this model becomes highly questionable when the motor is supplied by a power electronic device, such as, an ac inverter.

More sophisticated abc flux-linkage and/or current frame of reference models that may account for effects of the space-harmonics as well as their interaction with an ac inverter induced

time-harmonics have also been developed [53-59]. In these models the information about the space-harmonics has to be obtained prior to the simulation through either analytical or static finite element simulation means [77]. It should also be mentioned that in some of these models it is assumed that the rotor of a squirrel-cage induction machine behaves as an equivalent three-phase winding. One of the more well known simplification to these models that allows one to include the space-harmonics of up to the second order is a well know dq0 induction machine model [53], [54], [57-59]. This model is widely used in the ac drive industry due to its relative simplicity, good accuracy, and more importantly fast execution time. The latter property is of crucial importance to the ac drive designers since it allows one to apply this model in a microcontroller based control algorithm of an ac drive. Moreover, the parameters of this model can be estimated through the standard motor tests, such as, the no-load and locked-rotor tests. Hence, this model is considered a good choice in the task of programming the control of the induction machine's speed and torque production.

Multiple coupled circuit models based on the winding function approach have been developed in [61-63]. These models allow one to incorporate the space-harmonics produced as a result of nonsinusoidally distributed mmfs of stator and rotor windings. In this modeling approach various mutual and self inductances are calculated based on the machine geometry and winding layout. It should be noted that this model is similar to the abc flux-linkage/current frame of reference model in the sense that some inductance terms are time-varying. However, here the assumption of squirrel-cage rotor behaving as an equivalent three-phase winding is no longer necessary. Hence, the order of the model can be significantly increased to account for additional states associated with squirrel-cage rotors leading to increased accuracy of the model. The increase in the number of states accounting for the individual squirrel-cage rotor loops makes this model suitable for squirrel-cage rotor fault modeling [62]. Moreover, this model can be extended

to model stator winding faults as has been shown in [64]. Also, provided in this model is a consistent approach to calculation of the various machine parameters based on the geometry and winding layout through the use of air gap winding functions [61-66]. There are two types of parameters that exist in this model, time-varying mutual inductances between stator and rotor circuits that are constantly updated during the simulation process, and various leakage inductances, which can be calculated prior to the simulation. The winding function approach used to calculate the parameters of this model has been extended to include the effects of rotor skewing [65], as well as partially account for saturation effects [66].

In this thesis two models are used to simulate squirrel-cage rotor faults, namely, a magnetic equivalent circuit model and time-stepping finite element model. The magnetic equivalent circuit (MEC) model allows one to incorporate space-harmonics due to discrete winding distribution, stator and rotor slotting, as well as the saliency effect caused by saturation of the magnetic material [67-74]. Moreover, the deep-bar effect, also known as the skin effect, can be included in the solution to provide a more realistic transient model of the machine [68]. The magnetic equivalent circuit model provides reasonably accurate results and relatively small computation time, when compared to the time-stepping finite element (TSFE) model. Finite element models in general provide a higher degree of space discretization, and hence a more accurate solution, when compared to the MEC approach. However, the computational time required by a finite element model is significantly increased due to its complexity. Nevertheless, time-stepping finite element analysis is a useful tool in fault diagnostics studies, as was shown in [34] and [77]. Implementation of the MEC and TSFE models will be discussed in more detail in the following sections.

### 3.2 MAGNETIC EQUIVALENT CIRCUIT MODEL

In this section development of the magnetic equivalent circuit (MEC) model for fault simulation studies will be discussed. As was previously mentioned, the MEC model allows one to account for effects associated with the discrete winding distribution, rotor/stator slotting and skewing, as well as the saturation effects, resulting from the nonlinear magnetic material properties. Similar to the finite element modeling approach, the space discretization of the machine can be increased in order to provide more accurate results [68]. The MEC modeling approach has been successfully used to model a variety of electric machines under various healthy and faulty conditions [67-74]. More specifically, the MEC modeling approach has been used to model induction machines under a variety of steady-state and transient conditions in [67-70]. A three-dimensional MEC model has been used in the study of inter-bar currents and the resulting axial fluxes in healthy and faulty induction machines in [73]. In [74] the MEC model has been shown to yield accurate results under a variety of operating conditions: no-load, rated-load, unbalanced excitation, and broken end-ring conditions. It should be noted that in this thesis the formulation of the MEC model developed in [67-70] will be used, since in the opinion of this author, it provides a more consistent and logical approach to development of the model.

The concept of magnetic circuits has been extensively used in engineering practice due to its resemblance to dc electric circuits' analysis. More specifically, magnetic circuits could be analyzed using the same basic principles defined by Kirchhoff's Laws. The use of magnetic circuits, as well as the application of Kirchhoff's Laws in electric circuits, is possible because of several assumptions. Namely, for magnetic circuits it is assumed that a change in the coil current produces an immediate corresponding change in magnetic flux. Furthermore, magnetic flux propagates instantly throughout the magnetic circuit, meaning that no wave propagation phenomenon exists. This is similar to the assumption used for electric circuits that all changes in

the circuit take place simultaneously, when Kirchhoff's Laws are to be utilized for circuit analysis. In other words, these assumptions state that the time needed for the electromagnetic wave to propagate through the magnetic device or electrical circuit is negligible in comparison to the period of the wave. This is similar to stating that the dimensions of the magnetic device or an electric circuit to be studied have to be much less than the wavelength of the electromagnetic wave for the Kirchhoff's Laws to be valid. In terms of Maxwell's Equations this means that the equations can be simplified as will be shown next. Starting with the original set of Maxwell's Equations:

$$\nabla \times \vec{H} = \vec{J} + \frac{\partial \vec{D}}{\partial t} \quad (\text{Ampere's Law with Maxwell's modification}) \quad (3.1)$$

$$\nabla \cdot \vec{B} = 0 \quad (\text{Gauss' Law for Magnetism}) \quad (3.2)$$

$$\nabla \times \vec{E} = -\frac{\partial \vec{B}}{\partial t} \quad (\text{Faraday's Law}) \quad (3.3)$$

$$\nabla \cdot \vec{D} = \rho \quad (\text{Gauss' Law}) \quad (3.4)$$

The auxiliary equations relating the magnetic flux density,  $\vec{B}$ , and magnetic field intensity,  $\vec{H}$ , and relating the electric,  $\vec{E}$ , to the displacement field,  $\vec{D}$ , and current density,  $\vec{J}$ , are provided in equations (3.5) through (3.7) below.

$$\vec{B} = \mu \vec{H} \quad (3.5)$$

$$\vec{D} = \epsilon \vec{E} \quad (3.6)$$

$$\vec{J} = \sigma \vec{E} \quad (3.7)$$

Considering the right hand side of (3.1), in most low-frequency applications where the capacitive coupling is insignificant it is safe to assume that the displacement current density,  $\frac{\partial \vec{D}}{\partial t}$ , can be neglected. This assumption is valid in most situations where conduction current is

dominant and the operational frequencies are low [55], which is the case here in this work.

Hence, the set of Maxwell's Equations can be reduced to the following:

$$\nabla \times \vec{H} = \vec{J} \quad (\text{Ampere's Law original definition}) \quad (3.8)$$

$$\nabla \cdot \vec{B} = 0 \quad (\text{Gauss' Law for Magnetism}) \quad (3.9)$$

$$\nabla \times \vec{E} = -\frac{\partial \vec{B}}{\partial t} \quad (\text{Faraday's Law}) \quad (3.10)$$

In magnetic equivalent circuits only two of the remaining Maxwell's Equations are utilized, namely, Ampere's Law in its original definition (3.8), and Gauss' Law (3.9). The third equation, Faraday's Law, (3.10) is used to account for the effects that the changing flux might have on the coil current. In other words, along with equation (3.8), equation (3.10) provides the means of connecting the magnetic equivalent circuit to the outside world, e.g., electric circuitry that may be connected to the terminals of the device. Now using a simple example provided in [55] consider a magnetic device such as the one shown in Figure 3-1.

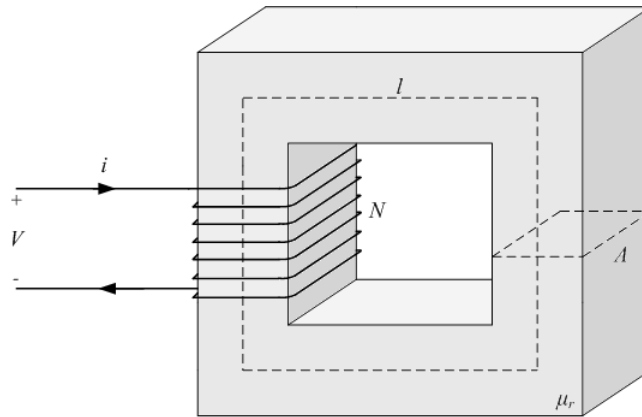


**Figure 3-1.** Simple magnetic device.

Here, considering Ampere's Law in its integral form provided in (3.11) one can define the magnetomotive force (mmf),  $\mathcal{F}$ , sometimes referred to as magnetic scalar potential.

$$\oint_C \vec{H} dl = NI = \mathcal{F} \quad (3.11)$$

For a closed path,  $l$ , one can simplify (3.11) as follows:

$$\mathcal{F} = Hl \quad (3.12)$$

This equation can be rewritten in terms of the flux density,  $B$ , as follows:

$$\mathcal{F} = \frac{B}{\mu_r \mu_o} l \quad (3.13)$$

where,  $\mu_r$ , is relative permeability and,  $\mu_o$ , is permeability of free space. Meanwhile, (3.13) can be expressed in terms of magnetic flux,  $\Phi$ , as follows:

$$\mathcal{F} = \Phi \left( \frac{l}{\mu_r \mu_o A} \right) \quad (3.14)$$

where,  $A$ , is the cross-sectional area of the core perpendicular to the flux density direction. Now, it is possible to define a reluctance,  $\mathfrak{R}$ , and a permeance,  $P$ , as given in (3.15) and (3.16), respectively.

$$\mathfrak{R} = \frac{\mathcal{F}}{\Phi} = \frac{l}{\mu_r \mu_o A} \quad (3.15)$$

$$P = \frac{1}{\mathfrak{R}} = \frac{\mu_r \mu_o A}{l} \quad (3.16)$$

It should be noted that it assumed that the flux in the core of the device, depicted in Figure 3-1, is uniformly distributed across the cross-section of the core. Moreover, it is also assumed that all magnetic flux produce by the coil is confined to the core. However, it should also be mentioned that these assumptions can be eliminated if the space discretization of the device is increased. In other words, increasing the number of reluctance/permeance elements characterizing the magnetic device can increase the accuracy of the solution. Also, from the above discussion one should note the similarity between the magnetic and resistive electric circuits, which can also be seen from the schematic in Figure 3-2.

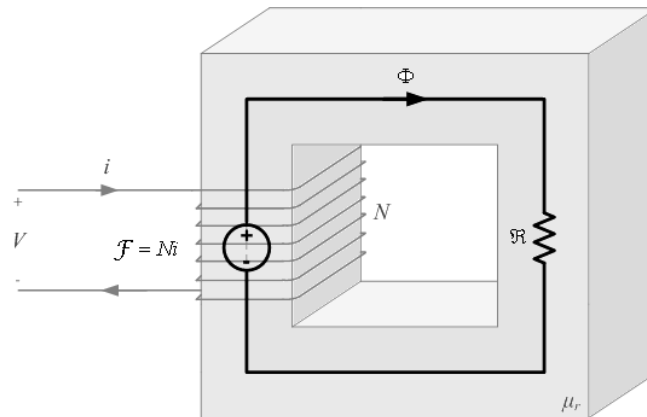


**Figure 3-2.** Magnetic equivalent circuit representation of a simple magnetic device.

Moreover, the above discussion can be extended to show the corresponding similarities between Ampere's Law and Kirchhoff's Voltage Law, and Gauss' Law and Kirchhoff's Current Law, when applied to the magnetic equivalent circuits. Hence, the reader should be convinced that the magnetic properties of the problem depicted in Figures 3-1 and 3-2 can be characterized by a set of algebraic equations. However, in the case of a time-varying coil current Faraday's Law, (3.10), has to be invoked to account for the interaction between the electric and magnetic circuits.

A cross-section of a 5-hp squirrel-cage induction machine that will be studied in this thesis is depicted in Figure 3-3. This machine has six poles, 36 stator and 45 rotor slots. It has a double-layer stator winding with the layout shown in Figure 3-4. In Figure 3-4 "Top" refers to the part of the stator slot closest to the air gap, whereas "Bottom" refers to the part of the slot closest to the back iron. Moreover, this machine has two coils per pole per phase, a total of 36 coils, with 20 turns per coil. Also, provided in Figures 3-5 and 3-6 are the close-up views of the stator and rotor slots. Here, it should be noted that not all of the dimensions required to completely characterize the geometry of the slots are included in the drawings. The reason for this stems from the fact that the shapes of the slots will be simplified for the purpose of calculation of reluctances/permeances as will be given in further analysis.

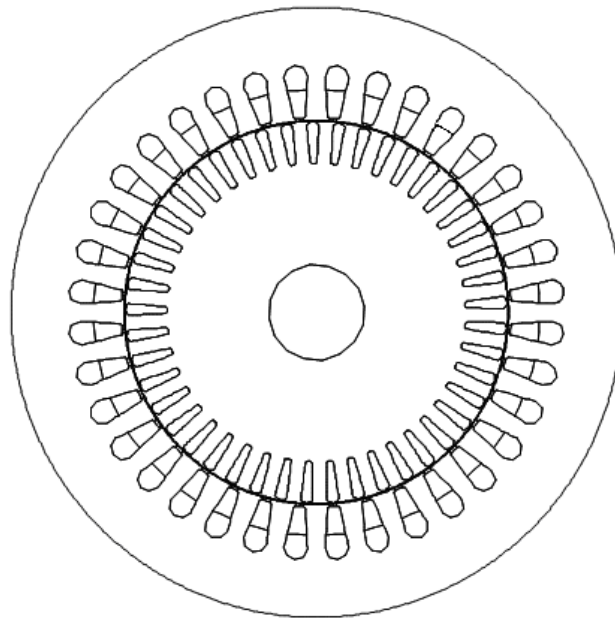


Figure 3-3. Cross-section of the 5-hp squirrel-cage induction machine.

<i>Top</i>	A+	C-	C-	B+	B+	A-	A-	C+	C+	B-	B-	A+	A+	C-	C-	B+	B+	A-
<i>Bottom</i>	A+	A+	C-	C-	B+	B+	A-	A-	C+	C+	B-	B-	A+	A+	C-	C-	B+	B+
<i>Slot</i>	1	2	3	4	5	6	7	8	9	10	11	12	13	14	15	16	17	18
	A-	C+	C+	B-	B-	A+	A+	C-	C-	B+	B+	A-	A-	C+	C+	B-	B-	A+
	A-	A-	C+	C+	B-	B-	A+	A+	C-	C-	B+	B+	A-	A-	C+	C+	B-	B-
	19	20	21	22	23	24	25	26	27	28	29	30	31	32	33	34	35	36

Figure 3-4. Stator winding layout of the 5-hp squirrel-cage induction machine.

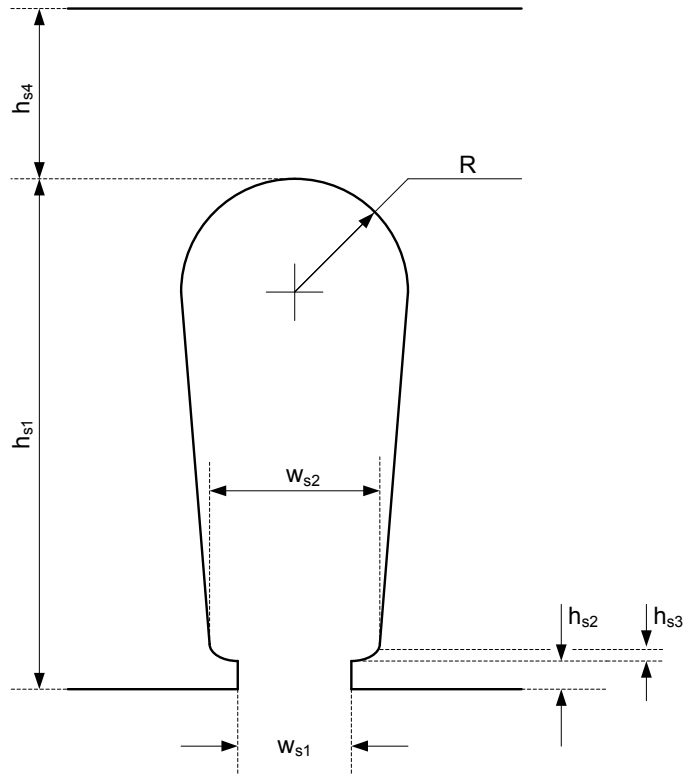


Figure 3-5. Stator slot of the 5-hp induction machine.

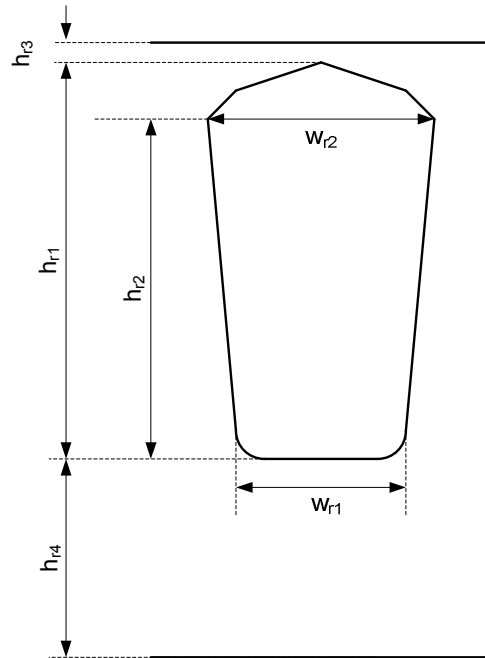


Figure 3-6. Rotor slot of the 5-hp induction machine.

A stator slot with a double-layer winding, depicted in Figures 3-4 and 3-5, can be represented by a magnetic equivalent circuit shown in Figure 3-7. In this magnetic equivalent circuit representation,  $\mathfrak{R}_{S_{TAN\ i}}$ , is the tangential leakage reluctance of the inner stator layer and,  $\mathfrak{R}_{S_{TAN\ o}}$ , is the tangential leakage reluctance of the outer layer. Meanwhile, the teeth of the stator are divided into two reluctances,  $\mathfrak{R}_{S_{TOOTH\ i}}$ , for the upper part of the tooth and,  $\mathfrak{R}_{S_{TOOTH\ o}}$ , for the lower part of the tooth. Moreover, the effect of the current carried by every coil side in the slot can be accounted for by the mmf sources, shown in Figure 3-7. Here,  $\mathcal{F}_{S_i}$ , is the mmf produced by the coil side in the inner layer whereas,  $\mathcal{F}_{S_o}$ , is the mmf produced by the coil side in the outer layer. Meanwhile, the backiron can be characterized by a single reluctance value,  $\mathfrak{R}_{S_{YOKE}}$ . It should be noted that index,  $m$ , is used here to distinguish between the individual stator tooth reluctances, which may vary from tooth to tooth if saturation needs to be considered. As was shown in [68], the magnetic equivalent circuit described above can be simplified as depicted in Figure 3-8. In the magnetic circuit of Figure 3-8 every stator tooth is represented by a single tooth reluctance,  $\mathfrak{R}_{S_{TOOTH}}$ , and a single mmf source,  $\mathcal{F}_S$ . Moreover, the stator slot tangential leakage reluctance is lumped into a single reluctance term,  $\mathfrak{R}_{S_{TAN}}$ . It should be mentioned that the stator slot tangential leakage reluctance,  $\mathfrak{R}_{S_{TAN}}$ , is a function of the slot geometry only and hence will remain constant during the operation of the machine. In this magnetic circuit representation of the stator slot it is assumed that the magnetic flux can flow in either of the two directions, namely, radial and/or tangential, as shown in Figures 3-7 and 3-8. Meanwhile, mmf sources are placed in the stator teeth in order to represent the effect of the current carrying coil sides. Also, the reluctance values representing the regions of the stator where the magnetic material is present, namely,  $\mathfrak{R}_{S_{TOOTH\ i}}$ ,  $\mathfrak{R}_{S_{TOOTH\ o}}$ , and,  $\mathfrak{R}_{S_{YOKE}}$ , of Figure 3-7, and  $\mathfrak{R}_{S_{TOOTH}}$ ,  $\mathfrak{R}_{S_{YOKE}}$ , of Figure 3-8 can be varied depending on the value of the flux density. Therefore, varying these reluctances, depending on the value of the flux density enables one to capture the effects of local saturation of the magnetic material in the stator teeth in the solution. These reluctances have been defined in [68] as inherently nonlinear.

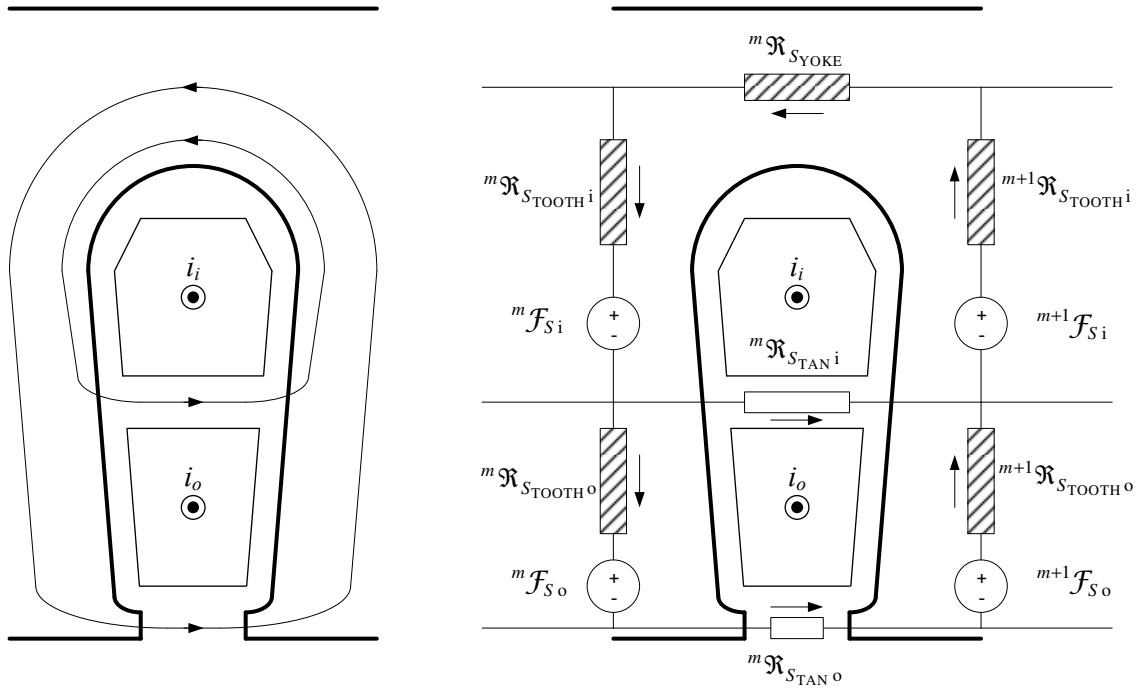


Figure 3-7. MEC representation of a double-layer stator winding.

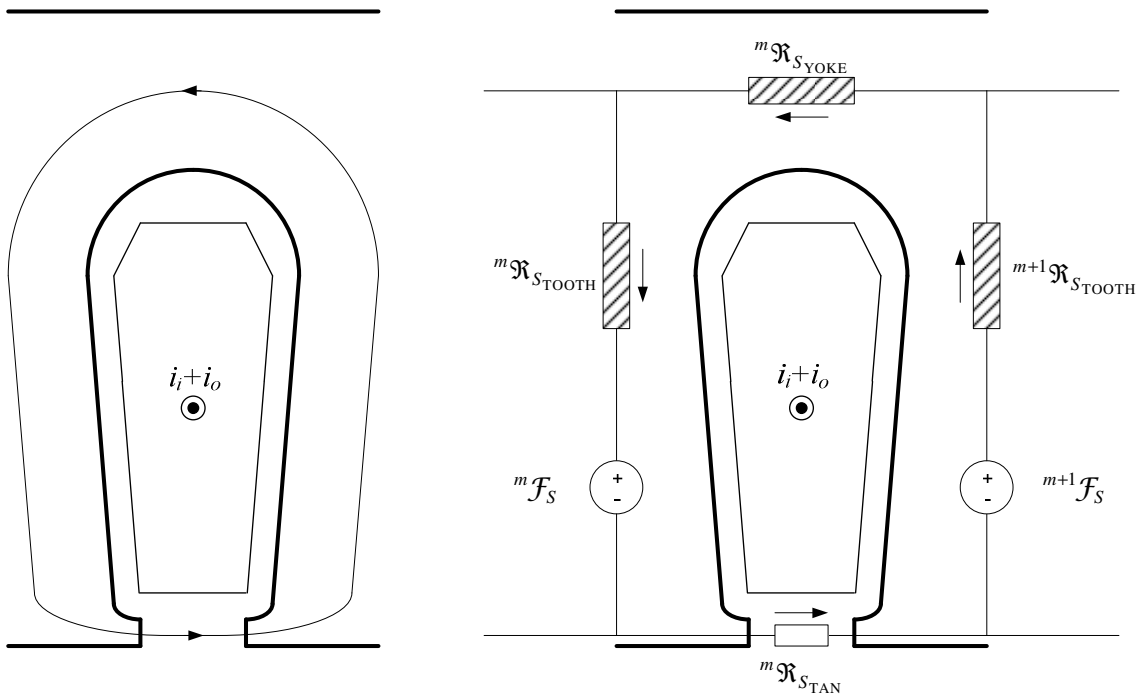


Figure 3-8. Simplified MEC representation of a double-layer stator winding.

The rotor slot design depicted in Figure 3-6 is typical of squirrel-cage induction machines that provide good rated load performance (high power factor, high efficiency, low slip, etc.) while providing an acceptable starting performance (high starting torque, low starting current, etc.). This is possible due to the deep-bar rotor slot design, which provides an increase of rotor impedance at starting, hence, increasing the starting torque and reducing the starting current, while also providing low rotor impedance at rated conditions resulting in relatively good performance at rated load conditions. This is possible because of the so-called deep-bar effect, also known as the skin effect. This deep-bar effect results in the increase of the rotor impedance at starting when the frequency of rotor currents is high. Meanwhile, the rotor impedance decreases, as the rotor speed approaches the synchronous speed, because of the corresponding decrease of the frequency of rotor currents. This variation of the rotor impedance has to be accounted for in the model in order to provide an accurate solution of the transient operation of the machine. More specifically, the deep-bar effect has to be included in the solution when accurate studies of the starting transients need to be performed. However, this deep-bar effect can be neglected if the machine is simulated under steady-state operation. Moreover, the deep-bar effect can also be neglected if the machine is supplied by a close-loop ac drive because of the fact that the speed of the rotor is always varied (due to the drive's controller action) such that the difference between the rotor speed and the synchronous speed (commanded by the drive) is low, hence, resulting in the low frequency rotor currents. It has been shown in [68] that the deep-bar effect can be modeled using magnetic equivalent circuit technique by dividing the rotor slot into a number of layers, as depicted in Figure 3-9. From Figure 3-9 it should be observed that the lower,  $i^{\text{th}}$ , layer is linked by the highest magnetic flux, hence, the  $i^{\text{th}}$  layer has the highest value of leakage inductance. At low rotor speeds (high rotor current frequency) this results in the high values of  $i^{\text{th}}$  layer leakage reactance increasing the overall impedance of this layer. Moreover, this means that at low rotor speeds the current tends to crowd in the top layers of the slot. One should also

observe that in Figure 3-9 there are two types of reluctances, namely, inherently nonlinear reluctances, which depend on the value of the magnetic flux density, and constant reluctances, which are independent of the flux density [68]. Again, in Figure 3-9, the index,  $n$ , is used to distinguish between the individual rotor teeth.

In this thesis, however, a simplified rotor slot magnetic equivalent representation will be used. This model is depicted in Figure 3-10. As can be observed from Figure 3-10, this model of the rotor slot does not allow one to directly incorporate the deep-bar effect in the magnetic solution of the machine. In this thesis, this author opted for the use of an analytical approach where rotor impedance will be calculated based on the rotor speed and some basic rotor slot dimensions. This allows one to significantly reduce the order of the magnetic equivalent circuit model while still providing acceptable accuracy in simulations of the transient machine operation. It has been shown in [57] that for very narrow rectangular rotor slot the impedance as a function of frequency can be approximated as follows:

$$X_{slot} = R_{dc} \alpha d \left\{ \left( \frac{\sinh(2\alpha d) + \sin(2\alpha d)}{\cosh(2\alpha d) - \cos(2\alpha d)} \right) + j \left( \frac{\sinh(2\alpha d) - \sin(2\alpha d)}{\cosh(2\alpha d) - \cos(2\alpha d)} \right) \right\} \quad (3.17)$$

$$\text{where, } \alpha = 2\pi \sqrt{\frac{rf}{\rho 10^9}},$$

$R_{dc}$  = dc rotor slot resistance, [ $\Omega$ ],

$d$  = depth of the slot [cm],

$r$  = ratio of bar width to slot width,

$f$  = slip frequency, [Hz],

$\rho$  = resistivity of the conducting material [ $\Omega$ -cm].

Again, it should be stressed here that it is assumed that the rotor slot can be approximate as a narrow rectangular slot surrounded by a core of infinite permeability. Meanwhile, in the MEC representation of the machine, more realistic slot geometry and value of core permeability are used for reluctance calculations.

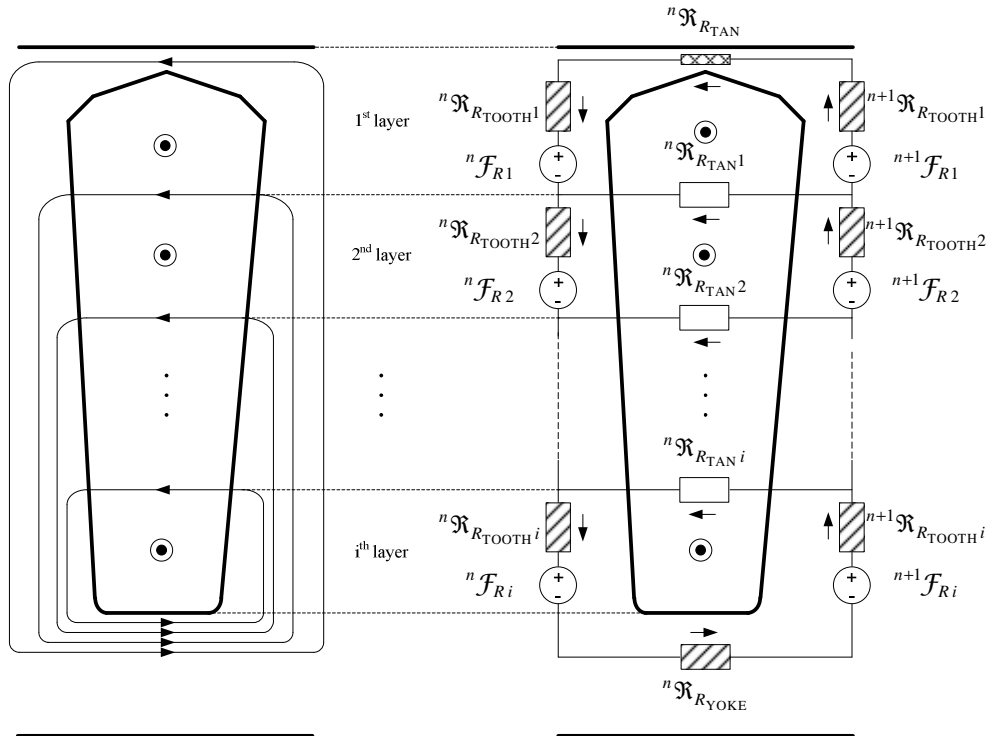


Figure 3-9. MEC representation of a rotor slot (with deep-bar effect).

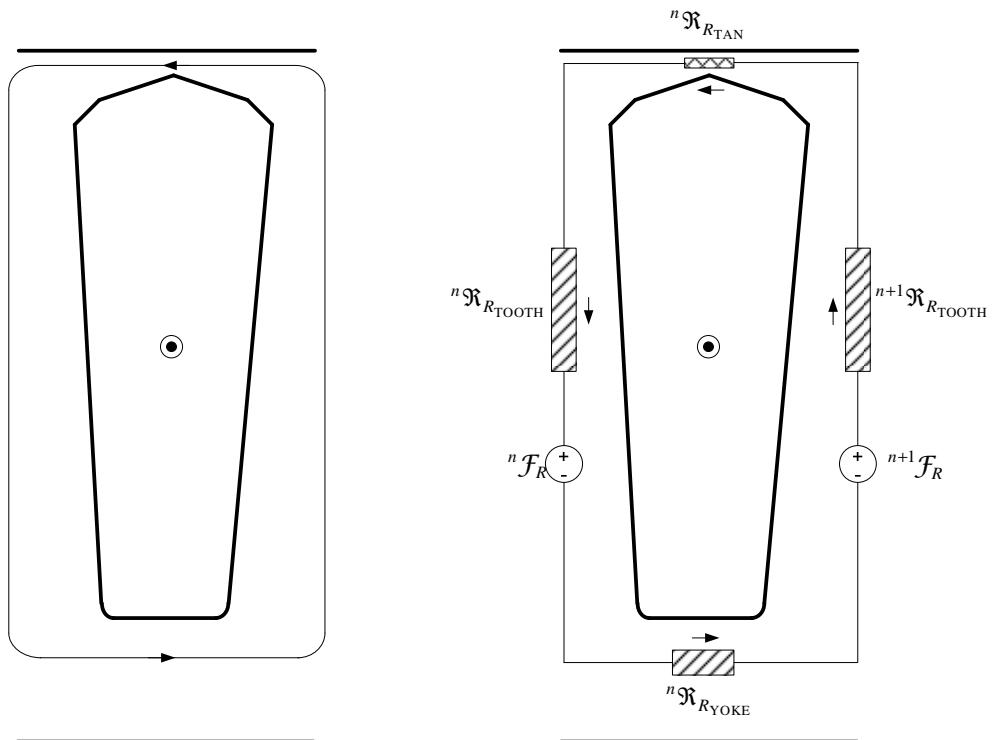


Figure 3-10. Simplified MEC representation of a rotor slot (without deep-bar effect).

Now that both the stator and rotor slot magnetic equivalent circuits are defined a complete magnetic equivalent circuit model of the induction machine can be assembled. This model is depicted in Figure 3-11. In this figure, air gap reluctances are included to provide the coupling between the rotor and the stator teeth. It should be noted that electromechanical energy conversion takes place in the air gap; hence, it is crucial to model the air gap reluctances as accurately as possible. Moreover, from Figure 3-11 it should be noted that the MEC model is assembled such that every tooth on the stator is coupled to every tooth on the rotor, and vice versa. It should also be noted that the air gap reluctance represents the third and the last class of the reluctances used in the induction machine's MEC modeling [68]. These reluctances are referred to as parametric nonlinear reluctances in [68]. This is because these reluctances depend on relative position between the corresponding stator and rotor teeth. Hence, unlike in the case of inherently nonlinear reluctances, where the value of reluctance is a function of magnetic flux density, here in the case of nonlinear parametric reluctances the value of reluctance is a function of geometry (relative position of the rotor with respect to the stator). More specifically, air gap reluctance is a function of the area of overlap of stator and rotor teeth. The air gap reluctance modeling is discussed in detail in the Appendix of this thesis. It should also be mentioned that from this point on all reluctances will be replaced with corresponding permeances. The reason for this stems from the fact that in the further analysis the node-potential method will be used to solve the magnetic equivalent circuit model. Therefore, to avoid possible numerical difficulties in a computer simulation associated with possibilities of dealing with infinite air gap reluctances one should inverse the reluctance values to obtain the corresponding permeance values. It should be noted that radial leakage flux can also be accounted for in the MEC representation of the stator and rotor slots. However, it has been shown in [70] that the effect of the radial leakage flux on the performance of the machine is insignificant and can be ignored. This also results in the significant simplification of the node-potential analysis that will be shown next.

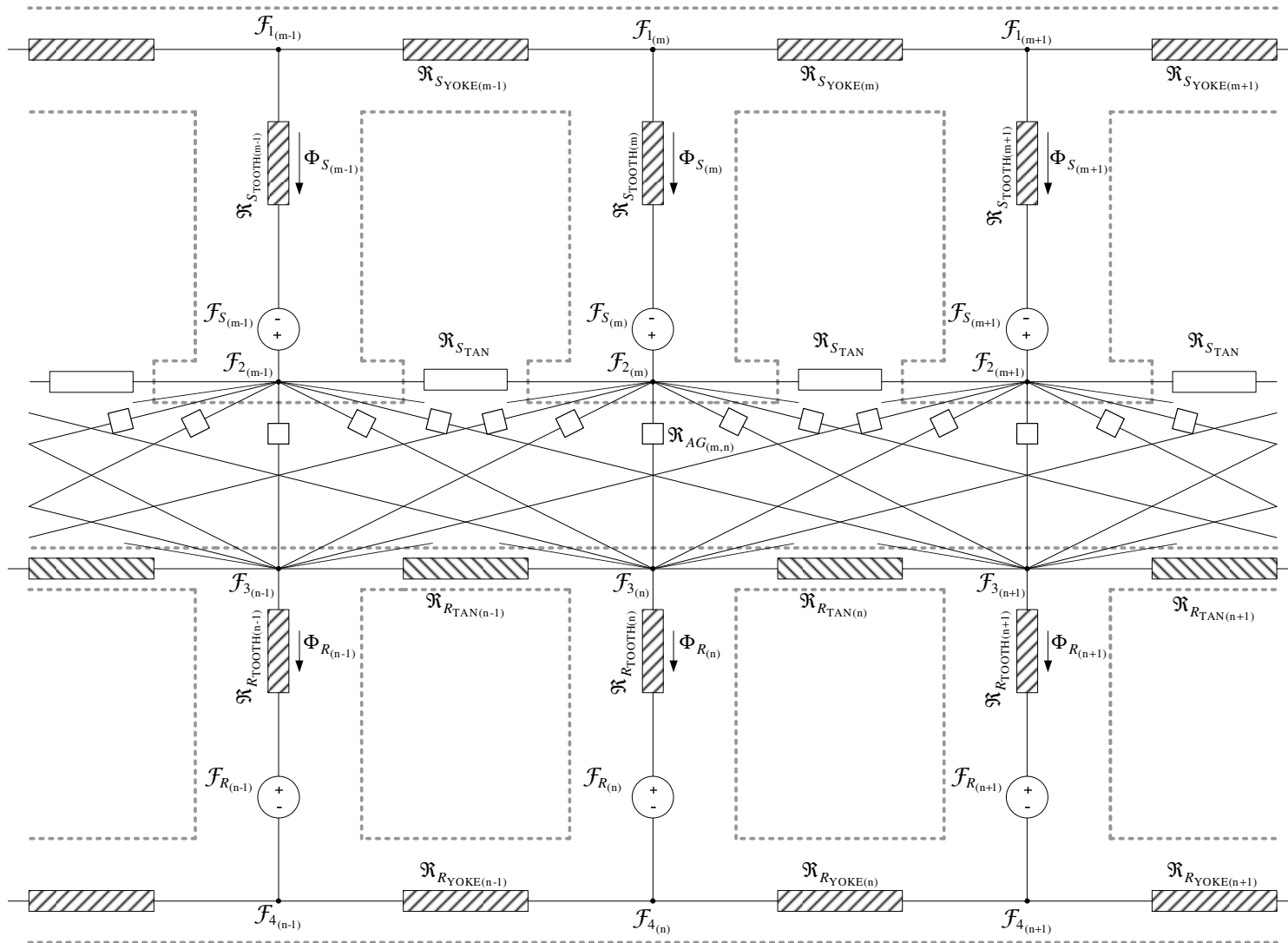


Figure 3-11. MEC representation of the 5-hp induction machine (with closed rotor slot).

From Figure 3-11 one can proceed with the development of the system of algebraic equations. As was mentioned earlier, the node-potential method will be used to generate the required equations. The nodes used to generate the equations are:  $\mathcal{F}_{1(m)}$ ,  $\mathcal{F}_{2(m)}$ ,  $\mathcal{F}_{3(n)}$ ,  $\mathcal{F}_{4(n)}$ , where the index,  $m$ , identifies a stator tooth and the index,  $n$ , is used to identify a specific rotor tooth. Hence, in the case-study motor with 36 stator slots and 45 rotor slots, the index,  $m$ , varies from 1 to 36, and the index,  $n$ , varies from 1 to 45. Considering Figure 3-11 with the reluctances substituted with the corresponding permeances, one can develop four sets of nodal equations.

Considering node,  $\mathcal{F}_{1(m)}$ , one can write the following:

$$P_{S_{\text{YOKE}(m-1)}} (\mathcal{F}_{1(m)} - \mathcal{F}_{1(m-1)}) + P_{S_{\text{YOKE}(m)}} (\mathcal{F}_{1(m)} - \mathcal{F}_{1(m+1)}) + \Phi_{S(m)} = 0 \quad (3.18)$$

Meanwhile, considering node,  $\mathcal{F}_{2(m)}$ , one can write the following:

$$P_{S_{\text{TAN}}(m-1)} (\mathcal{F}_{2(m)} - \mathcal{F}_{2(m-1)}) + P_{S_{\text{TAN}}(m)} (\mathcal{F}_{2(m)} - \mathcal{F}_{2(m+1)}) + \sum_{n=1}^{n=N_R} P_{AG(m,n)} (\mathcal{F}_{2(m)} - \mathcal{F}_{3(n)}) - \Phi_{S(m)} = 0 \quad (3.19)$$

Considering node,  $\mathcal{F}_{3(n)}$ , one can write the following:

$$P_{R_{\text{TAN}}(n-1)} (\mathcal{F}_{3(n)} - \mathcal{F}_{3(n-1)}) + P_{R_{\text{TAN}}(n)} (\mathcal{F}_{3(n)} - \mathcal{F}_{3(n+1)}) + \sum_{m=1}^{m=N_S} P_{AG(m,n)} (\mathcal{F}_{3(n)} - \mathcal{F}_{2(m)}) + \Phi_{R(n)} = 0 \quad (3.20)$$

Finally, considering node,  $\mathcal{F}_{4(n)}$ , one can write the following:

$$P_{R_{\text{YOKE}(n-1)}} (\mathcal{F}_{4(n)} - \mathcal{F}_{4(n-1)}) + P_{R_{\text{YOKE}(n)}} (\mathcal{F}_{4(n)} - \mathcal{F}_{4(n+1)}) - \Phi_{R(n)} = 0 \quad (3.21)$$

Equations (3.18) through (3.21) can be rewritten as follows:

$$(-P_{S_{\text{YOKE}(m-1)}}) \mathcal{F}_{1(m-1)} + (P_{S_{\text{YOKE}(m-1)}} + P_{S_{\text{YOKE}(m)}}) \mathcal{F}_{1(m)} + (-P_{S_{\text{YOKE}(m)}}) \mathcal{F}_{1(m+1)} = -\Phi_{S(m)} \quad (3.22)$$

$$\begin{aligned} & (-P_{S_{\text{TAN}}(m-1)}) \mathcal{F}_{2(m-1)} + \left( 2P_{S_{\text{TAN}}(m)} + \sum_{n=1}^{n=N_R} P_{AG(m,n)} \right) \mathcal{F}_{2(m)} + (-P_{S_{\text{TAN}}(m+1)}) \mathcal{F}_{2(m+1)} + \\ & + (-P_{AG(m,n)}) \mathcal{F}_{3(n)} + \dots + (-P_{AG(m,N_R)}) \mathcal{F}_{3(N_R)} = \Phi_{S(m)} \end{aligned} \quad (3.23)$$

$$\begin{aligned}
& (-P_{R_{\text{TAN}(n-1)}}) \mathcal{F}_{3(n-1)} + \left( P_{R_{\text{TAN}(n-1)}} + P_{R_{\text{TAN}(n)}} + \sum_{m=1}^{m=N_S} P_{AG(m,n)} \right) \mathcal{F}_{2(m)} + (-P_{R_{\text{TAN}(n)}}) \mathcal{F}_{3(n+1)} \\
& + (-P_{AG(m,n)}) \mathcal{F}_{2(m)} + \dots (-P_{AG(N_S,n)}) \mathcal{F}_{2(N_S)} = -\Phi_{R(n)}
\end{aligned} \tag{3.24}$$

$$(-P_{R_{\text{YOKE}(n-1)}}) \mathcal{F}_{4(n-1)} + (P_{R_{\text{YOKE}(n-1)}} + P_{R_{\text{YOKE}(n)}}) \mathcal{F}_{4(n)} + (-P_{R_{\text{YOKE}(n)}}) \mathcal{F}_{4(n+1)} = \Phi_{R(n)} \tag{3.25}$$

Here,  $N_S$ , refers to the number of stator slots (36 slots for the case at hand), whereas,  $N_R$ , refers to the number of rotor slots (45 slots for the case at hand). One could proceed to form the rest of the node-potential equations for every node in the MEC model. Based on these equations one could write the permeance matrices representing the interconnection between the various nodes. Consequently, considering Figure 3-11 along with the equations (3.22) through (3.25), the matrices give in (3.26) through (3.31) can be formed by inspection.

From equation (3.22) along with other equations describing the nodal potentials in the stator's backiron/yoke one can form a matrix of permeances interconnecting the nodes in stator backiron/yoke,  $\underline{\mathbf{A}}_{11}$ , provided in (3.26). The matrix of permeances connecting the nodes in the stator tooth tips,  $\underline{\mathbf{A}}_{22}$ , can be formed from equation (3.23) and is given in (3.27). Also, from equation (3.23) it is possible to form a matrix of the air gap permeances,  $\underline{\mathbf{A}}_{23}$ , interconnecting nodes in the stator and rotor tooth tips, provided in (3.28). It should be noticed that the matrix,  $\underline{\mathbf{A}}_{23}$ , has dimensions of  $N_S \times N_R$ . From equation (3.24), along with the equations describing other rotor tooth tip nodal mmf potentials, one can assemble a matrix of permeances interconnecting nodes in the rotor tooth tips,  $\underline{\mathbf{A}}_{33}$ , given in (3.30). Also, from equation (3.24), along with other equations for the nodes in the rotor tooth tips, it is possible to form a matrix interconnecting the rotor teeth and stator teeth,  $\underline{\mathbf{A}}_{32}$ , given in (3.29). This matrix can also be obtained by transposing the matrix,  $\underline{\mathbf{A}}_{23}$ . Meanwhile, from equation (3.25) one can also write a permeance matrix interconnecting the nodes in the backiron/yoke of the rotor,  $\underline{\mathbf{A}}_{44}$ , see equation (3.31).

$$\underline{\mathbf{A}}_{11} = \begin{bmatrix} P_{S_{\text{YOKE}(N_S)}} + P_{S_{\text{YOKE}(1)}} & -P_{S_{\text{YOKE}(1)}} & 0 & \cdots & 0 & -P_{S_{\text{YOKE}(N_S)}} \\ -P_{S_{\text{YOKE}(1)}} & P_{S_{\text{YOKE}(1)}} + P_{S_{\text{YOKE}(2)}} & -P_{S_{\text{YOKE}(2)}} & \cdots & 0 & 0 \\ & & & \vdots & & \\ -P_{S_{\text{YOKE}(N_S)}} & 0 & 0 & \cdots & -P_{S_{\text{YOKE}(N_S-1)}} & P_{S_{\text{YOKE}(N_S-1)}} + P_{S_{\text{YOKE}(N_S)}} \end{bmatrix}_{N_S \times N_S} \quad (3.26)$$

$$\underline{\mathbf{A}}_{22} = \begin{bmatrix} \left( 2P_{S_{\text{TAN}}} + \sum_{n=1}^{n=N_R} P_{AG(1,n)} \right) & -P_{S_{\text{TAN}}} & 0 & \cdots & 0 & -P_{S_{\text{TAN}}} \\ -P_{S_{\text{TAN}}} & \left( 2P_{S_{\text{TAN}}} + \sum_{n=1}^{n=N_R} P_{AG(2,n)} \right) & -P_{S_{\text{TAN}}} & \cdots & 0 & 0 \\ & & & \vdots & & \\ -P_{S_{\text{TAN}}} & 0 & 0 & \cdots & -P_{S_{\text{TAN}}} & \left( 2P_{S_{\text{TAN}}} + \sum_{n=1}^{n=N_R} P_{AG(N_S,n)} \right) \end{bmatrix}_{N_S \times N_S} \quad (3.27)$$

$$\underline{\mathbf{A}}_{23} = \begin{bmatrix} -P_{AG(1,1)} & -P_{AG(1,2)} & -P_{AG(1,3)} & \cdots & -P_{AG(1,N_R-1)} & -P_{AG(1,N_R)} \\ -P_{AG(2,1)} & -P_{AG(2,2)} & -P_{AG(2,3)} & \cdots & -P_{AG(2,N_R-1)} & -P_{AG(2,N_R)} \\ & & & \vdots & & \\ -P_{AG(N_S,1)} & -P_{AG(N_S,2)} & -P_{AG(N_S,3)} & \cdots & -P_{AG(N_S,N_R-1)} & -P_{AG(N_S,N_R)} \end{bmatrix}_{N_S \times N_R} \quad (3.28)$$

$$\underline{\mathbf{A}}_{32} = \underline{\mathbf{A}}_{23}^T \quad (3.29)$$

$$\underline{\mathbf{A}}_{33} = \begin{bmatrix} \left( P_{R_{\text{TAN}(N_R)}} + P_{R_{\text{TAN}(1)}} + \sum_{m=1}^{m=N_S} P_{AG(m,1)} \right) & -P_{R_{\text{TAN}(1)}} & 0 & \cdots & 0 & -P_{R_{\text{TAN}(N_R)}} \\ -P_{R_{\text{TAN}(1)}} & \left( P_{R_{\text{TAN}(1)}} + P_{R_{\text{TAN}(2)}} + \sum_{m=1}^{m=N_S} P_{AG(m,2)} \right) - P_{R_{\text{TAN}(2)}} & \cdots & 0 & & 0 \\ & & \vdots & & & \\ -P_{R_{\text{TAN}(N_R)}} & 0 & 0 & \cdots & -P_{R_{\text{TAN}(N_{R-1})}} & \left( P_{R_{\text{TAN}(N_{R-1})}} + P_{R_{\text{TAN}(N_R)}} + \sum_{m=1}^{m=N_S} P_{AG(m,N_R)} \right) \end{bmatrix}_{N_R \times N_R} \quad (3.30)$$

$$\underline{\mathbf{A}}_{44} = \begin{bmatrix} P_{R_{\text{YOKE}(N_R)}} + P_{R_{\text{YOKE}(1)}} & -P_{R_{\text{YOKE}(1)}} & 0 & \cdots & 0 & 0 \\ -P_{R_{\text{YOKE}(1)}} & P_{R_{\text{YOKE}(1)}} + P_{R_{\text{YOKE}(2)}} & -P_{R_{\text{YOKE}(2)}} & \cdots & 0 & 0 \\ & & \vdots & & & \\ 0 & 0 & 0 & \cdots & -P_{R_{\text{YOKE}(N_{R-2})}} & P_{R_{\text{YOKE}(N_{R-2})}} + P_{R_{\text{YOKE}(N_{R-1})}} \end{bmatrix}_{N_{R-1} \times N_{R-1}} \quad (3.31)$$

These matrices along with the vectors of nodal potentials (mmfs) and stator and rotor teeth fluxes, provided in (3.32) through (3.37), form a complete magnetic circuit model, given in (3.38). It should be noticed that the potential at node,  $\mathcal{F}_{4(N_R-1)}$ , is set to zero for reference purposes [68]. Also, from (3.38) one can see that the first and the last rows are not coupled to the second and the third rows. This is possible because of elimination of the radial stator and rotor slot leakage and will result in the consequent simplification of the overall problem, as has been shown earlier in [70].

$$\underline{\mathcal{F}}_1 = [\mathcal{F}_{1(1)} \quad \mathcal{F}_{1(2)} \quad \mathcal{F}_{1(3)} \quad \cdots \quad \mathcal{F}_{1(N_S)}]^T \quad (3.32)$$

$$\underline{\mathcal{F}}_2 = [\mathcal{F}_{2(1)} \quad \mathcal{F}_{2(2)} \quad \mathcal{F}_{2(3)} \quad \cdots \quad \mathcal{F}_{2(N_S)}]^T \quad (3.33)$$

$$\underline{\mathcal{F}}_3 = [\mathcal{F}_{3(1)} \quad \mathcal{F}_{3(2)} \quad \mathcal{F}_{3(3)} \quad \cdots \quad \mathcal{F}_{3(N_R)}]^T \quad (3.34)$$

$$\underline{\mathcal{F}}_4 = [\mathcal{F}_{4(1)} \quad \mathcal{F}_{4(2)} \quad \mathcal{F}_{4(3)} \quad \cdots \quad \mathcal{F}_{4(N_R-1)}]^T \quad (3.35)$$

$$\underline{\Phi}_S = [\Phi_{S(1)} \quad \Phi_{S(2)} \quad \Phi_{S(3)} \quad \cdots \quad \Phi_{S(N_S)}]^T \quad (3.36)$$

$$\underline{\Phi}_R = [\Phi_{R(1)} \quad \Phi_{R(2)} \quad \Phi_{R(3)} \quad \cdots \quad \Phi_{R(N_R)}]^T \quad (3.37)$$

$$\underline{\Phi}'_R = [\Phi_{R(1)} \quad \Phi_{R(2)} \quad \Phi_{R(3)} \quad \cdots \quad \Phi_{R(N_R-1)}]^T \quad (3.38)$$

$$\begin{bmatrix} \underline{\mathbf{A}}_{11} & \underline{\mathbf{0}} & \underline{\mathbf{0}} & \underline{\mathbf{0}} \\ \underline{\mathbf{0}} & \underline{\mathbf{A}}_{22} & \underline{\mathbf{A}}_{23} & \underline{\mathbf{0}} \\ \underline{\mathbf{0}} & \underline{\mathbf{A}}_{32} & \underline{\mathbf{A}}_{33} & \underline{\mathbf{0}} \\ \underline{\mathbf{0}} & \underline{\mathbf{0}} & \underline{\mathbf{0}} & \underline{\mathbf{A}}_{44} \end{bmatrix} \begin{bmatrix} \underline{\mathcal{F}}_1 \\ \underline{\mathcal{F}}_2 \\ \underline{\mathcal{F}}_3 \\ \underline{\mathcal{F}}_4 \end{bmatrix} = \begin{bmatrix} -\underline{\Phi}_S \\ \underline{\Phi}_S \\ -\underline{\Phi}_R \\ \underline{\Phi}'_R \end{bmatrix} \quad (3.38)$$

Now, in order to provide a relationship between the nodal mmf vectors,  $\underline{\mathcal{F}}_1$ ,  $\underline{\mathcal{F}}_2$ ,  $\underline{\mathcal{F}}_3$ ,  $\underline{\mathcal{F}}_4$ , and the corresponding individual stator and rotor tooth mmf vectors,  $\underline{\mathcal{F}}_S$ ,  $\underline{\mathcal{F}}_R$ , produced by the current carrying coil sides, two additional sets of equations have to be introduced. From Figure 3-11 these equations can be written as follows:

$$\underline{\mathcal{F}}_S = \underline{\mathcal{F}}_2 - \underline{\mathcal{F}}_1 + \underline{\mathfrak{X}}_S \underline{\Phi}_S \quad (3.39)$$

$$\underline{\mathcal{F}}_R = \underline{\mathcal{F}}_3 - \underline{\mathcal{F}}_4 - \underline{\mathfrak{X}}_R \underline{\Phi}_R \quad (3.40)$$

where,  $\underline{\mathcal{F}}_4' = [\mathcal{F}_{4(1)} \quad \mathcal{F}_{4(2)} \quad \mathcal{F}_{4(3)} \quad \cdots \quad \mathcal{F}_{4(N_R-1)} \quad 0]^T$ . Also,  $\underline{\mathfrak{X}}_S$ , and,  $\underline{\mathfrak{X}}_R$ , are diagonal matrices



chapter. Meanwhile, in order to solve the system of algebraic equations of equation (3.38) one needs to provide  $N_S$  stator tooth fluxes. Accordingly, a relationship between the stator phase flux linkages and the individual stator tooth fluxes has to be derived. Also, a relationship between the  $N_S$  stator and  $N_R$  rotor tooth mmfs and three stator phase currents and  $N_R$  rotor currents has to be derived.

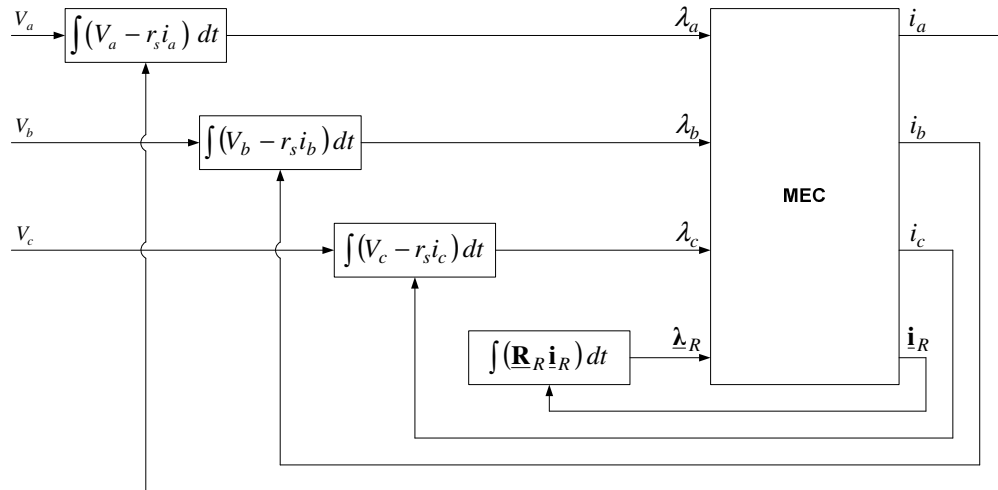


**Figure 3-12.** Block diagram of a squirrel-cage induction machine MEC model (without Mechanical System).

In order to derive a relationship between the stator phase flux linkages,  $\lambda_a$ ,  $\lambda_b$ ,  $\lambda_c$ , and the individual stator tooth fluxes,  $\Phi_S$ , one has to consider the stator winding layout provided in Figure 3-4 from which Figure 3-13 is generated for the purposes at hand. An analytical approach to developing a relationship between the stator phase flux linkages and individual stator tooth fluxes based on parameters such as: the type of the winding, the number of slots, the number coils per phase per slot, the winding connection, etc., has been developed in [68]. In this thesis, however, a graphical approach based on Figure 3-4 will be used. This approach is chosen because it allows one to visualize flux distribution in the machine. It should be noted, however, that the analytical approach developed in [68] is a generalized version of the technique used here. Shown in Figure 3-13 is a winding layout for the first twelve stator slots (one pole span). Also, shown in Figure 3-13 are the individual tooth fluxes and mmfs produced by phases a, b, and c.

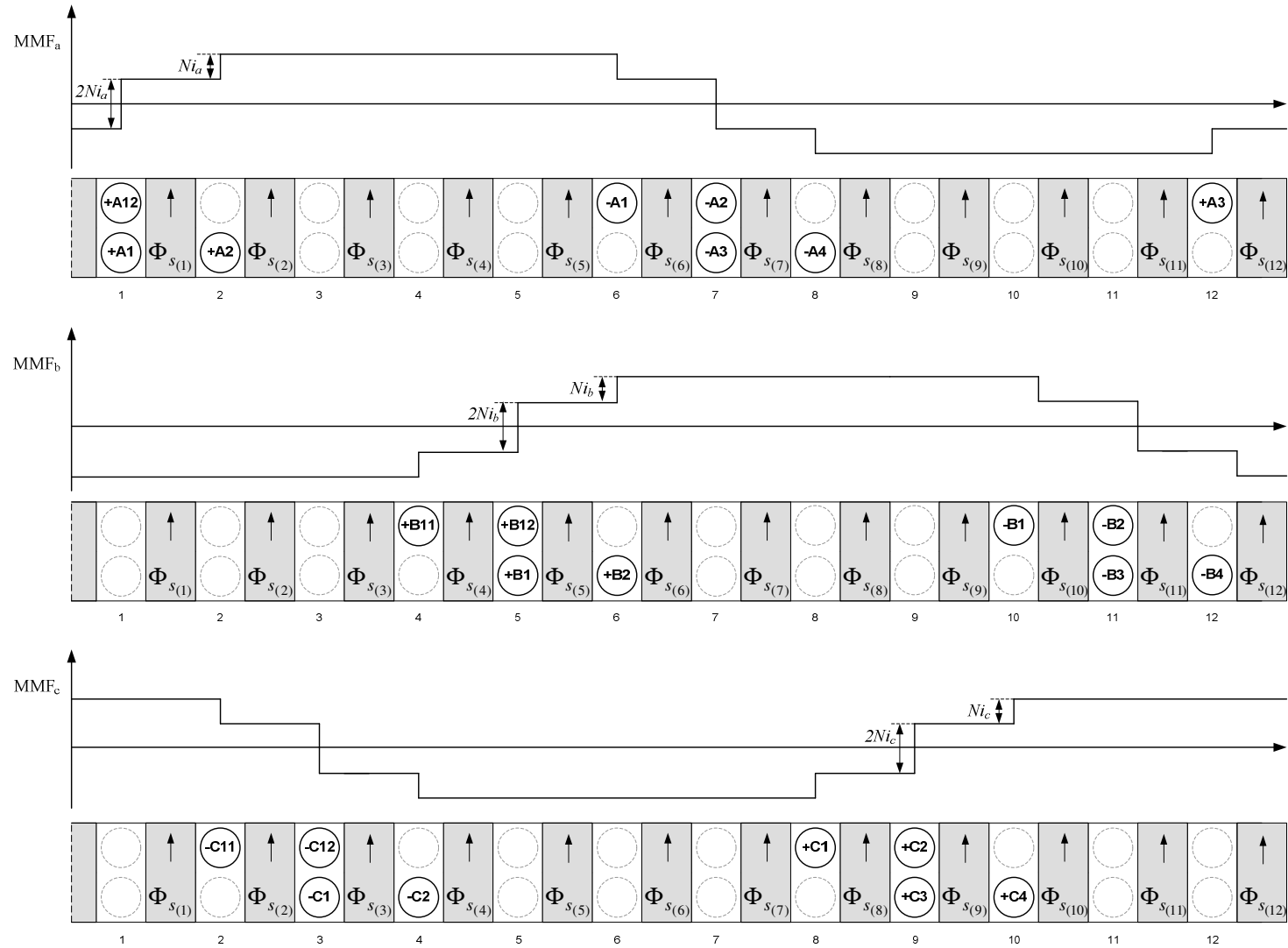


Figure 3-13. Stator winding layout and mmf distribution of phases a, b, and c.

Considering Figure 3-13, and taking into account which individual tooth flux links which coil on a one by one basis, one can write the following relationships between the stator phase flux linkages and the stator tooth fluxes as follows:

$$\lambda_a = N(\Phi_{S(1)} + 2\Phi_{S(2)} + 2\Phi_{S(3)} + 2\Phi_{S(4)} + 2\Phi_{S(5)} + \Phi_{S(6)} \dots + (-1)\Phi_{S(N_s)}) \quad (3.43)$$

$$\lambda_b = N((-2)\Phi_{S(1)} + (-2)\Phi_{S(2)} + (-2)\Phi_{S(3)} + (-1)\Phi_{S(4)} + \Phi_{S(5)} + 2\Phi_{S(6)} \dots + (-2)\Phi_{S(N_s)}) \quad (3.44)$$

$$\lambda_c = N(2\Phi_{S(1)} + \Phi_{S(2)} + (-1)\Phi_{S(3)} + (-2)\Phi_{S(4)} + (-2)\Phi_{S(5)} + (-2)\Phi_{S(6)} \dots + 2\Phi_{S(N_s)}) \quad (3.45)$$

where,  $N$ , is the number of turns per coil. These relationships can be rewritten in matrix notation as given below in (3.46).

$$\begin{bmatrix} \lambda_a \\ \lambda_b \\ \lambda_c \end{bmatrix} = N \begin{bmatrix} 1 & 2 & 2 & 2 & 2 & 1 & \dots & -1 \\ -2 & -2 & -2 & -1 & 1 & 2 & \dots & -2 \\ 2 & -1 & -2 & -2 & -2 & -2 & \dots & 2 \end{bmatrix}_{3 \times N_s} \begin{bmatrix} \Phi_{S(1)} \\ \Phi_{S(2)} \\ \Phi_{S(3)} \\ \Phi_{S(4)} \\ \Phi_{S(5)} \\ \Phi_{S(6)} \\ \vdots \\ \Phi_{S(N_s)} \end{bmatrix}_{N_s \times 1} \quad (3.46)$$

In short matrix form (3.46) can be rewritten as follows:

$$\underline{\lambda}_{abc} = N \underline{\mathbf{w}}' \underline{\Phi}_S \quad (3.47)$$

where the matrix,  $\underline{\mathbf{w}}'$ , has been defined as flux connection matrix in [68]. It should be noticed that flux connection matrix,  $\underline{\mathbf{w}}'$ , is not square and hence cannot be inverted. This means that it is impossible to obtain individual stator tooth fluxes from the knowledge of phase flux linkages alone. The solution to this problem will be discussed later in this chapter.

Again, considering Figure 3-13 along with a complete winding layout of Figure 3-4 one can derive a relationship between the stator phase currents,  $i_a$ ,  $i_b$ ,  $i_c$ , and the individual tooth mmfs,  $\underline{\mathcal{F}}_S$ , as given below in (3.48) through (3.50).

$$\mathcal{F}_{S(1)} = N(i_a + (-2)i_b + 2i_c) \quad (3.48)$$

$$\mathcal{F}_{S(2)} = N(2i_a + (-2)i_b + i_c) \quad (3.49)$$

$$\vdots$$

$$\mathcal{F}_{S(N_s)} = N((-1)i_a + (-2)i_b + 2i_c) \quad (3.50)$$

These relationships can be rewritten in matrix notation as given below in (3.51).

$$\begin{bmatrix} \mathcal{F}_{S(1)} \\ \mathcal{F}_{S(2)} \\ \mathcal{F}_{S(3)} \\ \mathcal{F}_{S(4)} \\ \mathcal{F}_{S(5)} \\ \mathcal{F}_{S(6)} \\ \vdots \\ \mathcal{F}_{S(N_s)} \end{bmatrix}_{N_s \times 1} = N \begin{bmatrix} 1 & -2 & 2 \\ 2 & -2 & 1 \\ 2 & -2 & -1 \\ 2 & -1 & -2 \\ 2 & 1 & -2 \\ 1 & 2 & -2 \\ \vdots \\ -1 & -2 & 2 \end{bmatrix}_{N_s \times 3} \begin{bmatrix} i_a \\ i_b \\ i_c \end{bmatrix}_{3 \times 1} \quad (3.51)$$

In short matrix notation (3.51) can be rewritten as follows:

$$\underline{\mathcal{F}}_S = \underline{\mathbf{w}}'' \underline{\mathbf{i}}_{abc} \quad (3.52)$$

where the matrix,  $\underline{\mathbf{w}}'' = N \begin{bmatrix} 1 & 2 & 2 & 2 & 2 & 1 & \cdots & -1 \\ -2 & -2 & -2 & -1 & 1 & 2 & \cdots & -2 \\ 2 & -1 & -2 & -2 & -2 & -2 & \cdots & 2 \end{bmatrix}^T$ , was defined as the mmf

connection matrix in [68]. Again, it should be noticed that matrix,  $\underline{\mathbf{w}}''$ , is not a square one.

Therefore, it is impossible to obtain stator phase currents directly from the individual stator teeth mmfs.

A similar procedure can be used to develop relationships for the squirrel-cage rotor. Here, the procedure is greatly simplified due to simplicity of the squirrel-cage rotor design. In a squirrel-cage rotor, the teeth fluxes,  $\underline{\Phi}_R$ , are equal to the rotor loop flux linkages,  $\underline{\lambda}_R$ , because of the fact that the number of turns is equal to one for all the rotor circuits. Meanwhile, rotor teeth mmfs,  $\underline{\mathcal{F}}_R$ , are equal to the rotor loop currents. This can also be seen from Figure 3-14. It

should be noted that in Figure 3-14 the loop currents are depicted such that they produce rotor teeth mmfs opposing the teeth fluxes penetrating from the stator. This represents the real physical situation in the machine where rotor currents, according to Faraday’s Law, are responsible for the producing mmfs that oppose the magnetization effect of the stator currents.

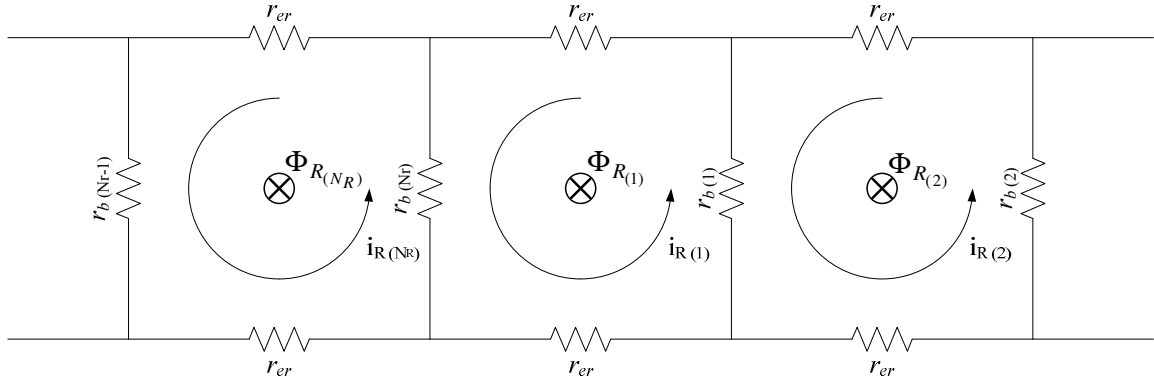


Figure 3-14. Rotor squirrel-cage showing rotor loop currents and teeth fluxes.

The rotor circuits are externally excited by fluxes imposed by the stator excitation. These rotor circuits react (Faraday’s reaction) to these external excitations. Thus, here  $\Phi_{R(1)}$  through  $\Phi_{R(N_R)}$  are the sum of the externally imposed flux by the stator and the flux produced by the reaction of the rotor circuits. Accordingly, the corresponding rotor differential equations can be developed from Figure 3-14 as shown in equations (3.53) through (3.55).

$$\frac{d\lambda_{R(1)}}{dt} = \frac{d\Phi_{R(1)}}{dt} = (i_{R(1)} - i_{R(2)})r_{b(1)} + (i_{R(1)} - i_{R(N_R)})r_{b(N_R)} + 2r_{er}i_{R(1)} \quad (3.53)$$

$$\frac{d\lambda_{R(2)}}{dt} = \frac{d\Phi_{R(2)}}{dt} = (i_{R(2)} - i_{R(3)})r_{b(2)} + (i_{R(2)} - i_{R(1)})r_{b(1)} + 2r_{er}i_{R(2)} \quad (3.54)$$

⋮

$$\frac{d\lambda_{R(N_R)}}{dt} = \frac{d\Phi_{R(N_R)}}{dt} = (i_{R(N_R)} - i_{R(1)})r_{b(N_R)} + (i_{R(N_R)} - i_{R(N_R-1)})r_{b(N_R-1)} + 2r_{er}i_{R(N_R)} \quad (3.55)$$

The system of equation in (3.53) through (3.55) can be rewritten as follows in (3.56) through (3.58).

$$\frac{d\lambda_{R(1)}}{dt} = \frac{d\Phi_{R(1)}}{dt} = (-r_{b(N_R)})i_{R(N_R)} + (r_{b(1)} + r_{b(N_R)} + 2r_{er})i_{R(1)} + (-r_{b(1)})i_{R(2)} \quad (3.56)$$

$$\frac{d\lambda_{R(2)}}{dt} = \frac{d\Phi_{R(2)}}{dt} = (-r_{b(1)})i_{R(1)} + (r_{b(1)} + r_{b(2)} + 2r_{er})i_{R(2)} + (-r_{b(2)})i_{R(3)} \quad (3.57)$$

⋮

$$\frac{d\lambda_{R(N_R)}}{dt} = \frac{d\Phi_{R(N_R)}}{dt} = (-r_{b(N_R-1)})i_{R(N_R-1)} + (r_{b(N_R)} + r_{b(N_R-1)} + 2r_{er})i_{R(N_R)} + (-r_{b(N_R)})i_{R(1)} \quad (3.58)$$

The system of equations in (3.56) through (3.58) can be rewritten in the short matrix form as

follows:

$$\frac{d\lambda_R}{dt} = \frac{d\Phi_R}{dt} = \mathbf{R}_R \mathbf{i}_R \quad (3.59)$$

where,  $\mathbf{R}_R$ , is the rotor resistance matrix and is given in (3.60).

$$\mathbf{R}_R = \begin{bmatrix} r_{R(1)} + r_{R(N_R)} + 2r_{er} & -r_{R(1)} & 0 & \cdots & 0 & -r_{R(N_R)} \\ -r_{R(1)} & r_{R(1)} + r_{R(N_R)} + 2r_{er} & -r_{R(2)} & \cdots & 0 & 0 \\ & & & \vdots & & \\ -r_{R(N_R)} & 0 & 0 & \cdots & -r_{R(N_R-1)} & r_{R(N_R)} + r_{R(N_R-1)} + 2r_{er} \end{bmatrix}_{N_R \times N_R} \quad (3.60)$$

As was mentioned earlier in this chapter both of the stator winding transform matrices,  $\underline{\mathbf{w}}'$ , and,  $\underline{\mathbf{w}}''$ , are not square matrices and hence do not have corresponding inverses. This means that in order to develop a complete MEC model with coupling between the magnetic circuit, depicted in Figure 3-11 and described by equations (3.38) through (3.40), and the corresponding electric circuit, an extended system of algebraic equations has to be developed [68]. This extended system of algebraic equations is given here in (3.61), where the matrices,  $\mathbf{I}$ , and,  $\mathbf{0}$ , are the identity and zero matrices of the appropriate dimensions. Also, the matrix,  $\mathbf{I}_{N_R \times N_R - 1}$ , is given in (3.62) for the sake of completeness of the model formulation. It should also be noticed that dimensions of this extended system of equations are  $(4N_S + 3N_R + (N_R - 1) + 3)$ , where  $N_S$  is the number of stator slots, and  $N_R$  is the number of rotor slots.

$$\begin{bmatrix}
\underline{\mathbf{A}}_{11} & \underline{\mathbf{0}} & \underline{\mathbf{0}} & \underline{\mathbf{0}} & \underline{\mathbf{0}} & \underline{\mathbf{0}} & \underline{\mathbf{I}}_{N_S \times N_S} & \underline{\mathbf{0}} & \underline{\mathbf{0}} \\
\underline{\mathbf{0}} & \underline{\mathbf{A}}_{22} & \underline{\mathbf{A}}_{23} & \underline{\mathbf{0}} & \underline{\mathbf{0}} & \underline{\mathbf{0}} & -\underline{\mathbf{I}}_{N_S \times N_S} & \underline{\mathbf{0}} & \underline{\mathbf{0}} \\
\underline{\mathbf{0}} & \underline{\mathbf{A}}_{32} & \underline{\mathbf{A}}_{33} & \underline{\mathbf{0}} & \underline{\mathbf{0}} & \underline{\mathbf{0}} & \underline{\mathbf{0}} & \underline{\mathbf{0}} & \underline{\mathbf{0}} \\
\underline{\mathbf{0}} & \underline{\mathbf{0}} & \underline{\mathbf{0}} & \underline{\mathbf{A}}_{44} & \underline{\mathbf{0}} & \underline{\mathbf{0}} & \underline{\mathbf{0}} & \underline{\mathbf{0}} & \underline{\mathbf{0}} \\
-\underline{\mathbf{I}}_{N_S \times N_S} & \underline{\mathbf{I}}_{N_S \times N_S} & \underline{\mathbf{0}} & \underline{\mathbf{0}} & -\underline{\mathbf{I}}_{N_S \times N_S} & \underline{\mathbf{0}} & \underline{\mathfrak{R}}_S & \underline{\mathbf{0}} & \underline{\mathbf{0}} \\
\underline{\mathbf{0}} & \underline{\mathbf{0}} & -\underline{\mathbf{I}}_{N_R \times N_R} & \underline{\mathbf{I}}_{N_R \times N_R - 1} & \underline{\mathbf{0}} & \underline{\mathbf{0}} & \underline{\mathbf{0}} & \underline{\mathbf{I}}_{N_R \times N_R} & \underline{\mathbf{0}} \\
\underline{\mathbf{0}} & \underline{\mathbf{0}} & \underline{\mathbf{0}} & \underline{\mathbf{0}} & \underline{\mathbf{I}}_{N_S \times N_S} & -\underline{\mathbf{w}}'' & \underline{\mathbf{0}} & \underline{\mathbf{0}} & \underline{\mathbf{0}} \\
\underline{\mathbf{0}} & \underline{\mathbf{0}} & \underline{\mathbf{0}} & \underline{\mathbf{0}} & \underline{\mathbf{0}} & \underline{\mathbf{0}} & \underline{\mathbf{w}}' & \underline{\mathbf{0}} & \underline{\mathbf{0}} \\
\underline{\mathbf{0}} & \underline{\mathbf{I}}_{N_R \times N_R} & -\underline{\mathbf{I}}_{N_R \times N_R}
\end{bmatrix}
\begin{bmatrix}
\underline{\mathcal{F}}_1 \\
\underline{\mathcal{F}}_2 \\
\underline{\mathcal{F}}_3 \\
\underline{\mathcal{F}}_4 \\
\underline{\mathcal{F}}_S \\
\underline{\mathbf{i}}_{abc} \\
\underline{\Phi}_S \\
\underline{\mathcal{F}}_R \\
\underline{\mathbf{i}}_R
\end{bmatrix}
=
\begin{bmatrix}
\underline{\mathbf{0}} \\
\underline{\mathbf{0}} \\
-\underline{\Phi}_R \\
\underline{\Phi}_R \\
\underline{\mathbf{0}} \\
-\underline{\mathfrak{R}}_R \underline{\Phi}_R \\
\underline{\mathbf{0}} \\
\underline{\lambda}_{abc} / N \\
\underline{\mathbf{0}}
\end{bmatrix}
\quad (3.61)$$

$$\underline{\mathbf{I}}_{N_R \times N_R - 1} = \begin{bmatrix} 1 & 0 & 0 & 0 \\ 0 & 1 & 0 & 0 \\ & & \ddots & \\ 0 & 0 & 0 & 1 \\ 0 & 0 & 0 & 0 \end{bmatrix}_{N_R \times N_R - 1} \quad (3.62)$$

It is important to note that in order to solve the system of equations provided in (3.62) a technique such as the iterative Gauss-Seidel needs to be used [74]. Also, as was mentioned earlier in this chapter, it is assumed that no radial slot leakage flux exists. Hence, the system in equation (3.61) can be simplified as has been shown in [70] and is depicted here in (3.63) through (3.68) for the sake of completeness and the reader's convenience. Depending on the type of algorithm used for matrix inversion, this simplification may result in significant reduction of computer execution time of the model.

$$\begin{aligned} & \left[ \begin{array}{c} \underline{\mathbf{w}}' \\ \underline{\mathbf{A}}_{11} (\underline{\mathbf{A}}_{22} - \underline{\mathbf{A}}_{23} \underline{\mathbf{A}}_{33}^{-1} \underline{\mathbf{A}}_{32})^{-1} + (\underline{\mathbf{A}}_{11} \underline{\mathfrak{R}}_S + \underline{\mathbf{I}}_{N_S \times N_S}) - \underline{\mathbf{A}}_{11} \underline{\mathbf{w}}'' \end{array} \right] \begin{bmatrix} \underline{\Phi}_S \\ \underline{\mathbf{i}}_{abc} \end{bmatrix} \\ & = \left[ \begin{array}{c} \frac{\lambda_{abc}}{N_{C_{phase}} N} \\ \underline{\mathbf{A}}_{11} (\underline{\mathbf{A}}_{22} - \underline{\mathbf{A}}_{23} \underline{\mathbf{A}}_{33}^{-1} \underline{\mathbf{A}}_{32})^{-1} \underline{\mathbf{A}}_{23} \underline{\mathbf{A}}_{33}^{-1} \underline{\Phi}_R \end{array} \right] \end{aligned} \quad (3.63)$$

Where,  $N_{C_{phase}}$ , is the number of coils per phase.

$$\underline{\mathcal{F}}_2 = (\underline{\mathbf{A}}_{22} - \underline{\mathbf{A}}_{23} \underline{\mathbf{A}}_{33}^{-1} \underline{\mathbf{A}}_{32})^{-1} (\underline{\Phi}_S + \underline{\mathbf{A}}_{23} \underline{\mathbf{A}}_{33}^{-1} \underline{\Phi}_R) \quad (3.64)$$

$$\underline{\mathcal{F}}_3 = -\underline{\mathbf{A}}_{33}^{-1} (\underline{\Phi}_R + \underline{\mathbf{A}}_{32} \underline{\mathcal{F}}_2) \quad (3.65)$$

$$\underline{\mathcal{F}}_4 = \underline{\mathbf{A}}_{44}^{-1} \underline{\Phi}_R' \quad (3.66)$$

$$\underline{\mathcal{F}}_R = \underline{\mathcal{F}}_3 - \underline{\mathcal{F}}_4 - \underline{\mathfrak{R}}_R \underline{\Phi}_R \quad (3.67)$$

$$\underline{\mathbf{i}}_R = \underline{\mathcal{F}}_R \quad (3.68)$$

Now, that electrical and magnetic behavior of the induction machine has been defined, it is possible to couple the machine to the mechanical load as shown in Figure 3-15. The expression for electromagnetic torque can be derived from the MEC model directly, as has been done in [68] based on electromechanical energy conversion principles, and is given as follows:

$$T_{em} = \frac{1}{2} \sum_{m=1}^{N_S} \sum_{n=1}^{N_R} (\mathcal{F}_{2(m)} - \mathcal{F}_{3(n)})^2 \frac{dP_{AG(m,n)}}{d\theta_R} \quad (3.69)$$

where,  $\theta_R$ , is the rotor position in mechanical measure.

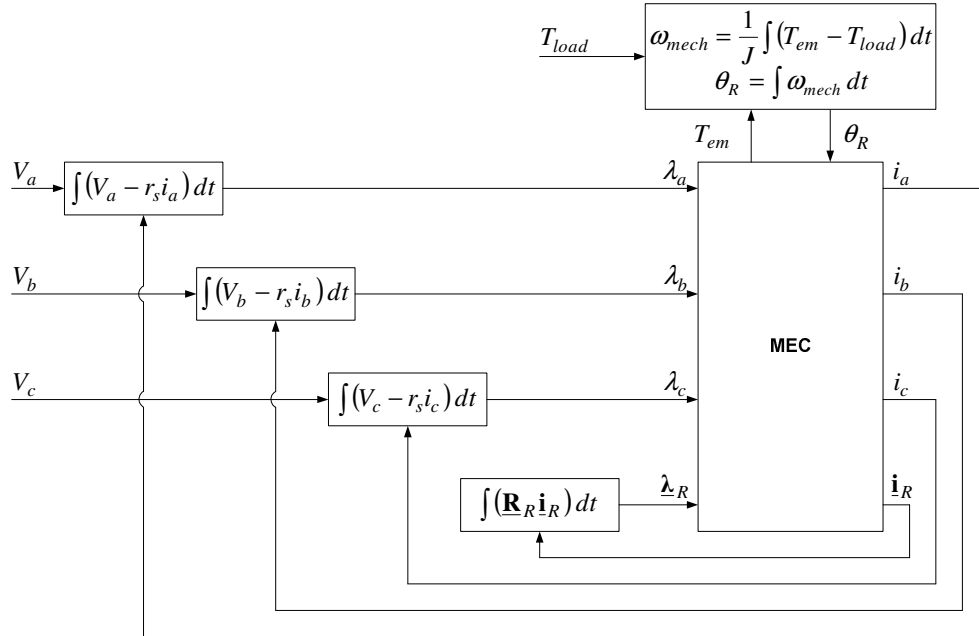


Figure 3-15. Block diagram of a complete squirrel-cage induction machine MEC model.

As has been mentioned earlier in this chapter there are three types of permeances in the MEC model of an electric machine, namely, constant, inherently nonlinear, and parametric nonlinear. Constant permeances are defined as the permeances of the regions with linear magnetic properties and constant geometry. On the other hand, inherently nonlinear permeances are defined as being dependent on the properties of nonlinear magnetic materials. These permeances are used to model the core of the machine. Meanwhile, parametric nonlinear permeances are defined as permeances dependent on the geometry of the region and are used to model the air gap region. A detailed derivation of various parameters used in the MEC model of a 5-hp induction motor is provided in an Appendix to this thesis.

### 3.3 FINITE ELEMENT MODEL

In this section the development of the Time-Stepping Finite Element (TSFE) model will be discussed. It should be noted that the TSFE model used in this thesis has been implemented in the commercially available software package, namely MAGSOFT (Flux 2D). This software package allows the user to develop a TSFE model by inputting all relevant design data such as machine geometry, material properties, winding layout, etc., while not involving the user in the details of the finite element formulation programming and solution. In other words, the user does not need to know the details of the inner workings of the TSFE modeling approach, but rather be familiar with some basic principles behind it. Hence, this chapter will present some basic principles of the TSFE modeling approach rather than providing a detailed explanation of the model's formulation development process.

As has been shown earlier in this chapter, Maxwell's Equations can be simplified for low-frequency (quasi-static) applications when only inductive coupling exists between the electric field intensity,  $\vec{E}$ , and the magnetic field intensity,  $\vec{H}$ . That is, the magnetic field intensity,  $\vec{H}$ , is dependent only on the conduction current density,  $\vec{J}$ , in which case the displacement current density,  $\frac{\partial \vec{D}}{\partial t}$ , is negligible as is the case in the majority of electric machinery problems. Again, this simplified set of Maxwell's Equations is given here for reader's convenience:

$$\nabla \times \vec{H} = \vec{J} \quad (\text{Ampere's Law original definition}) \quad (3.70)$$

$$\nabla \cdot \vec{B} = 0 \quad (\text{Gauss' Law for Magnetism}) \quad (3.71)$$

$$\nabla \times \vec{E} = -\frac{\partial \vec{B}}{\partial t} \quad (\text{Faraday's Law}) \quad (3.72)$$

where, the auxiliary equations relating the magnetic flux density,  $\vec{B}$ , and the magnetic field intensity,  $\vec{H}$ , and the electric field,  $\vec{E}$ , to the current density,  $\vec{J}$ , are provided in equations (3.73) and (3.74), respectively.

$$\vec{B} = \mu \vec{H} \quad (3.73)$$

$$\vec{J} = \sigma \vec{E} \quad (3.74)$$

It should be noted that a similar simplified set of Maxwell's Equations can be derived for the case of low-frequency, electrostatic or quasi-static, electric fields [74].

One approach to solving finite element type numerical problems is by introducing an energy functional that has to be minimized [74-76]. In static and quasi-static magnetic fields such a functional can be based on the current density and the corresponding magnetic vector potential [74]. In other words, the functional, in this case a difference between the input and stored magnetic energies, can be derived in terms of the current density and the corresponding magnetic vector potential. Meanwhile, magnetic vector potential (MVP),  $\vec{A}$ , can be related to the magnetic flux density,  $\vec{B}$ , as given below in (3.75). This is possible by applying the null identity ( $\nabla(\nabla \times \vec{A}) \equiv 0$ ) to equation (3.71). In other words, considering (3.71) and the null identity it can be stated that the magnetic flux density must be the curl of some vector field,  $\vec{A}$ , as shown in (3.75). The advantage of using the magnetic vector potential stems from the fact that all parameters used to characterize magnetic fields, such as, the magnetic field intensity,  $\vec{H}$ , and the magnetic flux density,  $\vec{B}$ , are readily available from the magnetic vector potential,  $\vec{A}$ , and hence the need of using multiple physical quantities to characterize the field is eliminated.

$$\vec{B} = \nabla \times \vec{A} \quad (3.75)$$

Moreover, the MVP,  $\vec{A}$ , can be related to the current density,  $\vec{J}$ , by first expressing (3.73) as:

$$\vec{H} = \frac{1}{\mu} \vec{B} \quad (3.76)$$

then, substituting (3.75) into (3.76) thus yielding the following:

$$\vec{H} = \frac{1}{\mu} (\nabla \times \vec{A}) \quad (3.77)$$

Finally, substituting (3.77) into the expression for Ampere's Law previously provided in (3.70), as shown in (3.78).

$$\nabla \times \left( \frac{1}{\mu} (\nabla \times \vec{A}) \right) = \vec{J} \quad (3.78)$$

Expression in (3.78), when applied to static magnetic field problems, provides the basis for the TSFE method. In other words, the solution of (3.78) is the principal equation to be solved using finite element method [76]. It should be pointed out, however, that in order to extend (3.78) to the quasi-static (low-frequency field) problems one has to consider Faraday's Law provided in (3.72). Substituting for the magnetic flux density,  $\vec{B}$ , from (3.75) into (3.72) yields the following:

$$\nabla \times \vec{E} = -\nabla \times \frac{\partial \vec{A}}{\partial t} \quad (3.79)$$

where,  $\nabla \times \vec{E}$ , can be rewritten using the identity which states that the curl of any vector is equal to the sum of the curl of the vector and a gradient of some scalar field function, as follows:

$$\nabla \times \vec{E} = \nabla \times (\vec{E} + \nabla V) \quad (3.80)$$

where,  $V$ , is a scalar field function. Substituting equation (3.80) in (3.79) and integrating yields the following result:

$$\vec{E} + \nabla V = -\frac{\partial \vec{A}}{\partial t} \quad (3.81)$$

Now, using (3.81), current density,  $\vec{J}$ , can be expressed as:

$$\vec{J} = -\sigma \left( \nabla V + \frac{\partial \vec{A}}{\partial t} \right) \quad (3.82)$$

where, the first term on the right hand-side,  $\sigma(\nabla V)$ , is the current density impressed by the outside voltage source and the second term,  $\sigma \left( \frac{\partial \vec{A}}{\partial t} \right)$ , represents the current density induced as the result of the time-varying magnetic field. Hence, using equation (3.82) one can rewrite (3.78) for use in quasi-static field problems, such as the problem of induction machines at hand, is given in (3.83) below.

$$\nabla \times \left( \frac{1}{\mu} (\nabla \times \vec{A}) \right) = -\sigma \left( \nabla V + \frac{\partial \vec{A}}{\partial t} \right) \quad (3.83)$$

It should be noted that the expression provided in (3.83) can be utilized for the solution of both two and three dimensional problems. Hence, a somewhat simplified version of (3.83) is utilized in the MAGSOFT (Flux 2D) software package to solve for the magnetic field distribution in the machine. This expression is given in [75], and in expanded two-dimensional magnetic field formulation can be written as follows:

$$\frac{\partial}{\partial x} \left( \frac{1}{\mu} \frac{\partial A_z}{\partial x} \right) + \frac{\partial}{\partial y} \left( \frac{1}{\mu} \frac{\partial A_z}{\partial y} \right) = -\sigma \left( \nabla V + \frac{\partial A_z}{\partial t} \right) \quad (3.83)$$

The time-stepping finite element (TSFE) model used in this thesis is utilized to model both healthy and faulty operation of the case-study 5-hp squirrel-cage induction machine. A half of the cross-section of the 5-hp squirrel-cage induction machine showing a large number of finite elements is depicted in Figure 3-16. As can be seen from Figure 3-16, there are two regions where the density of the finite elements is especially high. Namely, these regions are, the air gap, and the rotor slots with surrounding regions. As was mentioned earlier, it is particularly important

to model the air gap as accurately as possible, since the energy conversion takes place in the air gap. In the case of the squirrel-cage rotor with deep-bar rotor slot design, one has to generate a relatively high number of finite elements in the rotor slots to account for the deep-bar effect (skin effect) for accurate starting transient simulations purpose. Therefore, both models used in this work can be utilized in both steady-state and starting transient studies. It should be pointed out, however, that in this thesis centering on broken bar fault diagnostics, only the steady-state operation of the machine will be considered. Hence, this makes the need for accurate simulation of deep-bar effects unnecessary. Accordingly, the need for such a high density of elements in the rotor slot region is not necessary.

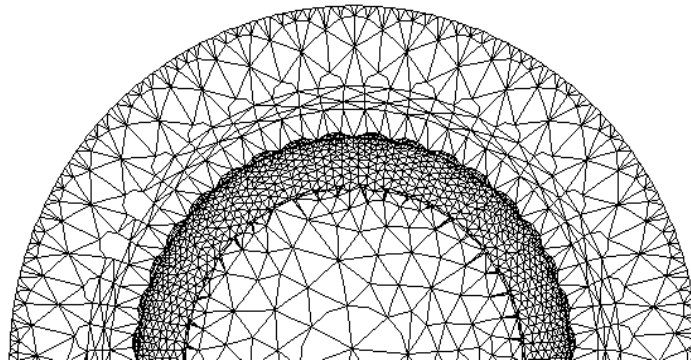


**Figure 3-16.** Cross-section of the 5-hp squirrel-cage induction machine with finite element grid.

### 3.4 MODEL VALIDATION

In this section, MEC and TSFE models developed earlier will be verified by comparing the results of the simulations with experimentally obtained data of healthy and one broken bar motor operation. These models will be validated in three steps. First, the validity of MEC and TSFE models will be verified at steady-state rated load conditions. Second, the validity of MEC model will be verified at steady-state conditions under different loads. Third, the validity of the two modeling approaches for rotor fault modeling under steady-state rated load condition will also be verified for the one broken bar case.

Here, rated load steady-state operation will be considered. Depicted in Figures 3-17 and 3-18 are the time-domain waveform and the corresponding frequency spectrum of the phase-a current obtained via the MEC simulation of the rated load condition. Also, depicted in Figure 3-19 and 3-20 are the corresponding time-domain waveform and frequency spectrum of the phase-a current obtained via the TSFE simulation of the rated load condition. Meanwhile, shown in Figures 3-21 and 3-22 are the time-domain profile and the corresponding frequency spectrum of the phase-a current obtained during the experimental test under rated load condition. It should be noticed that both MEC and TSFE models are in relatively good agreement with the experimental test data. Also, provided in Table 3-1 are the tabulated data of the steady-state performance characteristics at different load conditions, namely, torque, speed, and power factor. Again, from Table 3-1 it should be noted that both models are in relatively close agreement with the experimental test.

<b>100% (30Nm)</b>	<b>MEC</b>	<b>TSFE</b>	<b>Test</b>
Current, [ $A_{rms}$ ]	6.10	6.04	6.15
Speed, [r/min]	1166	1166	1165
Power factor, [%]	82.9	84.3	79.7
<b>75% (22.5Nm)</b>	<b>MEC</b>	<b>TSFE</b>	<b>Test</b>
Current, [ $A_{rms}$ ]	4.83	4.64	4.75
Speed, [r/min]	1175	1175	1175
Power factor, [%]	76.8	77.2	74.2
<b>50% (15Nm)</b>	<b>MEC</b>	<b>TSFE</b>	<b>Test</b>
Current, [ $A_{rms}$ ]	3.91	3.82	3.95
Speed, [r/min]	1184	1183	1182
Power factor, [%]	67.5	70.2	66.5

**Table 3-1.** Steady-state performance characteristics (MEC, TSFE, and Test).

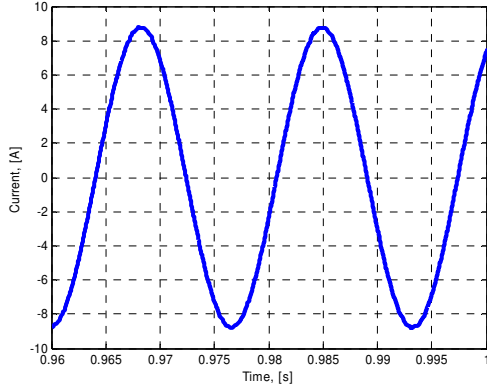


Figure 3-17. Time-domain profile of phase-a current (MEC).

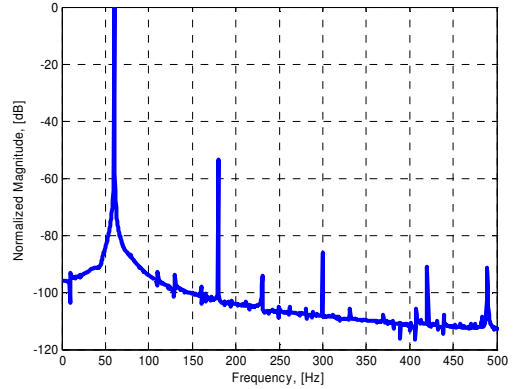


Figure 3-18. Frequency spectrum profile of phase-a current (MEC).

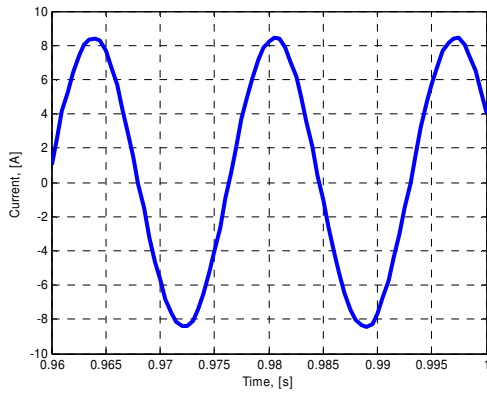


Figure 3-19. Time-domain profile of phase-a current (TSFE).

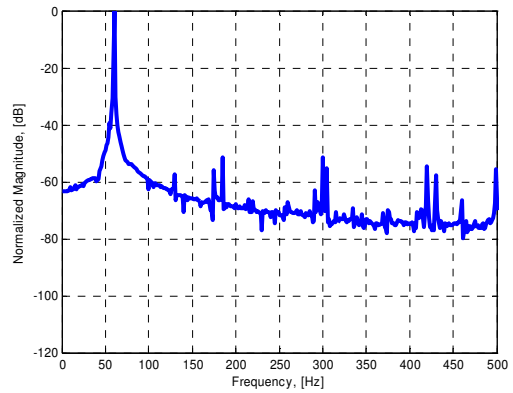


Figure 3-20. Frequency spectrum profile of phase-a current (TSFE).

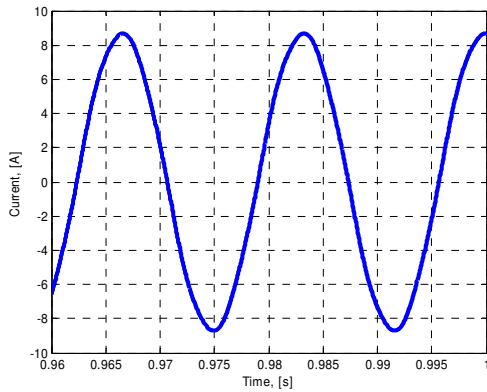


Figure 3-21. Time-domain profile of phase-a current (Experimental Test).

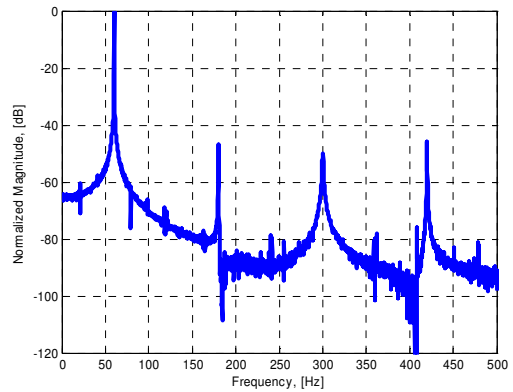
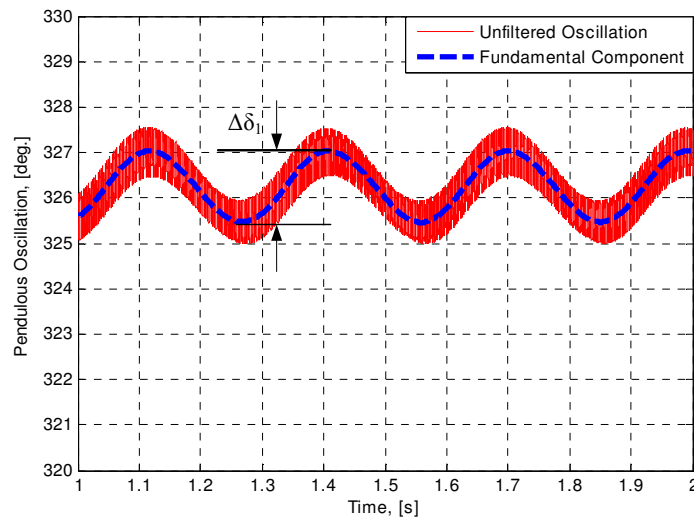
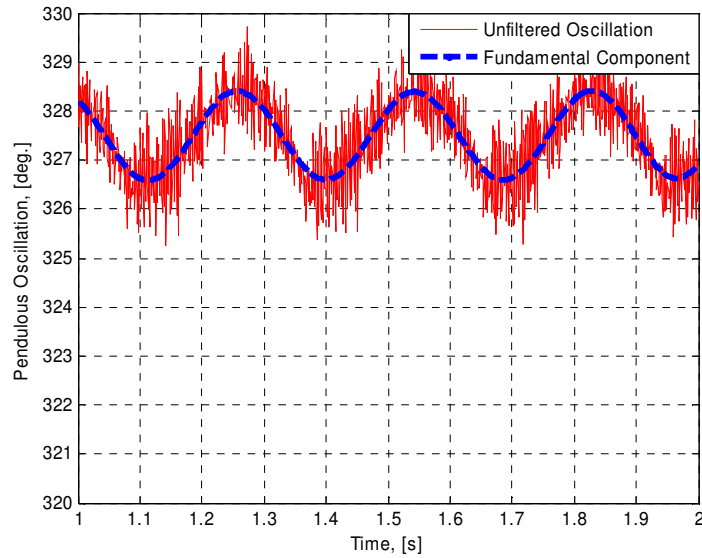


Figure 3-22. Frequency spectrum profile of phase-a current (Experimental Test).

Here, the validity of both models for rotor fault modeling will be verified based on the analysis of one broken rotor bar fault. Depicted in Figures 3-23 through 3-25 are pendulous oscillation profiles [46] for both MEC and TSFE models as well as the experimental test. The values of corresponding swing angles,  $\Delta\delta_1$ , are provided in Table 3-2. The swing angle,  $\Delta\delta_1$ , has been defined in [46] as the peak-to-peak value of the fundamental component of the so-called pendulous oscillation. Also, provided in Table 3-2 are the values of the lower side-band component (LSB) obtained by performing spectral analysis on the phase-a currents from one broken bar simulations of MEC and TSFE models as well as from the experimental test. From Figures 3-23 through 3-25 and Table 3-2, one should notice that the both lower side-band and swing-angle data yielded relatively accurate results for both modeling approaches, when compared to the experimental test results. It should be mentioned that details of the fault diagnostics techniques, namely, MCSA and Pendulous Oscillation method, used to compare the performance of both models will be discussed in Chapter 4.



**Figure 3-23.** Pendulous Oscillation,  $\Delta\delta_1 = 1.5^\circ$  (MEC).



**Figure 3-24.** Pendulous Oscillation,  $\Delta\delta_1=1.8^\circ$  (TSFE).

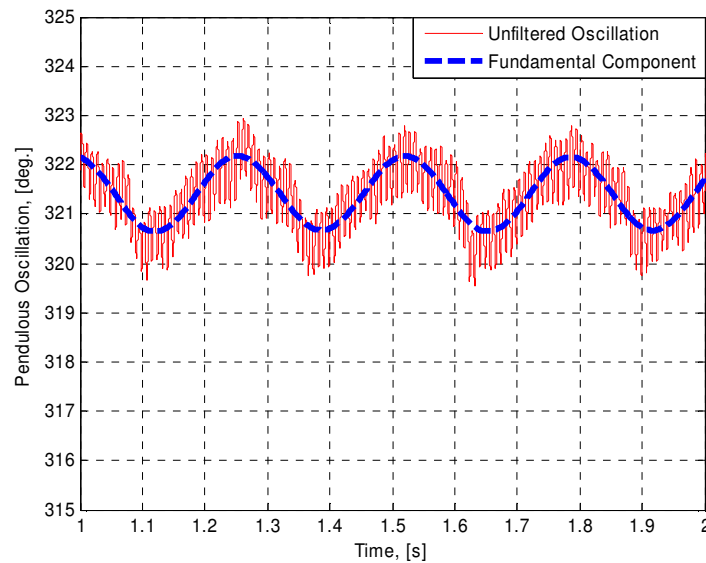


**Figure 3-25.** Pendulous Oscillation,  $\Delta\delta_1=1.6^\circ$  (Experimental Test).

Fault Indices	MEC	TSFE	Test
LSB, [dB]	-44.64	-40.39	-44.7
Swing angle, $\Delta\delta_1$ , [deg.]	1.5	1.8	1.6

**Table 3-2.** Values of lower side-band component (LSB) and swing angle,  $\Delta\delta_1$ , under conditions of one broken rotor bar.

## CHAPTER 4: ROTOR FAULT DIAGNOSTICS

---

### 4.1 INTRODUCTION

**T**HIS chapter will describe two diagnostic techniques that have been previously established in the literature. Both of these techniques have proven to be reliable for diagnostics of adjacent rotor bar breakages. The main purpose of this chapter is to establish the necessary background required for rotor fault analysis that will follow in the consequent chapters. Hence, this chapter will concentrate on the basic application of these techniques to rotor fault diagnostics in squirrel-cage induction machines. The secondary goal of this chapter is to continue validation of the models presented in Chapters 2 and 3.

### 4.2 MOTOR CURRENT SIGNATURE ANALYSIS (MCSA)

Spectrum analysis of induction machine line currents, also known as motor current signature analysis (MCSA), is one of the most commonly used rotor fault diagnostic techniques [38-40]. In this technique side-bands adjacent to the supply fundamental frequency component present in the frequency spectrum of motor currents are used to diagnose the extent of the fault. As has been shown in Chapter 2, in the case of a broken bar fault the magnetic field produced by the rotor will oscillate at twice the slip frequency,  $2s\omega_{syn}$ . According to Faraday's Law this oscillating magnetic field will induce an electromotive force, emf, in the stator windings, which in turn will result in the stator current component at the same,  $2s\omega_{syn}$ , frequency. However, since

the magnetic field produced by rotor currents is also moving in space at synchronous speed this will also induce an emf and the consequent current at synchronous frequency,  $\omega_{\text{syn}}$ . Moreover, since, in the motoring region, the squirrel-cage rotor structure is moving at a speed lower than synchronous the resulting stator emf and the corresponding stator current will have a component at a frequency equal to  $(\omega_{\text{syn}} - 2s \omega_{\text{syn}}) = \omega_{\text{syn}}(1-2s)$ . This,  $\omega_{\text{syn}}(1-2s)$ , frequency component in the stator current spectrum can be used for rotor fault diagnostic purposes, and is usually referred to as the Lower Side-Band (LSB) component. Depicted in Figures 4-1 through 4-4 are the stator line current spectra under healthy and one broken rotor bar conditions. One should notice the lack of distinguishable Lower Side-Band component in the line current spectrum of the healthy machine. On the other hand, in the case of one broken bar there is a detectable LSB component. Moreover, as one can see from Figures 4-3 and 4-4 there is an additional component at a frequency equal  $\omega_{\text{syn}}(1+2s)$ . This,  $\omega_{\text{syn}}(1+2s)$ , is commonly referred to as the Upper Side-Band (USB) component. The existence of this Upper Side-Band component can be traced back to the Lower Side-Band component. In other words, the current component at  $\omega_{\text{syn}}(1-2s)$  produces a consequent torque pulsation at twice the slip frequency,  $2s\omega_{\text{syn}}$ . This torque pulsation may in turn result in the consequent speed pulsations at the same frequency,  $2s\omega_{\text{syn}}$ , which will produce a component in the stator current at  $\omega_{\text{syn}}(1+2s)$ . This process of interaction of stator current harmonics, torque oscillation, and the consequent speed ripple will continue to induce stator current harmonics at  $(1 \pm ks) \omega_{\text{syn}}$  (where  $k=2, 4, 6 \dots$ ). However, the existence of a detectable speed ripple and the consequent Upper Side-Band component is not guaranteed in the cases where the total inertia of the motor-load system is high. This dependency of the magnitude of the Upper Side-Band component on the motor-load inertia has been studied in detail in [46]. It should also be mentioned that both LSB and USB components are heavily dependent on the load conditions. More specifically, both LSB and the consequent USB components tend to become diminished at light loads, as has been shown in [44] and [46].

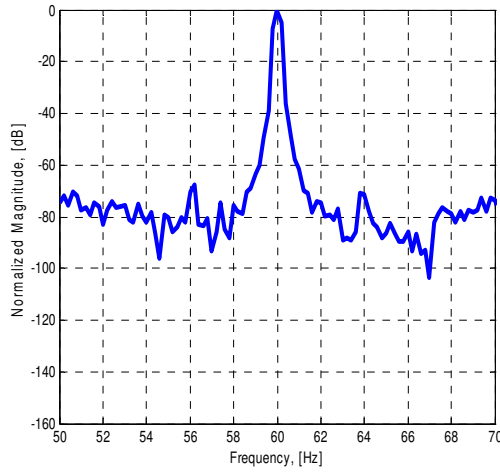


**Figure 4-1.** Stator line current spectrum of 5-hp induction machine under healthy full-load conditions (from Experimental Test).

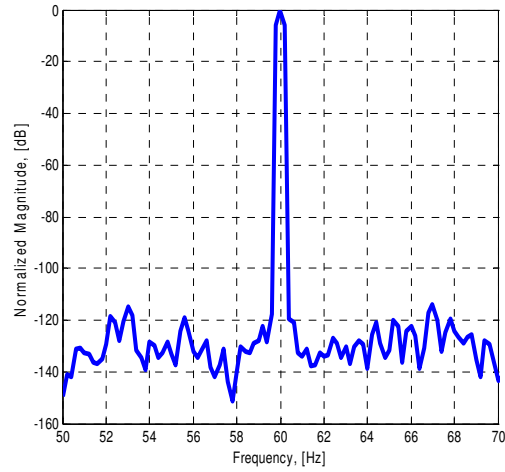


**Figure 4-2.** Stator line current spectrum of 5-hp induction machine under healthy full-load conditions (from MEC Simulation).

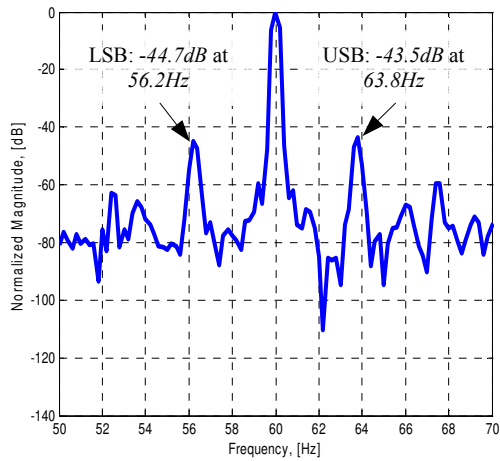


**Figure 4-3.** Stator line current spectrum of 5-hp induction machine under one broken bar full-load conditions (from Experimental Test).

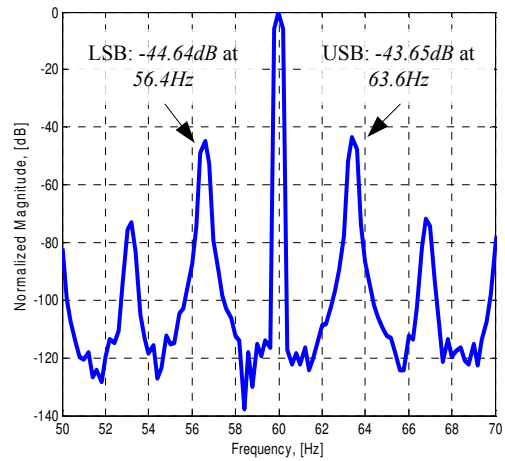


**Figure 4-4.** Stator line current spectrum of 5-hp induction machine under one broken bar full-load conditions (from MEC Simulation).

Depicted in Figure 4-5 and 4-6 are the values of LSB components for one through four adjacent broken squirrel-cage rotor bars. From comparison of both figures, one should notice that MEC model results are in close agreement with results obtained during the laboratory testing. This can also be seen from the recorded data of Table 4-1.

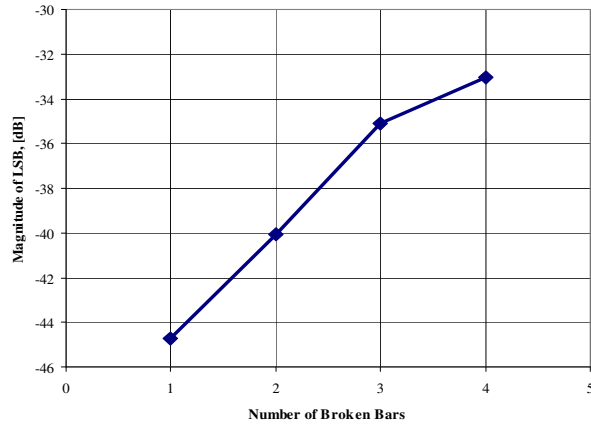


**Figure 4-5.** Lower Side-Band component versus number of broken bars under full-load conditions (from Experimental Tests).

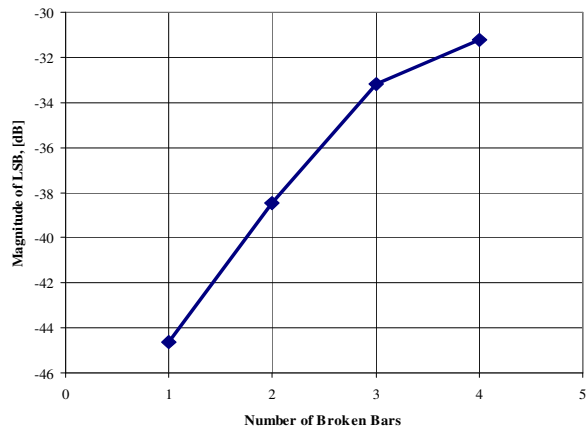


**Figure 4-6.** Lower Side-Band component versus number of broken bars under full-load conditions (from MEC Simulations).

Test			MEC		
Number of BB	Magnitude, [dB]	Frequency, [Hz]	Number of BB	Magnitude, [dB]	Frequency, [Hz]
1	-44.70	56.2	1	-44.64	56.4
2	-40.05	56.4	2	-38.48	56.6
3	-35.10	56.6	3	-33.20	56.4
4	-33.05	56.6	4	-31.24	56.4

**Table 4-1.** LSB component under full-load conditions (from Experimental Tests and MEC Simulations).

The major advantage of the MCSA based diagnostic approach is the fact that it utilizes a single current sensor. This current sensor is used to record the time-domain profile of one of the line currents, which can later be processed to obtain the corresponding spectrum. However, since only a finite number of current measurements can be recorded over time, due to memory and processing time limitations, this technique suffers from common shortcomings associated with finite-length Fast Fourier Transform (FFT) analysis. These shortcomings have been described in detail in [46] and are repeated in summary here for reader's convenience. Namely, these shortcomings are: difficulties associated with nonstationary signals, the side-lobe leakage phenomenon, frequency resolution limited by the sampling frequency,  $f_{sampling}$ , and sample length,  $N$ , as  $\Delta f = (1 / N)f_{sampling}$ , etc. These difficulties can be partially mitigated by applying Hanning Windowing to the data prior to the FFT analysis [46]. It should be mentioned that the (MEC) simulation and experimental data used in this thesis for spectral analysis purposes were sampled at a frequency,  $f_{sampling} = 50kHz$ , over *5second* time intervals. Moreover, the Hanning Window approach was applied over a complete data set of *5seconds* ( $N=250,000$ ) in order to mitigate some of the problems described above.

### 4.3 MAGNETIC FIELD PENDULOUS OSCILLATION (MFPO)

A so-called magnetic field pendulous oscillation (MFPO) technique, where time-domain values of motor line currents and voltages are used to generate the corresponding space-vectors and the oscillation of the angle between these space-vectors is used as the fault index, has been introduced in [43-46]. Again, referring back to Chapter 2 where it has been shown that a broken bar results in the oscillation of the rotor mmf around its healthy axis at twice the slip frequency,  $2s\omega_{syn}$ , one can take a different approach from that chosen in MCSA analysis. Considering the overall effect of the rotor fault on the resultant magnetic field distribution in the machine, one can

deduce that the oscillation of the rotor mmf will result in the corresponding oscillation of the resultant (stator and rotor) mmf. As has been shown in [43-46], this oscillation of the resultant mmf can be observed by monitoring the position of the stator current space-vector,  $\vec{i}_s(t)$ . More specifically, the relative motion of the stator current space-vector,  $\vec{i}_s(t)$ , with respect to the stator voltage space-vector,  $\vec{v}_s(t)$ , can be used for diagnostics purposes [43-46]. Using three voltage and current measurements, stator current and voltage space-vectors can be calculated as follows [43-46]:

$$\vec{i}_s(t) = \frac{2}{3} \left( (i_a(t) - i_b(t)) + \alpha(i_b(t) - i_c(t)) + \alpha^2(i_c(t) - i_a(t)) \right) \quad (4.1)$$

$$\vec{v}_s(t) = \frac{2}{3} \left( v_{ab}(t) + \alpha(v_{bc}(t)) + \alpha^2(v_{ca}(t)) \right) \quad (4.2)$$

where,  $\alpha$ , is the complex space-vector operator provided in (4.3).

$$\alpha = e^{j\frac{2\pi}{3}} \quad (4.3)$$

In the case of a floating stator winding neutral,  $i_a(t) + i_b(t) + i_c(t) = 0$ , equation (4.1) can be simplified as shown in (4.4) [46]. Moreover, (4.2) can be rewritten in terms of two line-to-line voltages as provided in (4.5) [46].

$$\vec{i}_s(t) = (i_a(t) - i_b(t)) + j\sqrt{3}(i_a(t) + i_b(t)) \quad (4.4)$$

$$\vec{v}_s(t) = v_{ab}(t) + j \frac{v_{ab}(t) + 2v_{bc}(t)}{\sqrt{3}} \quad (4.5)$$

It should be noticed from (4.4) and (4.5) that only two current and two voltage sensors are needed to form the voltage and current space-vectors required for purposes of fault diagnostics.

Meanwhile, the pendulous oscillation angle,  $\delta(t)$ , is defined in [43-46] as the angle between the current and voltage space-vectors can hence be expressed as follows:

$$\delta(t) = \angle \vec{i}_s(t) - \angle \vec{v}_s(t) \quad (4.6)$$

Furthermore,  $\delta_1(t)$ , is the fundamental component of the pendulous oscillation, and the swing angle,  $\Delta\delta_1$ , is the peak-to-peak value of the fundamental component of pendulous oscillation,  $\delta_1(t)$ . In this diagnostics technique the swing angle,  $\Delta\delta_1$ , is considered as the fault index which can be used to diagnose the extent of the fault. Here, the swing angle,  $\Delta\delta_1$ , is similar to the Lower Side-Band component of the MCSA diagnostics approach in the sense that both LSB and swing angle,  $\Delta\delta_1$ , are used as fault indices.

The pendulous oscillation is a time-domain phenomenon and hence can be easily correlated with the physical processes taking place in the machine during the fault. Here, this property of the MFPO will be used to further verify the simplified analysis presented in Chapter 2, as well as to gain a better understanding of the effects of the fault. In Chapter 2 it has been stated that the highest distortion of rotor mmf axis occurs at time instants when the breakage reaches the locations half way between the bar carrying maximum absolute value of the current and the bar carrying no current. In other words, the when breakage is  $45^\circ$  (electrical) from the bar carrying maximum absolute value of the current the breakage has the largest impact on the orientation of the rotor mmf axis. In the simple 8-bar squirrel-cage rotor of Chapter 2, considering Figures 4-7 and 4-8 these locations of maximum mmf disturbance are 2, 4, 6, and 8. It has also been stated that the rotor fault does not have any effect on the rotor mmf orientation at time instants where the broken bar is supposed to carry maximum absolute value of the current, as well as at locations where it is supposed to carry no current. Again, considering Figures 4-7 and 4-8, the locations of bar breakage which will not have any effect on the location of the rotor mmf axis and the machine will appear as if healthy, are locations 1, 3, 5, and 7. This means that at time instants when the breakage reaches locations 1, 3, 5, and 7 the value of the pendulous oscillation angle,  $\delta(t)$ , should correspond/intersect with that of the healthy case.

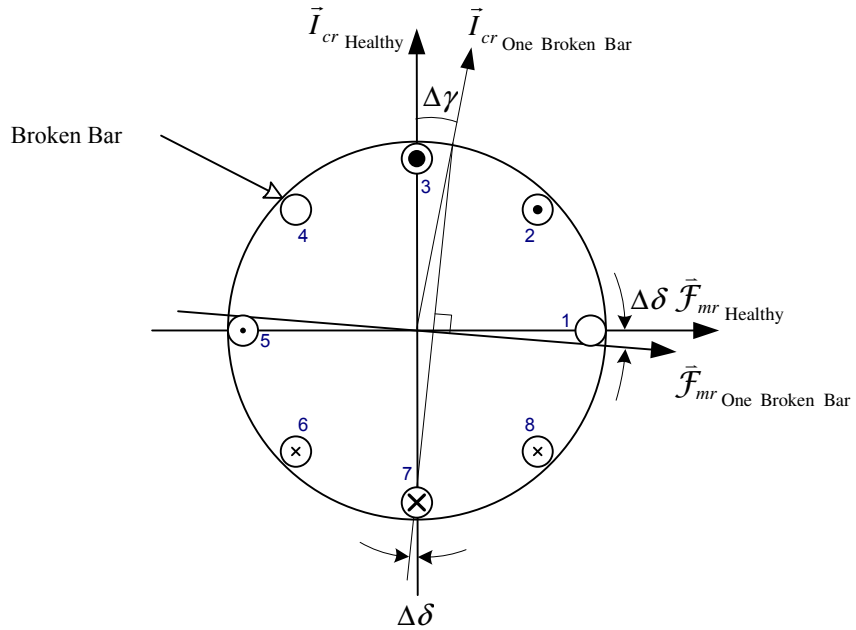


Figure 4-7. Simple 8-bar squirrel-cage rotor (Broken bar at location 4).

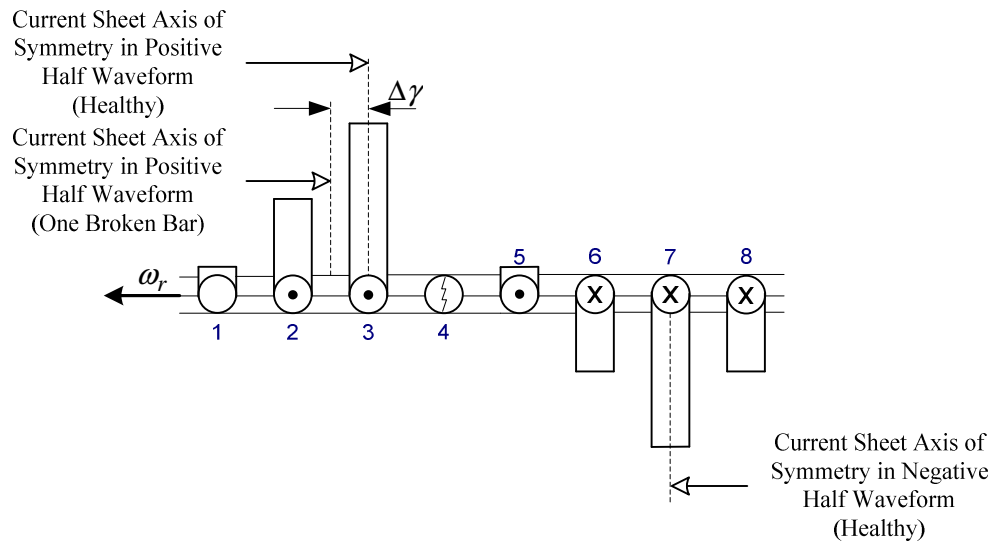
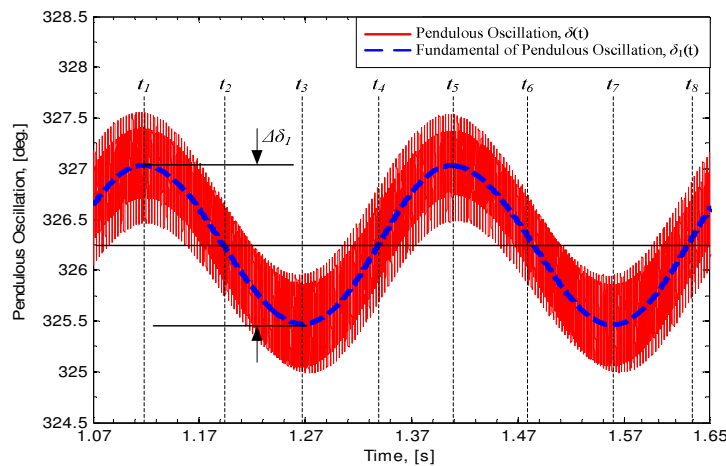


Figure 4-8. Rotor current sheet (Broken bar at location 4).

Now, in order to verify the analysis presented in Chapter 2 consider a time-domain profile of pendulous oscillation angle,  $\delta(t)$ , under the condition of one broken rotor bar obtained from MEC simulation of the 5-hp case study induction machine. This time-domain profile of pendulous oscillation is shown over a complete slip cycle in Figure 4-9. As has been previously mentioned in the case of a one broken bar fault, the pendulous oscillation has a frequency equal to twice the slip frequency,  $2s\omega_{syn}$ . Consequently, as can be observed from Figure 4-9, there are four time instances in a slip cycle where the pendulous oscillation angle reaches its maximum absolute value. Considering Figure 4-9 these time instances are:  $t_1$ ,  $t_3$ ,  $t_5$ , and  $t_7$ . Moreover, there are four time instances in a slip cycle where the bar breakage does not have any effect on the orientation of the rotor mmf. In other words, there are four time instances in a slip cycle where the axis of the faulty rotor mmf aligns with the axis of the healthy mmf. In Figure 4-9 these time instances are labeled as follows:  $t_2$ ,  $t_4$ ,  $t_6$ , and  $t_8$ . In order to verify the analysis presented above consider the current sheet distributions at time instances  $t_1$  through  $t_8$  shown in Figures 4-10 through 4-17. These current sheet distributions are readily available from both the MEC and the TSFE simulations but rather tough to obtain in an experimental setting. Therefore, here in Figures 4-10 through 4-17 only MEC simulation results are presented. Moreover, it should be mentioned that in Figures 4-10 through 4-17 bar number “12” is assumed to be broken.



**Figure 4-9.** Pendulous Oscillation time-domain profile (One broken bar, full-load, MEC Simulation).

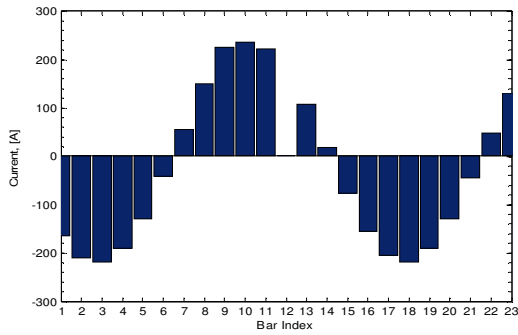


Figure 4-10. Rotor current sheet at time instant  $t_1$ .

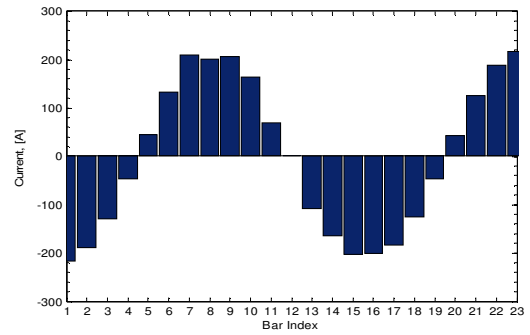


Figure 4-11. Rotor current sheet at time instant  $t_2$ .

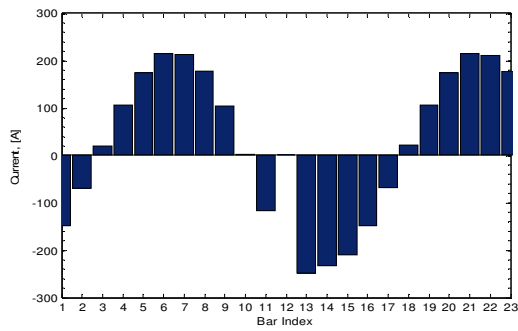


Figure 4-12. Rotor current sheet at time instant  $t_3$ .

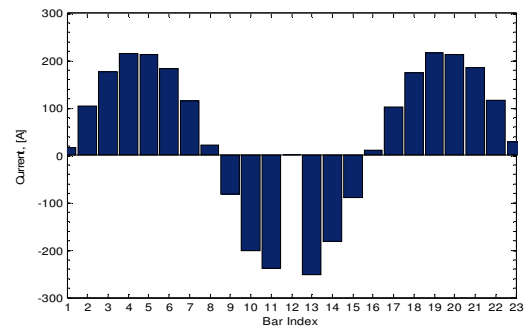


Figure 4-13. Rotor current sheet at time instant  $t_4$ .

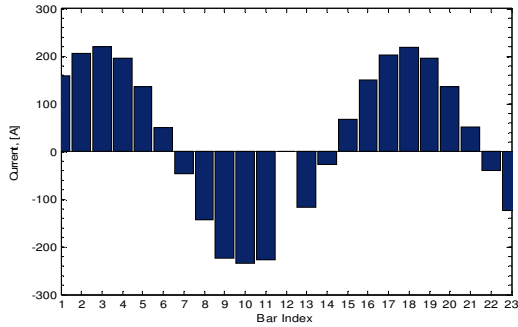


Figure 4-14. Rotor current sheet at time instant  $t_5$ .

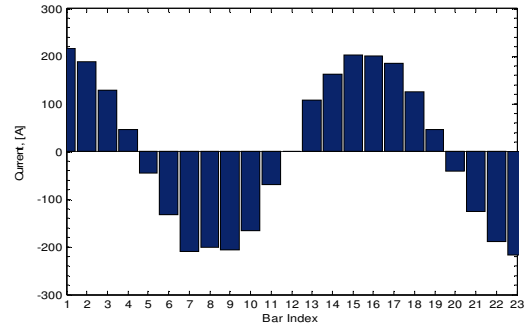


Figure 4-15. Rotor current sheet at time instant  $t_6$ .

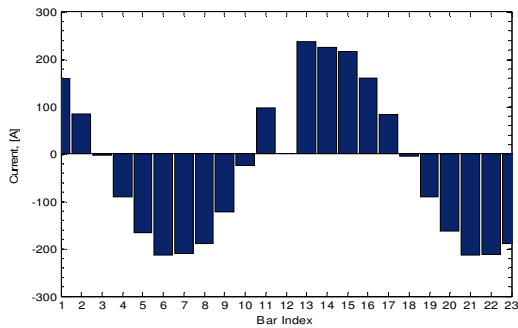


Figure 4-16. Rotor current sheet at time instant  $t_7$ .

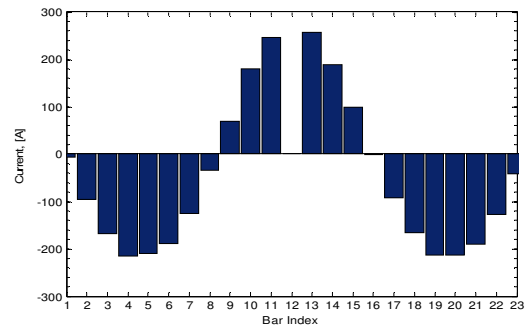
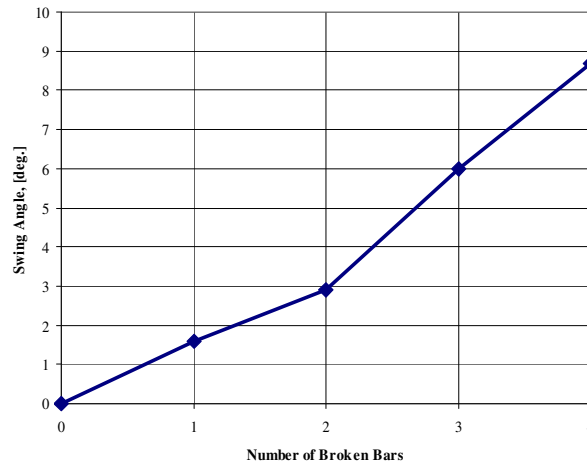


Figure 4-17. Rotor current sheet at time instant  $t_8$ .

As can be seen from the pendulous oscillation profile of Figure 4-9 and the corresponding current sheet profiles shown in Figures 4-10 through 4-17, the simple analysis presented in Chapter 2 is indeed valid and hence can be used to visualize the effects of such rotor faults. In addition, from Figures 4-10 through 4-17 one should notice that magnitudes of bar currents immediately adjacent to the fault are not significantly increased. In this 5-hp machine the increase in bar current magnitudes of the bars immediately adjacent to the fault is approximately 22%, when compared to the healthy bar current magnitudes under the same load conditions.

For purposes of comparison to the MCSA technique and completeness, the effectiveness of the MFPO technique for diagnosing adjacent faults will be explored here. It should be stressed that for detailed discussions of the MFPO technique and its application to adjacent broken rotor bar fault diagnostics one should consult [43-46]. Depicted in Figures 4-18 and 4-19 are the values of swing angles,  $\Delta\delta_l$ , for one through four adjacent broken squirrel-cage rotor bars. As can be seen from both Figures 4-18 and 4-19, the swing angle,  $\Delta\delta_l$ , increases with the number of broken bars in a consistent monotonic fashion, and hence can be used for adjacent broken bar fault diagnostics. Also, from comparison of both figures, one should notice that the MEC model results are in close agreement with results obtained during laboratory testing. This can also be seen from the recorded results in Table 4-2.

In summary, this chapter presented and compared two effective adjacent rotor fault diagnostic techniques. Moreover, models presented in Chapters 2 and 3 have been further verified through analysis of various adjacent rotor fault scenarios. It has also been shown, through simulation and experimental results, that rotor bar breakage faults manifest themselves mainly through the oscillation of the rotor magnetic field, which supports the claim made in the summary of Chapter 2.



**Figure 4-18.** Swing angle,  $\Delta \delta_l$ , versus number of broken bars under full-load conditions (from Experimental Tests).

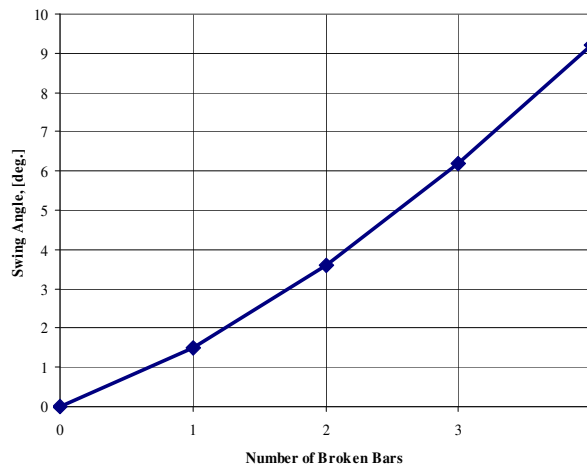


**Figure 4-19.** Swing angle,  $\Delta \delta_l$ , versus number of broken bars under full-load conditions (from MEC Simulations).

Test		MEC	
Number of BB	Swing Angle, [deg.]	Number of BB	Swing Angle, [deg.]
0	0.1	0	0.1
1	1.6	1	1.5
2	2.7	2	3.4
3	4.1	3	6.2
4	8.7	4	9.2

**Table 4-2.** Swing angle,  $\Delta \delta_l$ , under full-load conditions (from Experimental Tests and MEC Simulations).

## CHAPTER 5: APPLICATION OF PIEZOELECTRIC SENSORS TO MOTOR FAULT DIAGNOSTICS

---

### 5.1 INTRODUCTION

**I**N this chapter it will be shown that a simple piezoelectric vibration sensor can be utilized for rotor fault diagnostics. This chapter will present some basic principles behind the application of such piezoelectric sensors to electric machinery. Moreover, the history of application of such sensors to condition monitoring of various industrial processes will be discussed. In addition, some recent applications of piezoelectric sensors to electric machines will be presented.

The piezoelectric effect was first discovered by brothers Jacques and Pierre Curie in 1880s [78]. It has been found that some materials that possess crystal structures are capable of producing electric charge as a result of mechanical deformation. Moreover, it has been shown that dimensions of such materials can be altered when these materials are exposed to electric fields. Both of these properties have found a wide range of applications. The first property of piezoelectric materials allows these materials to be utilized in various sensor applications while the former property allows using such materials for actuation applications. Piezoelectric materials

have been used in vibration sensing for several applications ranging from music pickups and microphones to traffic and bearing wear sensors [78]. Piezoelectric materials have also been utilized in medical imaging ultrasound applications due to their high sensitivity and extremely high bandwidth [78]. Meanwhile, piezoelectric materials have been used in the audio industry for high fidelity speaker and microphone construction [78]. On the other hand, such piezoelectric materials have been used as actuators in fan applications, where the air flow is induced by the oscillating piezoelectric beam/cantilever, which in turn oscillates due to an applied time-varying voltage. In addition, such materials are being utilized for active vibration cancellation applications [78]. Some researchers have also proposed in [79] and [80] using such piezoelectric materials for energy harvesting applications, where the inherent vibration of the system is used to generate electric energy that can latter be utilized to energize low-power electronic devices.

In the above paragraph some general applications of piezoelectric materials have been outlined. Next, recent applications of piezoelectric materials to electric machinery will be considered. In [81] polyvinylidene fluoride (PVDF) film piezoelectric vibration sensors have been successfully used for sensing harmonics of electromagnetic torque in permanent magnet synchronous machines (PMSM). In this work three different locations for sensor mounting have been considered. Meanwhile, the work presented in [81] has been extended to provide an appropriate control action intended to minimize torque ripples in PMSM drives [82]. It has been shown that the feedback signal obtained from a piezoelectric vibration sensor can be utilized to mitigate torque induced vibrations in a close-loop control scheme of a PMSM motor drive system. In addition, PVDF film sensors have been utilized for detection of the initial rotor position in PMSM drives in [83]. More recently, the same group of researchers proposed using PVDF film piezoelectric vibration sensors for speed estimation in induction motor drive systems [84].

## 5.2 POLYVINYLIDENE FLUORIDE (PVDF) PIEZOELECTRIC MATERIAL

As has been mentioned in the introductory chapter of this thesis the suitability of piezoelectric vibration sensors for rotor fault diagnostics purposes will be the main topic of this chapter. More specifically, polyvinylidene fluoride (PVDF) film sensor will be used to obtain a voltage signal proportional to the mechanical vibration of an induction motor. Hence, both mechanical and electrical characteristics of this piezoelectric material need to be addressed. Depicted in Figure 5-1 is a piezoelectric film showing typical mechanical and electrical numerical axes classification [78]. Meanwhile, for all relevant parameters the following subscript notation is used,  $X_{mn}$ , where,  $m$ , refers to the electrical axis and,  $n$ , refers to the mechanical axis. Moreover, since the piezoelectric film used in this thesis has electrodes attached as shown in Figure 5-2 the parameters of interest will have coefficients,  $X_{3n}$ . This is because in this electrode configuration mechanical stress applied in any of the three axes of the film will produce a corresponding measurable voltage in axis-3 [78].

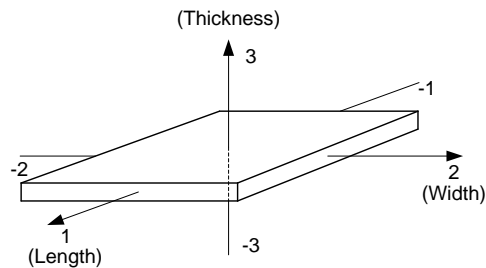


**Figure 5-1.** Piezoelectric (PVDF) film showing mechanical and electrical axes [78].

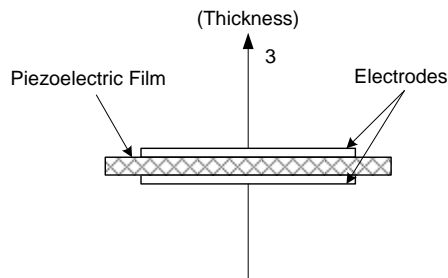


**Figure 5-2.** Piezoelectric (PVDF) film showing electrodes.

From Figure 5-2 one should note that at steady-state conditions this sensor configuration resembles a simple parallel plate capacitor. Hence, its capacitance can be approximated using a simple relationship as follows:

$$C_{PIEZO} = \epsilon_R \epsilon_o \frac{A}{t} \quad (5.1)$$

where,  $\epsilon_R$ , is relative permittivity,  $\epsilon_o$ , is the permittivity of free space,  $A$ , is electrode surface area, and,  $t$ , is the film thickness. It should be mentioned that a typical value of this capacitance for a typical PVDF film sensor is on the order of a few hundred picofarads. As has been previously mentioned under mechanical stresses this piezoelectric material is capable of producing voltage/charge. Hence, one way to model low-frequency behavior of piezoelectric materials is as shown in Figure 5-3. It should be noticed that voltage produced by the voltage source,  $V_{PIEZO}$ , is not directly accessible because of the film capacitance,  $C_{PIEZO}$ . This leads to the fact that only time-varying (dynamic) mechanical stresses can induce voltages across the piezoelectric film electrodes. In other words, the dc component of the voltage produced by the piezoelectric material under constant (time-invariant) stress will be blocked by the material's inherent capacitance,  $C_{PIEZO}$ .

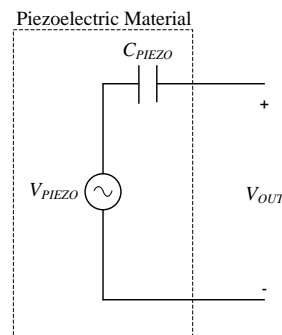


**Figure 5-3.** Electric equivalent circuit model of piezoelectric material.

The bandwidth of the piezoelectric vibration sensor is limited by two factors, namely, the electrical and mechanical loading. Again, considering Figure 5-3 when coupled to a practical electric circuit, which has a finite input impedance, piezoelectric materials will exhibit a high-

pass filter behavior. This means that any frequency below the lower cutoff frequency, dictated by the piezoelectric film capacitance,  $C_{PIEZO}$ , and the input resistance of a signal conditioning, circuit will be attenuated. This can also be seen from Figure 5-4 and the corresponding relationship (5.2), which shows a high-pass filter circuit nature of a piezoelectric sensor when connected to a signal conditioning circuitry.

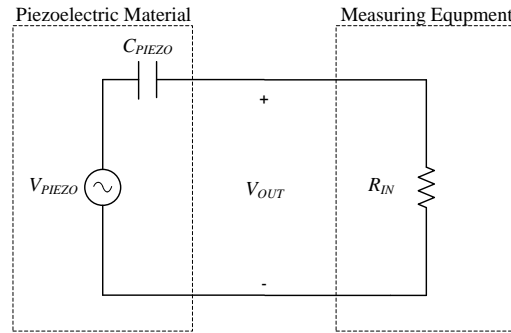


**Figure 5-4.** Electric equivalent circuit model of piezoelectric material connected to a practical circuit.

$$f_{LOW} = \frac{1}{2\pi(C_{PIEZO}R_{IN})} \quad (5.2)$$

Moreover, as has been mentioned earlier typical piezoelectric PVDF film sensors have capacitance values on the order of a few hundred picofarads. Hence, in order to capture low-frequency mechanical vibrations, such as the ones produced by squirrel-cage rotor faults, signal conditioning circuits having extremely high input impedances have to be designed. As has been suggested in [85] JFET operational amplifier circuits can be utilized in the signal conditioning circuit to provide desired high input impedance. A typical (TL-82) JFET operational amplifier has an input impedance on the order of  $10^{12}\Omega$  [86]. Depicted in Figure 5-5 is a typical unity gain buffer (voltage follower) amplifier circuit that can be used to provide high input impedance,  $R_{IN}$ , required for low-frequency sensing applications. From Figure 5-5 one should also notice an additional resistance,  $R_{INaux}$ , that can be used to vary the lower cutoff frequency to values higher than these imposed by,  $C_{PIEZO}$ , and,  $R_{IN}$ .

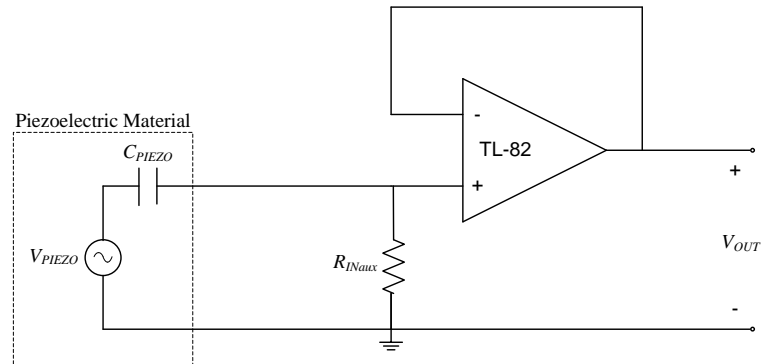


**Figure 5-5.** High input impedance unity gain buffer (voltage follower) amplifier.

On the other hand, linear operation of piezoelectric (PVDF) sensors at high-frequencies is limited by mechanical loading/preload as well as by the mode of operation of the sensor. More specifically, if the film sensor is operated as a vibrating beam/cantilever clamped at one end, as shown in Figure 5-6, its resonant frequency can be significantly reduced by the preload mass. On the other hand, sensitivity of the film sensor to the mechanical vibrations will be increased with the increase of a preload mass. In this mode of operation the mechanical system can be modeled as a simple mass-spring system with a first resonant frequency approximated by the following:

$$f_{resonance} = \frac{1}{2\pi} \sqrt{\frac{k}{m}} \quad (5.3)$$

where,  $k$ , is the stiffness of the piezoelectric film beam and,  $m$ , is the load mass.

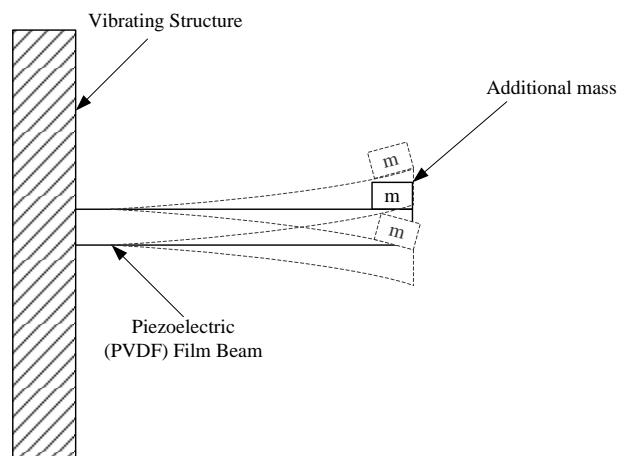


**Figure 5-6.** Piezoelectric PVDF film sensor operated as vibrating beam/cantilever.

In this work, however, the piezoelectric PVDF film is used in a compression mode along axis-3, as shown in Figure 5-7. In this case, the resonant frequency can be significantly increased, hence, increasing the effective bandwidth of the sensor. In this case, the first resonant frequency of a piezoelectric film can be estimated using the following [81]:

$$f_{resonance} = \frac{1}{2t} \sqrt{\frac{Y \left( 1 + \frac{F_{LOAD}}{YA} \right)}{\rho}} \tag{5.4}$$

where,  $t$ , is PVDF film thickness,  $Y$ , is material Young’s modulus,  $A$ , is the surface area of the film while,  $\rho$ , is PVDF material density and,  $F_{LOAD}$ , is the static preload force due to the mass of the vibrating structure.

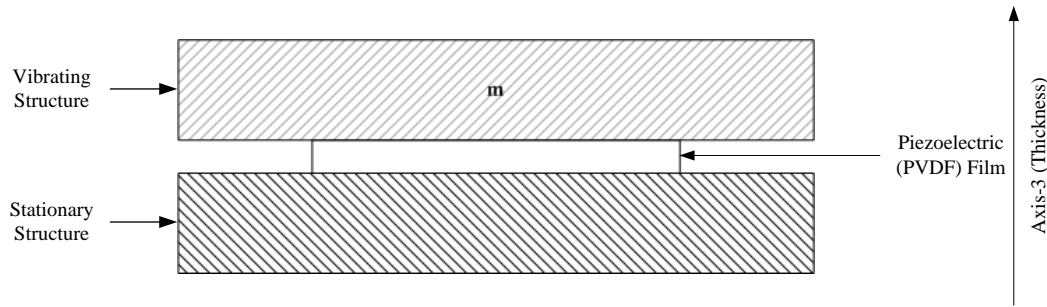


Figure 5-7. Piezoelectric PVDF film sensor operated in compression mode along axis-3.

It should be noted that the compression mode along axis-3 is chosen because of its simplicity and repeatability of experimental test results.

In this work a simple piezoelectric PVDF film sensor (part no. LDT0-028K/L) commercially manufactured by Measurement Specialties has been used. Shown in Table 5-1 are the relevant parameters of this PVDF film sensor [78], [87].

Thickness, $t$ , [ $\mu m$ ]	Width, $w$ , [ $mm$ ]	Length, $l$ , [ $mm$ ]	Piezo Stress Constant, $g_{33}$ , $\left[ \frac{V/m}{N/m^2} \right]$	Capacitance, $C_{PIEZO}$ , [ $pF$ ]	Young’s Modulus, $Y$ , [ $N/m^2$ ]	Relative Permittivity, $\epsilon_R$	Mass Density, $\rho$ , [ $kg/m^3$ ]	Temperature Range, [ $^{\circ}C$ ]
28	10.2	23.5	$330 \times 10^{-3}$	500	$2-4 \times 10^9$	12-13	$1.78 \times 10^3$	-40 to 100

Table 5-1. Piezoelectric PVDF sensor parameters.

The voltage produced by PVDF sensor as a result of mechanical stresses along axis-3 can be approximated as follows [78]:

$$V_{OUT} = g_{33} \left( \frac{F_3}{A} \right) t \quad (5.5)$$

where,  $F_3$ , is the force applied to the sensor along axis-3.

### 5.3 MOTOR FAULT DIAGNOSTICS USING PIEZOELECTRIC VIBRATION SENSOR

In this section, the application of the PVDF film sensor to motor fault diagnostics will be considered. It will be shown that the torque ripple produced as the result of the fault in the squirrel-cage rotor can be detected using a simple piezoelectric vibration sensor. Moreover, since this vibration signal also carries information about the speed of the machine the diagnostics procedure can be significantly simplified since it will provide the information about the slip frequency. Depicted in Figure 5-8 is the experimental setup showing the location of the piezoelectric PVDF film sensor. From Figure 5-8 one should note that the vibration sensor is mounted between the frame of the induction machine and the mounting base which is used to secure the machine. As has been mentioned in the previous section, this results in the sensor being preloaded by the static force due to the machine's weight and the force exerted by the mounting bolts. An alternative mounting, which could prove to be more reliable and convenient from the installation and repeatability point of view, could be a piezoelectric sensor in the form of a washer that could be used instead of an original mounting washer. However, this may require using an alternative ceramic material which in general has a lower sensitivity i.e. it produces a lower voltage for the same stress applied.

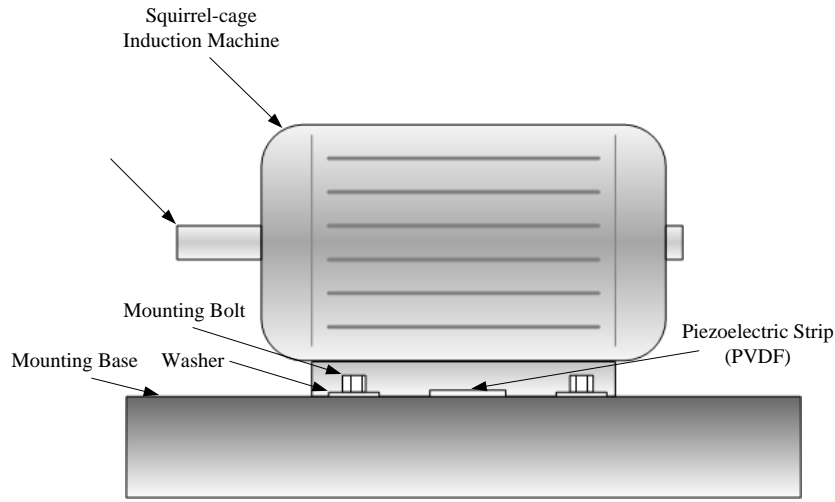


**Figure 5-8.** Experimental setup showing the location of PVDF sensor.

Now, that both the sensor and the experimental setup have been described the results obtained during the experimental tests can be presented. Shown in Figure 5-9 is a time-domain profile of the voltage signal obtained for a healthy machine operating at rated conditions. One should note a distinct fundamental component. As has been pointed out in [84], this fundamental component can be used for speed estimation purposes. As for the causes of this fundamental component, it may be caused by a number of imperfections ranging from magnetic circuit saliencies traveling at slip speed, and shaft misalignment, to unbalances of mass distribution in the rotating parts of the machine. In one form or another, these imperfections caused by manufacturing tolerances and the nature of magnetic materials used in construction of the magnetic core are present in every machine. Depicted in Figure 5-10 is the frequency spectrum of the same vibration signal showing the locations of a fundamental component at  $19.4\text{Hz}$ . Moreover, shown in Figure 5-10 is a frequency component at twice the slip frequency,  $2sf$ , which will be used to diagnose the machine. Meanwhile, the mechanical speed can be estimated from the fundamental frequency using the following:

$$n_{mech} = \frac{120 \left( \frac{P}{2} f_1 \right)}{P} = 60 f_1 \quad (5.6)$$

where,  $P$ , is the number of poles and,  $f_l$ , is the fundamental frequency of vibration signal.

Shown in Figures 5-11 and 5-12 are the corresponding time-domain and frequency spectrum of the vibration signal of a machine operating with one broken bar at full-load conditions. From 5-13 one should note a corresponding increase of the frequency component at  $2sf$ . Moreover, one should also note two side-band components adjacent to the fundamental frequency component.

These side-bands result from the speed ripple produced as a result of torque oscillations.

Mathematically this situation can be described as shown next. At steady-state conditions the developed torque can be expressed as a sum of a constant (dc) value and an additional ripple at frequency of  $2sf$  as shown in (5.7). It should be mentioned that the second term on the right hand side of equation (5.7) is responsible for detectable motor vibrations and results in a  $2sf$  frequency component with a normalized magnitude of  $-29.49dB$  in the spectrum of a vibration signal under conditions of one broken bar.

$$T_{dev} = T_{const} + A_{ripple} \cos(2\pi(2sf) t) \quad (5.7)$$

Using (5.7) the mechanical speed can be expressed as follows:

$$\omega_m = \frac{1}{J} \int (T_{dev} - T_{load}) dt = \omega_{const} + \frac{1}{J} \left( (T_{const} - T_{load}) t + \frac{A_{ripple}}{2\pi(2sf)} \sin(2\pi(2sf) t) \right) \quad (5.8)$$

where,  $J$ , is motor-load system total inertia,  $T_{load}$ , is the load torque and,  $A_{ripple}$ , is the torque ripple amplitude produced by the rotor fault. From (5.8) one should observe that in the case when developed torque,  $T_{const}$ , is equal to the load torque,  $T_{load}$ , the average (dc) value of the speed is constant, and hence, equation (5.8) can be rewritten as shown in (5.9).

$$\omega_m = \omega_{const} + \frac{1}{2\pi(2sf)} \left( \frac{A_{ripple}}{J} \right) \sin(2\pi(2sf) t) \quad (5.9)$$

However, in the case of a vibration sensor being mounted as is shown in Figure 5-8 the speed is not measured directly at the shaft but rather its effect on the vibration sensor is observed through

the forces/stresses applied to the sensor. Hence, with respect to the stationary frame of reference any imperfections that move in space as described by (5.9) will result in the forces/stresses on the sensor which will have the following components:

$$F_{speed} = \alpha \cos\left(2\pi\left(\frac{2}{P}\right)(f - sf) t\right) + \beta\left(\frac{1}{2\pi(2sf)}\right)\left(\frac{A_{ripple}}{J}\right)\sin(2\pi(2sf)t)\cos\left(2\pi\left(\frac{2}{P}\right)(f - sf) t\right) \quad (5.10)$$

where,  $\alpha$ , and,  $\beta$ , are appropriate conversion factors. Equation (5.10) can be simplified as shown in (5.11).

$$F_{speed} = \alpha \cos\left(2\pi\left(\frac{2}{P}\right)(f - sf) t\right) + \beta\left(\frac{1}{2\pi(2sf)}\right)\left(\frac{A_{ripple}}{J}\right)\left(\frac{1}{2}\sin\left(2\pi\left(\frac{2}{P}\right)(f - sf) + 2sf\right) t\right) - \frac{1}{2}\sin\left(2\pi\left(\frac{2}{P}\right)(f - sf) - 2sf\right) t\right) \quad (5.11)$$

One should note that first term on the right hand side of equation (5.11) results in the fundamental component of the vibration signal shown in Figures 5-10 and 5-12. Meanwhile, the second term is specific to the rotor fault case and produces the side-bands shown in Figure 5-12. From equation (5.11) one should also notice that magnitudes of side-bands tend to diminish with an increase in both slip frequency and motor-load inertia. From the discussion presented above one can conclude that in the case of adjacent rotor broken bar faults, the total force/stress applied to the vibration sensor along axis-3 will have components such as the ones described in (5.12). Considering equation (5.12) and Figure 5-12 one should observe a direct correlation between the corresponding frequency components.

$$\begin{aligned}
 F_3 = F_{torque} + F_{speed} = & \underbrace{\gamma A_{ripple} \cos(2\pi(2sf) t)}_{\substack{2sf \text{ component} \\ \text{(Torque Ripple)}}} + \underbrace{\alpha \cos\left(2\pi\left(\frac{2}{P}\right)(f - sf) t\right)}_{\substack{\text{Fundamental component} \\ \text{(Average Speed)}}} \\
 & + \beta \left(\frac{1}{2\pi(2sf)}\right) \left(\frac{A_{ripple}}{J}\right) \left( \underbrace{\frac{1}{2} \sin\left(2\pi\left(\frac{2}{P}\right)(f - sf) + 2sf\right) t}_{\substack{\text{Upper side-band} \\ \text{(Speed Ripple)}}} - \frac{1}{2} \sin\left(2\pi\left(\frac{2}{P}\right)(f - sf) - 2sf\right) t \right) \right)
 \end{aligned} \tag{5.12}$$

It should be mentioned that in equation (5.12) the conversion factors,  $\gamma$ ,  $\alpha$ , and,  $\beta$ , are used to emphasize the physical conversion from torque and speed to force/stress in the direction of axis-3. Moreover, right hand side terms of (5.12) may have phase shifts other than the ones shown. Hence, the main purpose of (5.12) is to relate the physical phenomena of torque and speed ripple to the frequency spectrum of the vibration signal.

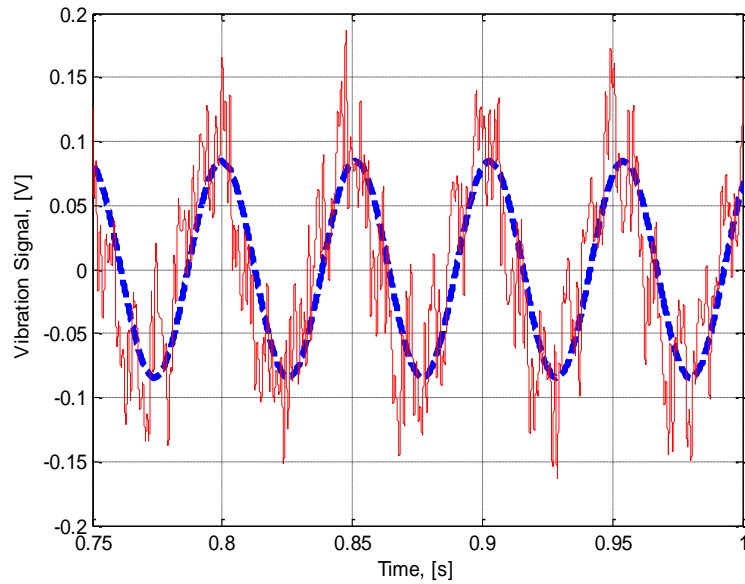


**Figure 5-9.** Vibration signal of 5-hp induction machine under healthy full-load conditions (30Nm, 1164r/min, from Experimental Test).

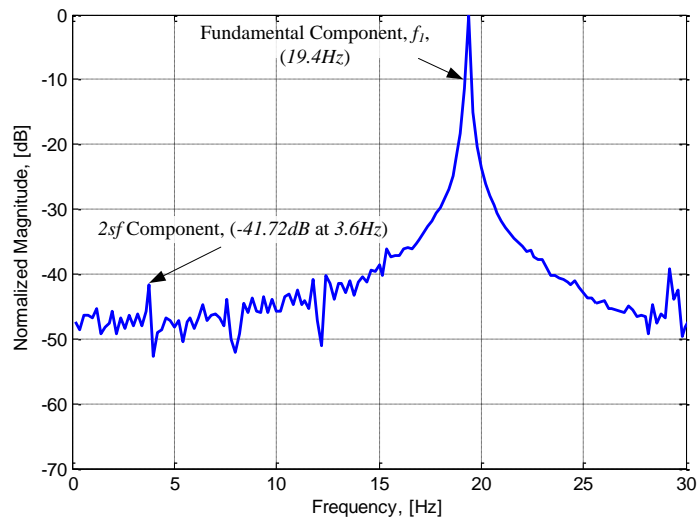


**Figure 5-10.** Spectrum of vibration signal of 5-hp induction machine under healthy full-load conditions (30Nm, 1164r/min, from Experimental Test).

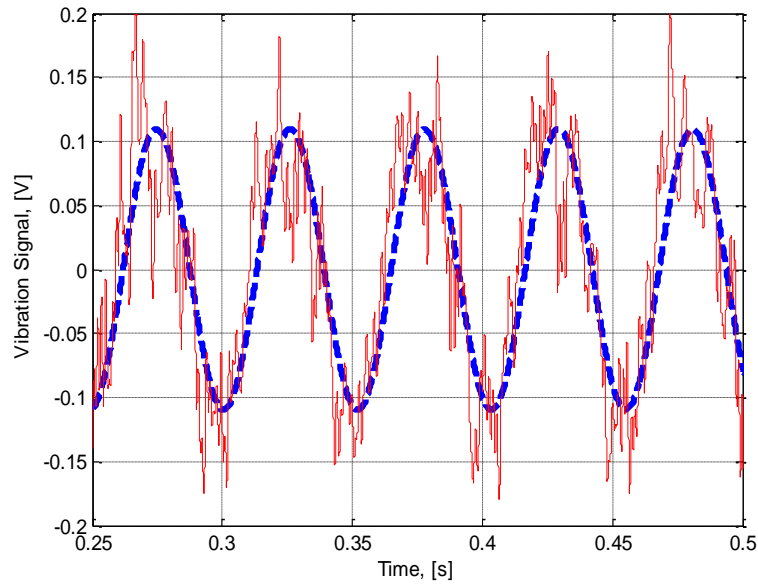


**Figure 5-11.** Vibration signal of 5-hp induction machine under one broken bar full-load conditions (30Nm, 1164r/min, from Experimental Test).

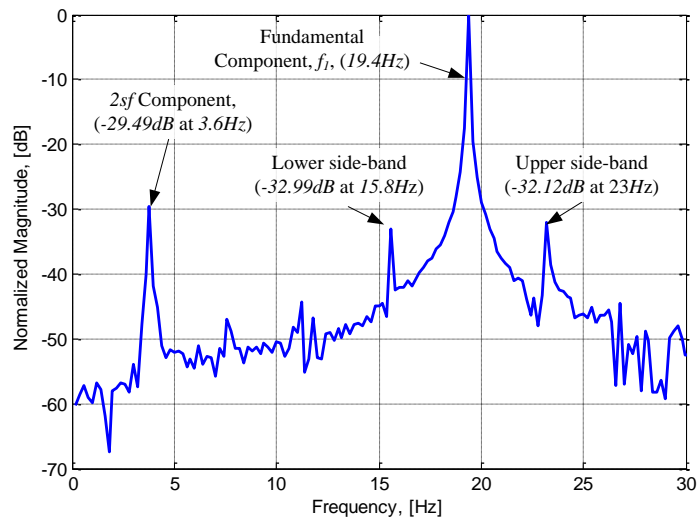


**Figure 5-12.** Spectrum of vibration signal of 5-hp induction machine under one broken bar full-load conditions (30Nm, 1164r/min, from Experimental Test).

In order to verify that the proposed vibration sensor is capable of detecting an increase in the number of adjacent broken bars an additional test has been performed. More specifically, PVDF vibration sensor was used to diagnose a case study 5-hp machine with four adjacent rotor bar breakages. The results of this experimental test are depicted in Figure 5-13. Comparing Figures 5-12 and 5-13 one should notice a significant increase of a  $2sf$  component and the consequent increase of both side-band components. This leads the author to conclude that such piezoelectric vibration sensors can be utilized for rotor fault diagnostics. Moreover, since the rotor speed and hence the slip frequency are readily available from the signal used for diagnostics purposes the overall diagnostics procedure is significantly simplified.

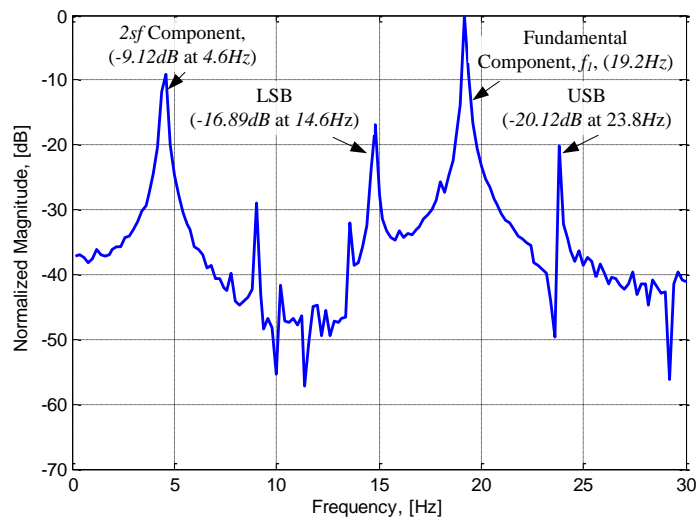


**Figure 5-13.** Spectrum of vibration signal of 5-hp induction machine under four broken bar full-load conditions (30Nm, 1155r/min, from Experimental Test).

## CHAPTER 6: EXPERIMENTAL AND SIMULATION RESULTS

---

### 6.1 INTRODUCTION

**I**N this chapter experimental and simulation results for a number of nonadjacent bar breakage scenarios will be considered. In the first section of this chapter experimental and simulation results for nonadjacent bar breakages separated by one half pole-pitch will be considered. Meanwhile, in the second part of this chapter rotor faults separated by one complete pole-pitch will be studied. As has been mentioned in Chapter 2, in this work pole-pitch measure is considered to be a number of rotor bars per pole. For the case study 5-hp machine used in this thesis this number is fractional and is equal to  $7\frac{1}{2}$  bars per pole. It should also be mentioned that both simulation and experimental results presented in this chapter are obtained at rated operating conditions with the machine supplied by a balanced three-phase sinusoidal voltage supply. For this case study 5-hp machine rated conditions correspond to torque of  $30Nm$  at the shaft speed of  $1165r/min$ .

### 6.2 ROTOR BAR BREAKAGES SEPARATED BY HALF POLE-PITCH

Here, experimental results of the machine operating under conditions of broken bars, separated by a half pole-pitch ( $90^\circ$  electrical) will be presented. The results will be evaluated

using the three diagnostic techniques described in the previous chapters. Namely, these techniques are the MCSA, MFPO, and piezoelectric vibration sensor technique. Two fault scenarios will be considered, namely, two broken bars separated by one half pole-pitch and  $N$  broken bars each separated by one half pole-pitch from the other, where  $N$  is an integer.

### 6.2.1 TWO BROKEN BARS SEPARATED BY HALF POLE-PITCH

As has been previously shown in Chapter 2 such faults are difficult to diagnose because of the fault masking that takes place when two bars are separated by one half pole-pitch ( $90^\circ$  electrical). However, as will be shown in this section these nonadjacent faults can still be diagnosed using secondary saturation effects that appear under such fault conditions.

Shown in Figure 6-1 is the cross-section of the case study machine showing the locations of nonadjacent rotor bar breakages separated by approximately one half pole-pitch ( $90^\circ$  electrical).

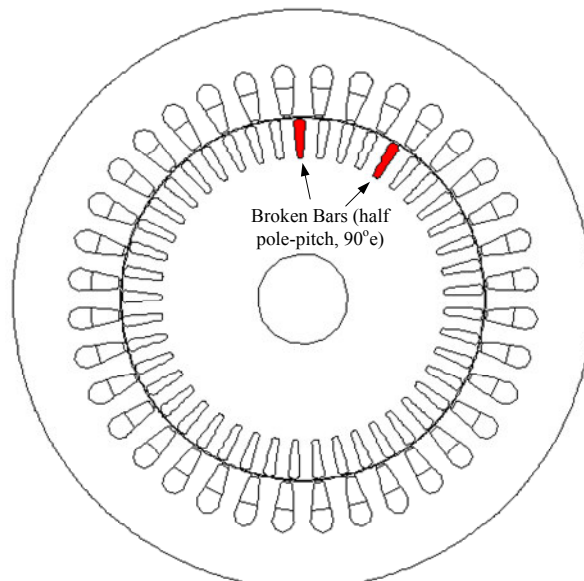


**Figure 6-1.** Cross-section of a case study 5-hp squirrel-cage induction machine showing locations of nonadjacent bar breakages separated by half pole-pitch,  $90^\circ$ e.

Depicted in Figure 6-2 are experimental results evaluated using MCSA diagnostic technique. Also, for the purposes of comparison shown in Figures 6-3 and 6-4 are the results for healthy and two adjacent bar breakage cases. From comparison of Figures 6-2 through 6-4, one should notice that both lower side-band (LSB) and upper side-band (USB) components at frequencies equal to  $(I \pm 2s)f$  are significantly reduced in the case of the nonadjacent fault. Hence, when the original MCSA approach is used to diagnose this type of fault chances of successful diagnosis of the machine under such nonadjacent bar breakage are significantly reduced. Moreover, upon careful examination of Figures 6-2 and 6-3 one should notice that in the case of the nonadjacent fault the lower side-band component at frequency equal to  $(I - 2s)f$ , which is generally used as the primary fault index in the MCSA approach, corresponds to the LSB of the healthy machine.

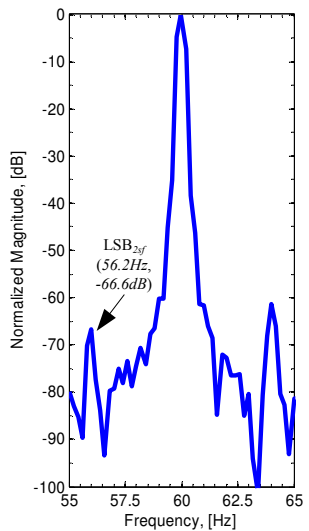


**Figure 6-2.** Current frequency spectrum (MCSA) under conditions of two broken bars separated by half pole-pitch, 90° electrical (from Experimental Test).

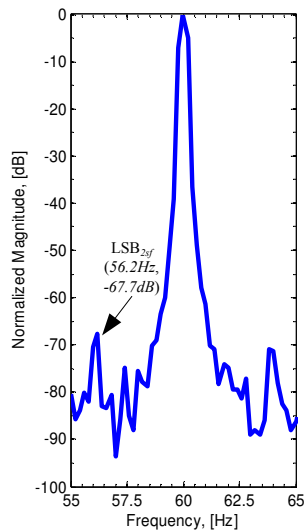


**Figure 6-3.** Current frequency spectrum (MCSA) under healthy conditions (from Experimental Test).

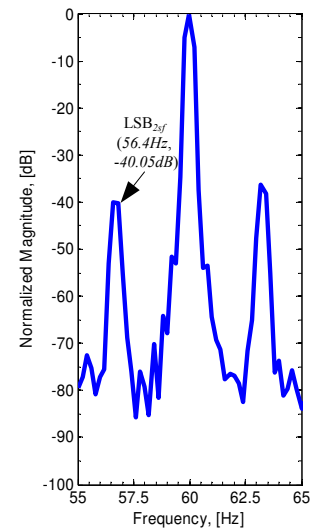


**Figure 6-4.** Current frequency spectrum (MCSA) under conditions of two adjacent broken bars (from Experimental Test).

In Figures 6-5 through 6-7 the same experimental results are evaluated using the MFPO diagnostic technique. In these figures the time-domain profiles of pendulous oscillation are plotted over a time period equal to approximately one slip cycle,  $1/sf$ . Again, similar to results obtained using original MCSA approach, in the case of a nonadjacent rotor fault, the swing angle fault index,  $\Delta\delta_f$ , is significantly reduced. One should also notice that the frequency of the pendulous oscillation doubles in the case of the nonadjacent rotor fault.

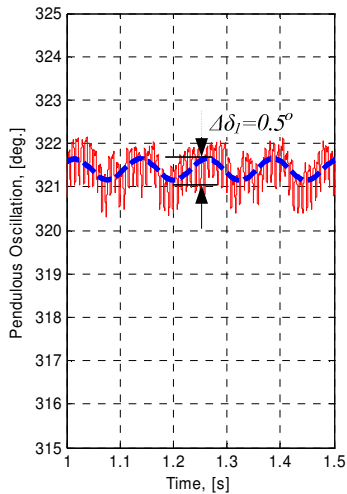


**Figure 6-5.** Pendulous Oscillation time-domain profile (MFPO) under conditions of two broken bars half pole-pitch, 90° electrical (from Experimental Test).

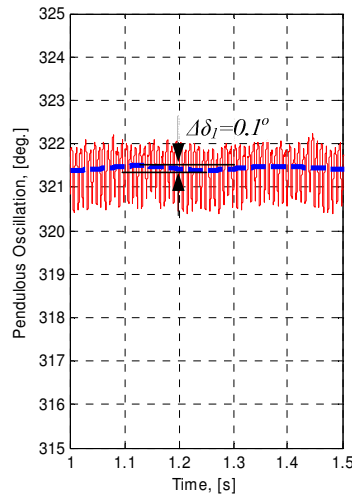


**Figure 6-6.** Pendulous Oscillation time-domain profile (MFPO) under healthy conditions (from Experimental Test).

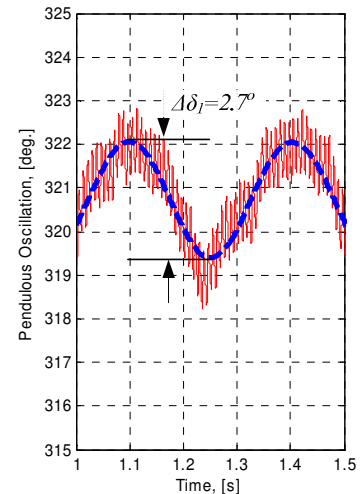


**Figure 6-7.** Pendulous Oscillation time-domain profile (MFPO) under conditions of two adjacent broken bars (from Experimental Test).

Consequently, referring back to the frequency spectrum of the MCSA approach in the case of nonadjacent rotor bar breakage fault one should expect detectable side-bands at frequencies equal to  $(1 \pm 4s)f$ . These side-band components are shown in Figure 6-8. Moreover, one should also notice the lack of these components in the frequency spectra of the healthy machine, Figure 6-9, and the machine with two adjacent bar breakages, Figure 6-10. This alludes to the fact that in the case when the classic LSB component at  $(1-2s)f$  is not present one could use LSB component at  $(1-4s)f$  to detect such nonadjacent faults. It should be mentioned that in the case of adjacent bar

breakage faults side-band components at  $(1\pm 2s)f$  may result in other side-band components including side-bands at  $(1\pm 4s)f$ . However, in the case of nonadjacent rotor faults separated by one half pole-pitch the  $(1\pm 4s)f$  components appear due to secondary local rotor saturation effects adjacent to the location of these breakages.

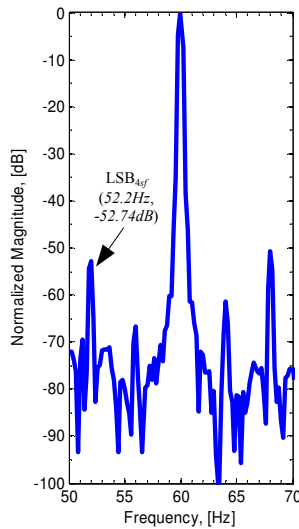


**Figure 6-8.** Current frequency spectrum (MCSA) two broken bars separated by half pole-pitch,  $90^\circ$  electrical (from Experimental Test).

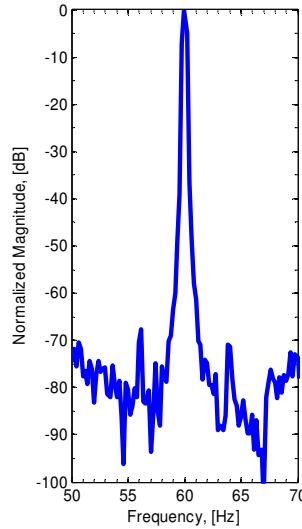


**Figure 6-9.** Current frequency spectrum (MCSA) under healthy conditions (from Experimental Test).

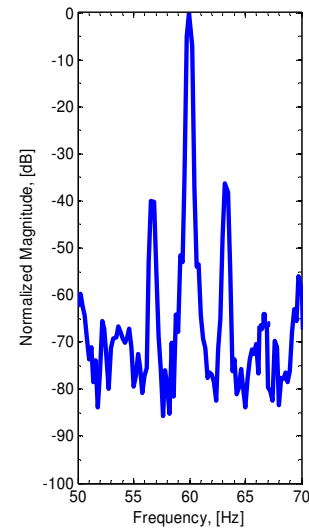


**Figure 6-10.** Current frequency spectrum (MCSA) under conditions of two adjacent broken bars (from Experimental Test).

Now the results of rotor bar breakage diagnostics using the piezoelectric vibration method will be presented. Depicted in Figures 6-11 through 6-13 are the frequency spectra of vibration signals for the cases of the squirrel-cage rotor with two bar breakages separated by one half pole-pitch, the case with a healthy rotor, and the case of a rotor with one broken bar. Comparing Figures 6-11 and 6-13, one should notice a significant magnitude decrease of the frequency component at  $2sf$  in the case of two bar breakages separated by a half pole-pitch. Moreover, from Figure 6-11 one should notice a distinct frequency component at  $4sf$ , which can be used for diagnostics of such faults.

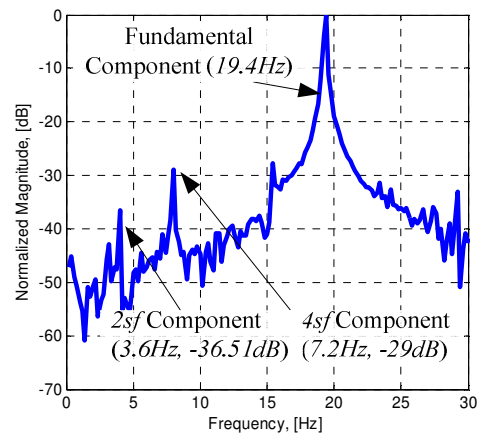


**Figure 6-11.** Spectrum of vibration signal of 5-hp induction machine under conditions of two broken bars separated by half pole-pitch, 90° electrical (from Experimental Test).

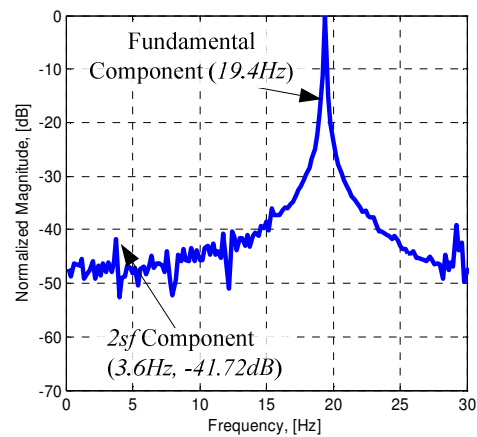


**Figure 6-12.** Spectrum of vibration signal of 5-hp induction machine under healthy conditions (from Experimental Test).

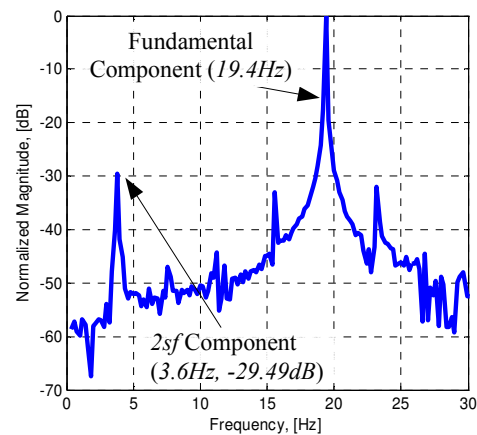


**Figure 6-13.** Spectrum of vibration signal of 5-hp induction machine under one broken bar conditions (from Experimental Test).

As has been previously mentioned in this section, in the case of two bar breakages separated by one half pole-pitch, secondary saturation effects can be used for rotor fault diagnostics. In the case of a broken rotor bar, the rotor teeth immediately adjacent to the broken bar are subjected to higher flux densities which in turn locally affect the magnetic core permeability in these teeth. This results in the local saturation patterns that appear twice every slip cycle. Moreover, in the case of two nonadjacent bar breakages this will result in saturation patterns appearing four times during one slip cycle. Consequently, these patterns modulate the stator currents and/or produce torque pulsations, which in turn may result in consequent speed oscillation, and hence lead to subtle but detectable fault indices.

### 6.2.2 $N$ BROKEN BARS SEPARATED BY HALF POLE-PITCH

In the previous section it has been shown that two broken bars separated by one half pole-pitch,  $N=2$ , result in significant reduction of conventional fault indices. Moreover, from the analysis presented in the previous section one can safely conclude that in cases when  $N$  is equal to an even number, fault masking will take place. Here, effects of an odd number of broken bars, each separated by half pole-pitch, on rotor fault diagnostics will be studied. More precisely, three bars separated by half pole-pitch,  $N=3$ , will be considered. This situation is shown in Figure 6-14.

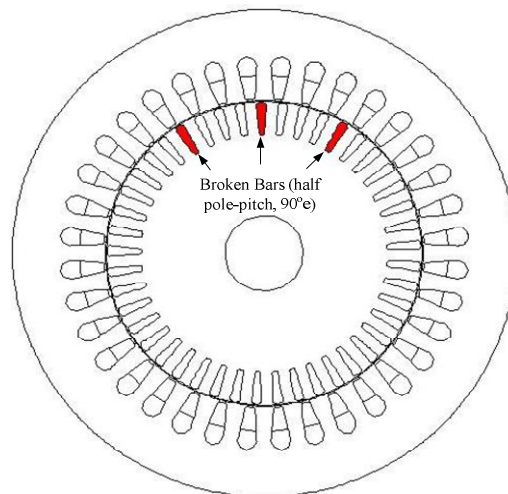


**Figure 6-14.** Cross-section of a case study 5-hp squirrel-cage induction machine showing locations of nonadjacent bar breakages separated by half pole-pitch ( $90^\circ\text{e}$ )  $N=3$ .

Shown in Figure 6-15 are experimental results evaluated using MCSA diagnostic technique in the case when the squirrel-cage rotor has three bar breakages each separated by one half pole-pitch,  $N=3$ . For comparison purposes, Figure 6-16 depicts experimental results in the case when squirrel-cage rotor has only one broken bar. Considering Figures 6-15 and 6-16 one should notice that in both cases the lower side-band components at  $(1-2s)f$  are very close in value. More specifically, in the case of three bars each separated by half pole-pitch  $|LSB_{2sf}| = -44.27dB$ , whereas in the case of one broken bar  $|LSB_{2sf}| = -44.7dB$ . Also, in the case of three broken bars each separated by one half pole-pitch one should notice a set of distinct side-band components at  $(1\pm 4s)f$ , which hint at the possibility of presence of additional nonadjacent faults.

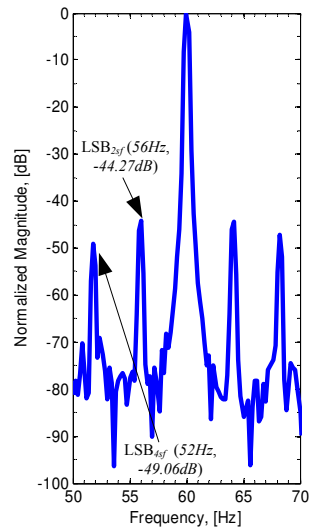


**Figure 6-15.** Current frequency spectrum (MCSA) under conditions of three broken bars separated by half pole-pitch,  $90^\circ$  electrical,  $N=3$ , (from Experimental Test).

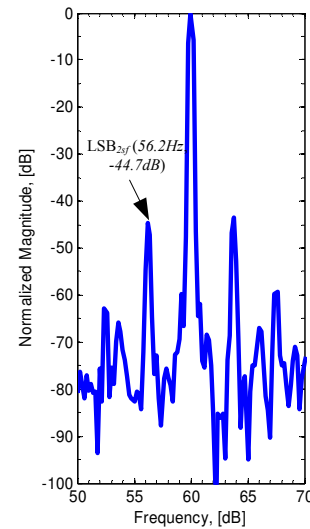


**Figure 6-16.** Current frequency spectrum (MCSA) under conditions of one broken bar (from Experimental Test).

Same experimental results have been processed using MFPO diagnostic technique. The corresponding time-domain profiles of the pendulous oscillation are plotted in Figure 6-17 and 6-18. One should note that in both cases the values of the swing angles are in close agreement. This

means that in the case of three bar breakages,  $N=3$ , separated by one half pole-pitch both diagnostic techniques yield fault indices corresponding to one broken bar.

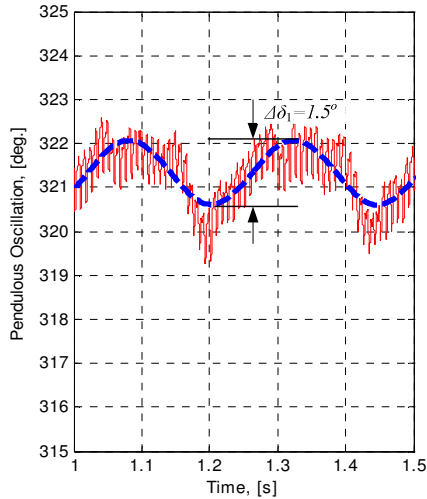


**Figure 6-17.** MFPO under conditions of three broken bars half pole-pitch,  $90^\circ$  electrical,  $N=3$ , (from Experimental Test).

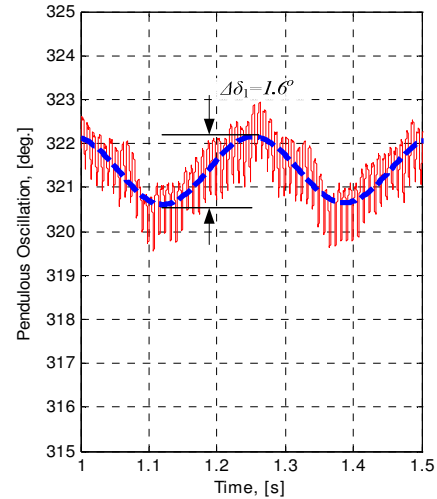


**Figure 6-18.** MFPO under conditions of one broken bar (from Experimental Test).

Depicted in Figures 6-19 and 6-20 are the frequency spectra of vibration signals obtained for the cases of three broken bars separated by a half pole-pitch and the one broken rotor bar. One should notice that in both cases magnitudes of frequency components at  $2sf$  are in close agreement. Meanwhile, a distinct  $4sf$  component is present only in the case of three bar breakages separated by one half pole-pitch.

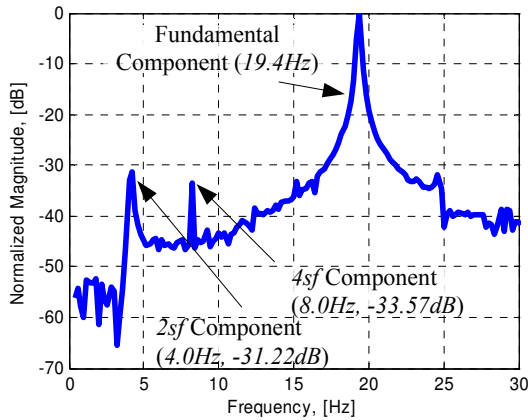


**Figure 6-19.** Spectrum of vibration signal of 5-hp induction machine under conditions of three broken bars separated by half pole-pitch,  $90^\circ$  electrical,  $N=3$ , (from Experimental Test).

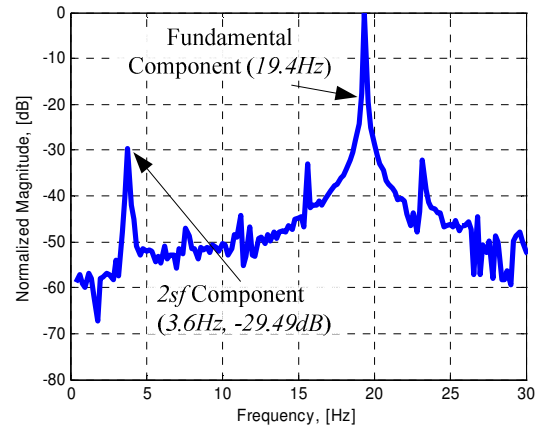


**Figure 6-20.** Spectrum of vibration signal of 5-hp induction machine under one broken bar conditions (from Experimental Test).

From analysis presented above one should notice that in the case of an odd number of nonadjacent bar breakages each separated by one half pole-pitch conventional fault diagnostic indices, such as  $LSB_{2sf}$  and/or swing angle,  $\Delta\delta_1$ , yield values equivalent to one broken rotor bar. In other words, squirrel-cage rotors subjected to such faults can be easily misdiagnosed as having one bar breakage. From the above presented results, one can safely conclude that in the case of  $N$  equal to an odd number (3, 5, 7, ...) fault indices corresponding to one rotor bar breakage will be produced.

### 6.3 ROTOR BAR BREAKAGES SEPARATED BY ONE POLE-PITCH

In this section simulation and experimental results for broken bars, separated by one pole-pitch ( $180^\circ$  electrical) will be presented. Again, simulation and experimental results will be evaluated using the three diagnostic techniques described in the previous chapters. Similar to the previous section, two fault scenarios will be considered, namely, two broken bars separated by one pole-pitch and  $N$  broken bars separated by one pole-pitch.

### 6.3.1 TWO BROKEN BARS SEPARATED BY ONE POLE-PITCH

Shown in Figure 6-21 is the cross-section of the case study 5-hp squirrel-cage induction machine showing the locations of nonadjacent bar breakages.

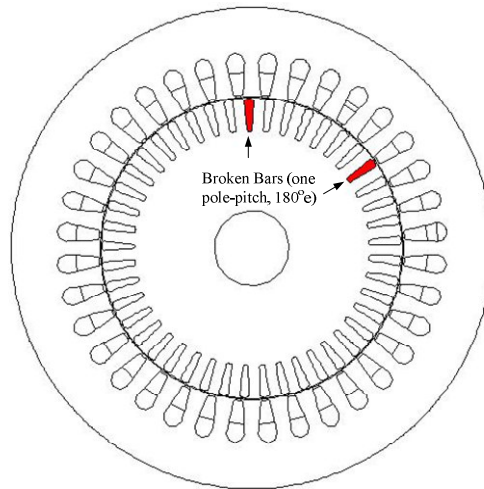


**Figure 6-21.** Cross-section of a case study 5-hp squirrel-cage induction machine showing locations of nonadjacent bar breakages separated by one pole-pitch ( $180^\circ$ )  $N=3$ .

Depicted in Figure 6-22 are the experimental results obtained for the case of two broken bars separated by one pole-pitch evaluated using the MCSA diagnostic technique. Also, for comparison purposes results for two adjacent bar breakages are plotted in Figure 6-23.

Comparing Figures 6-22 and 6-23 one should notice that magnitudes of the lower side-band components at  $(1-2s)f$  are in close agreement. More specifically, in the case of two bars separated by one pole pitch  $|LSB_{2sf}| = -38.0dB$ , which is in close agreement with the value obtained for the two adjacent bar fault  $|LSB_{2sf}| = -40.05dB$ .

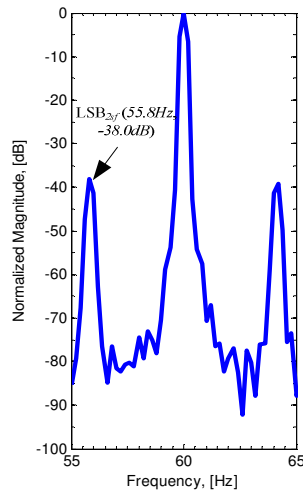


**Figure 6-22.** Current frequency spectrum (MCSA) under conditions of two broken bars separated by one pole-pitch, 180° electrical (from Experimental Test).

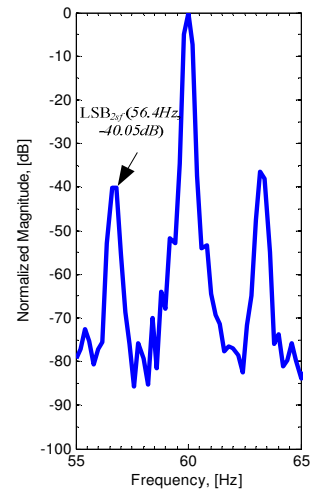


**Figure 6-23.** Current frequency spectrum (MCSA) under conditions of two adjacent broken bars (from Experimental Test).

Results obtained using MCSA diagnostic technique have been verified using the MFPO approach. Depicted in Figures 6-24 and 6-25 are the pendulous oscillation time-domain profiles corresponding to the two fault scenarios. Again, one should notice a very close agreement between the swing angle values. This indicates that such nonadjacent faults yield fault indices ( $LSB_{2sf} \Delta\delta_1$ ) corresponding to the adjacent faults with the same number of bar breakages.

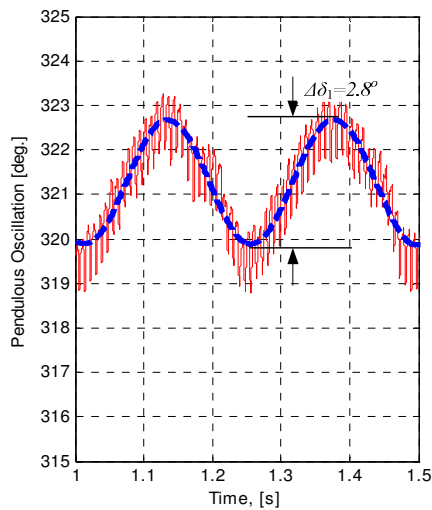


**Figure 6-24.** MFPO under conditions of three broken bars one pole-pitch, 180° electrical (from Experimental Test).

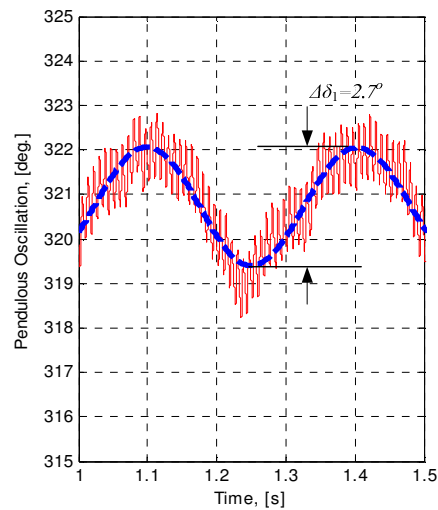


**Figure 6-25.** MFPO under conditions of two adjacent broken bars (from Experimental Test).

### 6.3.2 $N$ BROKEN BARS SEPARATED BY ONE POLE-PITCH

In the previous section it has been shown that in the case of two nonadjacent rotor bar breakage faults separated by one pole-pitch ( $180^\circ$  electrical) the fault indices ( $LSB_{2sf}$ ,  $\Delta\delta_l$ ) corresponding to two adjacent bar breakages will be produced. In this section these results will be extended to show that in cases when  $N$  nonadjacent bar breakages are separated by one pole-pitch fault indices corresponding to  $N$  adjacent bar breakages will be produced. It should be mentioned that in this section only MEC simulation results will be presented.

Shown in Figures 6-26 and 6-27 are the spectra of three nonadjacent and adjacent bar breakages. Similar to the previous section, one should note a good agreement between the values of  $LSB_{2sf}$  in both cases. The same simulation results are evaluated using the MFPO approach in Figures 6-28 and 6-29. Again, from the MFPO results one should note that in both cases fault indices are in close agreement. From this data one can safely conclude that in the case of  $N$  nonadjacent bar breakages each separated from the other by one pole-pitch fault indices corresponding to the adjacent broken bar fault will be produced. Hence, no difficulty associated with diagnosis of the specific number of broken bars in such faults should arise.

In summary, the experimental and simulation results of the various nonadjacent bar breakage patterns have been presented. It has been shown that difficulties may arise when nonadjacent faults separated by half pole-pitch are diagnosed using conventional diagnostics approaches. It has also been shown that secondary saturation effects that appear during such faults can be utilized for diagnostics purposes. On the other hand, it has been verified that in the case of bar breakages separated by a complete pole-pitch, fault indices corresponding to the adjacent fault are produced.

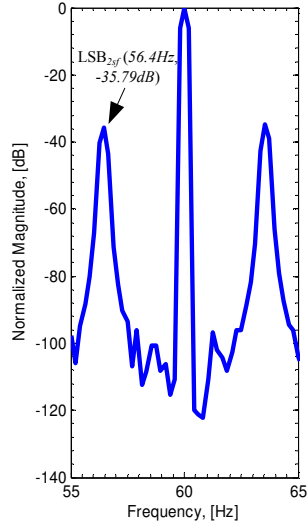


**Figure 6-26.** Current frequency spectrum (MCSA) under conditions of three broken bars separated by one pole-pitch,  $180^\circ$  electrical,  $N=3$ , (from MEC Simulation).

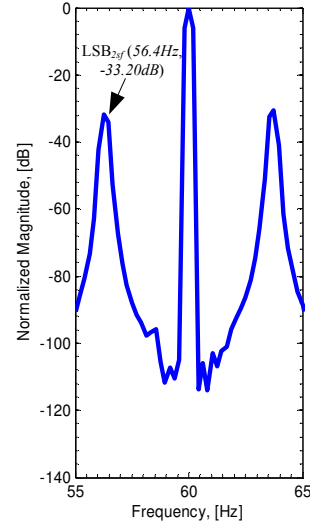


**Figure 6-27.** Current frequency spectrum (MCSA) under conditions of three adjacent broken bars (from MEC Simulation).

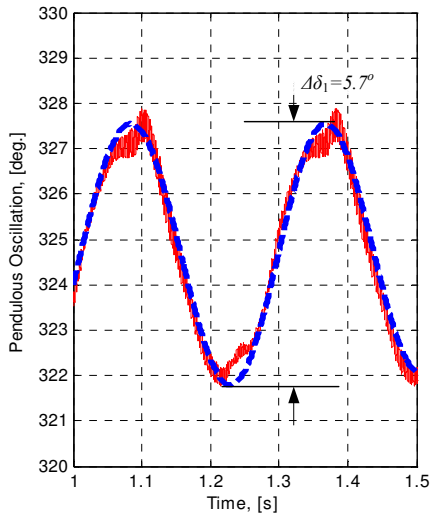


**Figure 6-28.** MFPO under conditions of three broken bars one pole-pitch,  $180^\circ$  electrical,  $N=3$ , (from MEC Simulation).

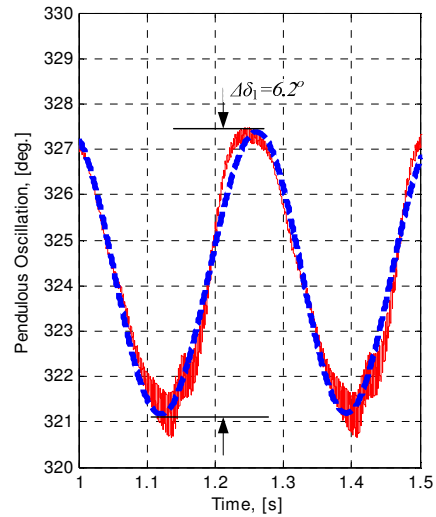


**Figure 6-29.** MFPO under conditions of three adjacent broken bars (from MEC Simulation).

## CHAPTER 7: CONCLUSIONS

---

### 7.1 SUMMARY AND CONCLUSIONS

**I**N this thesis, faults associated with squirrel-cage rotor structures of induction machines have been considered. More specifically, effects of adjacent and nonadjacent bar breakages on rotor fault diagnostics in squirrel-cage induction machines have been studied. It has been shown that nonadjacent bar breakages separated by half a pole-pitch ( $90^\circ$  electrical) result in masking of the commonly used fault indices, hence, leading to possible misdiagnosis of the machine. This masking problem has been addressed and partially solved in this work. Namely, it has been shown that secondary saturation effects resulting from such nonadjacent bar breakages manifest themselves in side-band frequency components at  $(1 \pm 4s)f$  in the frequency spectrum of motor currents, and  $4sf$  frequency components of the magnetic field pendulous oscillation, and vibration/torque. Hence, these secondary saturation effects can be utilized for diagnostics of such faults. At the present moment no statistical data showing the frequency of occurrence of such nonadjacent rotor failures exists. However, one can identify some squirrel-cage designs that may be more prone to such nonadjacent failures. Squirrel-cage rotor structures with a low number of rotor bars per pole, such as the one studied in this thesis, may be at higher risk of being misdiagnosed.

The magnetic equivalent circuit model has been implemented in order to study such nonadjacent bar breakages. This modeling approach has been effectively utilized due to its fast execution time and relatively good accuracy. Again, it has been shown that adjacent rotor bar breakages manifest themselves mainly through oscillation of the rotor mmf, which in turn produces the detectable magnetic field disturbance.

The suitability of application of a simple piezoelectric vibration sensor to motor fault diagnostics has been studied. It has been shown that such piezoelectric sensors can be utilized for rotor fault diagnostics. The vibration signal obtained using a PVDF piezoelectric vibration sensor can be used for fault diagnostics as well as for speed estimation purposes. Moreover, piezoelectric type vibration sensors provide excellent sensitivity and high bandwidth. These properties of piezoelectric vibration sensors can be utilized for diagnostics of faults in other machine components such as: stator winding, motor and load bearings, etc.

## 7.2 RECOMMENDATIONS FOR FUTURE WORK

In this work, a number of nonadjacent rotor failures have been studied. It has been shown that some nonadjacent squirrel-cage rotor failures may be masked, and hence go undetected when conventional diagnostic indices are used. Accordingly, such nonadjacent rotor faults need to be considered further in the development of an effective induction motor diagnostics software/hardware product. It has been shown that piezoelectric vibration sensors can be utilized for diagnostics of both adjacent and nonadjacent squirrel-cage rotor failures. The possibility of application of such sensors to diagnostics of other machine components, such as stator winding short circuits, defects in motor and load bearings, etc., needs to be addressed further in future work in the fault identification and diagnostics area.

## REFERENCES

---

- [1] N. Tesla, "Electro Magnetic Motor," U. S. Patent 381,968, May 1, 1888.
- [2] N. Tesla, "Electro Magnetic Motor," U. S. Patent 382,279, May 1, 1888.
- [3] IEEE Committee Report, "Report of Large Motor Reliability Survey of Industrial and Commercial Installation, Part I and Part II," *IEEE Transactions on Industry Applications*, Vol. 21, pp. 853-872, Jul./Aug. 1985.
- [4] P. F. Albrecht, J. C. Appiarius, and D. K. Sharma, "Assessment of the Reliability of Motors in Utility Applications-Updated," *IEEE Transactions on Energy Conversion*, Vol. 1, pp. 39-46, Dec. 1986.
- [5] M. L. Sin, W. L. Soong, and N. Ertugrul, "Induction Machine On-Line Condition Monitoring and Fault Diagnosis – A Survey," *Australian Universities Power Engineering Conference*, Christchurch, New Zealand, 2003.
- [6] R. R. Schoen, T. G. Habetler, F. Kamran, and R. G. Bartheld, "Motor Bearing Damage Detection Using Stator Current Monitoring," *IEEE Transaction on Industry Applications*, Vol. 31, No. 6, pp.1274-1279, November/December 1995.

- [7] R. Barron, Ed. *Engineering Condition Monitoring Practice, Methods, and Applications*. New York: Addison Wesley Longman Inc., 1996.
- [8] R. Ong, J. H. Dymond, and R. D. Findlay, "Bearing Damage Analysis in a Large Oil-Ring-Lubricated Induction Machine," *IEEE Transactions on Industrial Electronics*, Vol. 47, No. 5, October 2000.
- [9] F. Punga and W. Hess, "Bearing currents," *Elektrotech. Maschin.*, Vol. 25, pp. 615-618, Aug. 1907.
- [10] P. L. Alger and H. M. Samson, "Shaft Currents in Electric Machines," *Transactions of AIEE*, Vol. 43, pp. 235-244, Feb. 1924.
- [11] C.T. Pearce, "Bearing currents—Their Origin and Prevention," *Elect.Journal*, Vol. 24, No. 8, pp. 372-376, Aug. 1927.
- [12] R. F. Schiferl, M. J. Melfi, "Bearing Current Remediation Options," *Industry Application Magazine*, pp. 40-50, July/August 2004.
- [13] D. Busse, J. Erdman, R.J. Kerkman, D. Schlegel, and G. Skibinski, "Bearing currents and their relationship to PWM drives," *Power Electronics, IEEE Transactions on*, Vol.12, No.2, pp.243-252, Mar. 1997.
- [14] Electric Motor Reference, "Induced Bearing Currents, Determining the Problem," July 2007, [http://www.electricmotors.machinedesign.com/guiEdits/Content/bdeee11/bdeee11\\_5-1.aspx](http://www.electricmotors.machinedesign.com/guiEdits/Content/bdeee11/bdeee11_5-1.aspx).
- [15] H. E. Boyanton, and G. Hodges, "Bearing Fluting," *Industry Applications Magazine*, September/October 2002.
- [16] S. Bell, T. J. Cookson, S. A. Cope, R. A. Epperly, A. Fischer, D. W. Schlegel, and G. L. Skibinsky, "Experience With Variable-Frequency Drives and Motor Bearing Reliability,"

- IEEE Transactions on Industry Applications*, Vol. 37, No. 5, pp.1438-1446, September/October 2001.
- [17] E. Wiedenbrug, G. Frey, and J. Wilson, "Early Intervention: Impulse Testing and Turn Insulation Deterioration in Electric Motors" *IEEE Transactions on Industry Applications*, Vol. 37, No. 5, pp. 34-40, September/October 2004.
- [18] N. A. O. Demerdash, "Electrical Transients and Surges in Power Systems and Devices" class notes for EECE 187, Department of Electrical and Computer Engineering, Marquette University, Milwaukee, Wisconsin, Fall 2006.
- [19] M. Fenger, S. R. Campbell, and J. Pedersen, "Motor Winding Problems Caused by Inverter Drives," *Industry Applications Magazine*, pp. 22-31, July/August 2003.
- [20] A. H. Bonnett and G. C. Soukup, "Cause and Analysis of Stator and Rotor Failures in Three-Phase Squirrel-Cage Induction Motors," *IEEE Transactions on Industry Applications*, Vol. 28, No. 4, pp.22-42, July/August 1992.
- [21] M. Melfi, A. M. Jason Sung, S. Bell, and G. L. Skibinski, "Effects of Surge Voltage Risetime on the Insulation of Low-Voltage Machines Fed by PWM Converters," *IEEE Transactions on Industry Applications*, Vol. 34, No. 4, pp.766-775, July/August 1998.
- [22] ANSI/IEEE Std. 43-1974, IEEE Recommended Practice for Testing Insulation Resistance of Rotating Machinery.
- [23] ANSI/IEEE Std. 433-1974, IEEE Recommended Practice of Large AC Rotating Machinery with High Voltage at Very Low Frequency.
- [24] S. Nandi and H. A. Toliyat, "Novel Frequency-Domain-Based Technique to Detect Stator Interturn Faults in Induction Machines Using Stator-Induced Voltages After Switch-Off" *IEEE Transactions on Industry Applications*, Vol. 38, No. 1, pp. 101-109, January/February 2002.

- [25] W. T. Thomson, "On-Line MCSA to Diagnose Shorted Turns in Low Voltage Stator Windings of 3-Phase Induction Motors Prior to Failure," *Electric Machines and Drives Conference, 2001. IEMDC 2001. IEEE International*, Vol., No., pp. 891-898, 2001.
- [26] J. Sottile and J. L. Kohler, "An On-Line Method to Detect Incipient Failure of Turn Insulation In Random-Wound Motors," *IEEE Transactions on Energy Conversion*, Vol.8, No.4, December 1993.
- [27] B. Mirafzal, R. J. Povinelli, and N. A. O. Demerdash, "Interturn Fault Diagnosis in Induction Motors Using the Pendulous Oscillation Phenomenon," *IEEE Transactions on Industry Applications*, Vol. 21, No. 4, pp.871-882, December 2006.
- [28] M. A. Awadallah and M. M. Morcos, "Application of AI Tools in Fault Diagnosis of Electrical Machines and Drives – An Overview," *IEEE Transactions on Energy Conversion*, Vol.18, No.2, pp. 245-251, December 2003.
- [29] Ahmed Sayed-Ahmed, Chia-Chou Yeh, B. Mirafzal, and N.A.O. Demerdash, "Analysis of Stator Winding Inter-Turn Short-Circuit Faults in Induction Machines for Identification of the Faulty Phase," *2006. 41st IAS Annual Meeting. Conference Record of the 2006 IEEE*, Vol.3, No., pp.1519-1524, 8-12 Oct. 2006.
- [30] Ahmed Sayed-Ahmed, G. Y. Sizov, and N. A. O. Demerdash, "Diagnosis of Inter-Turn Short Circuit for a Polyphase Induction Motor in Closed-Loop Vector-Controlled Drives," accepted for presentation/publication at 42<sup>nd</sup> IAS Annual Meeting.
- [31] J. Penman, H. G. Sadding, B. A. Lloyd, and W. T. Fink, "Detection and Location of Interturn Short Circuits in the Stator Windings of Operation Motors," *IEEE Transactions on Energy Conversion*, Vol. 9, No. 4, December 1994.

- [32] A. H. Bonnett and G. C. Soukup, "Analysis of Rotor Failures in Squirrel-Cage Induction Motors," *IEEE Transactions on Industry Applications*, Vol. 24, No. 6, pp.1124-1130, November/December 1988.
- [33] I. D. Lomax, "Assessment of Induction Motor Cage Fatigue Life," *Electrical Machines and Drives, 1991. Fifth International Conference on (Conf. Publ. No. 341)*, pp.281-284, 11-13 Sep 1991.
- [34] J. F. Bangura and N. A. O. Demerdash, "Effects of Broken Bars/End-Ring Connectors and Airgap Eccentricities on Ohmic and Core Losses of Induction Motors in ASD's Using a Coupled Finite Element-State Space Method," *IEEE Transactions on Energy Conversion*, Vol. 15, No. 1, pp. 40-47, March 2000.
- [35] R. Carlson, "Inter-Bar Currents in the Rotor of Large Three-Phase Cage Induction Motors: Analysis and Detection," *Symposium on Diagnostics for Electric Machines, Power Electronics and Drives (SDEMPED 2003)*, August 2003.
- [36] A. H. Bonnett and T. Albers, "Squirrel-Cage Rotor Options for AC Induction Motors," *IEEE Transactions on Industry Applications*, Vol. 37, No. 4, July/August 2001.
- [37] J. S. Hsu, "Monitoring of Defects in Induction Motors Through Air-Gap Torque Observation," *IEEE Transactions on Industry Applications*, Vol. 31, No. 5, September/October 1995.
- [38] G. B. Kliman and R. A. Koegl, "Noninvasive Detection of Broken Rotor Bars in Operating Induction Motors," *IEEE Transactions on Energy Conversion*, Vol. 3, No. 4, pp. 873-879, December 1988.
- [39] W. T. Thomson and I. D. Stewart, "On-Line Current Monitoring for Fault Diagnosis in Inverter Fed Induction Motors," *IEE Third International Conference on Power Electronics and Drives, London*, pp. 432-435, 1988.

- [40] W. T. Thomson and M. Fenger, "Current Signature Analysis to Detect Induction Motor Faults," *Industry Applications Magazine*, pp. 26-34, July/August 2001.
- [41] M. Benbouzid, M. Vieira, and Celine Theys, "Induction Motors' Fault Detection and Localization Using Stator Current Advanced Signal Processing Techniques," *IEEE Transactions on Power Electronics*, Vol. 14, No. 1, pp. 14-22, January 1999.
- [42] M. Benbouzid and G. B. Kliman, "What Stator Current Processing-Based Technique to Use for Induction Motor Rotor Fault Diagnosis?," *IEEE Transactions on Energy Conversion*, Vol. 18, No. 2, pp. 238-244, June 2003.
- [43] B. Mirafzal and N. A. O. Demerdash, "On Innovative Methods of Induction Motor Interturn and Broken-Bar Fault Diagnostics," *IEEE Transactions on Industry Applications*, Vol. 42, No. 2, pp. 762-769, March/April 2006.
- [44] B. Mirafzal and N. A. O. Demerdash, "Effects of Load Magnitude on Diagnosing Broken Bar Faults in Induction Motors Using the Pendulous Oscillation of the Rotor Magnetic Field Orientation," *IEEE Transactions on Industry Applications*, Vol. 41, No. 3, pp. 771-773, May/June 2005.
- [45] B. Mirafzal and N. A. O. Demerdash, "Induction Motor Broken-Bar Fault Diagnosis Using the Rotor Magnetic Field Space-Vector Orientation," *IEEE Transactions on Industry Applications*, Vol. 40, No. 2, pp. 534-542, March/April 2004.
- [46] B. Mirafzal, "Incipient Fault Diagnosis in Squirrel-Cage Induction Motors," Ph.D. dissertation, Marquette University, Milwaukee, Wisconsin, USA, August 2005.
- [47] C. Kral, F. Pirker, and G. Pascoli, "Model-Based Detection of Rotor Faults Without Rotor Position Sensor - The Sensorless Vienna Monitoring Method," *IEEE Transactions on Industry Applications*, Vol. 41, No. 3, pp. 784-789, May/June 2005.

- [48] C. Kral, R. S. Wieser, F. Pirker, and M. Schagginger, "Sequences of Field-Oriented Control for the Detection of Faulty Rotor Bars in Induction Machines – The Vienna Monitoring Method," *IEEE Transactions on Industry Electronics*, Vol. 47, No. 5, pp. 1042-1050, October 2000.
- [49] N. M. Elkasabgy, A. R. Eastham, and G. E. Dawson, "Detection of Broken Bars in the Cage Rotor on an Induction Machine," *IEEE Transactions on Industry Applications*, Vol. 28, No. 1, pp. 165-171, January/February 1992.
- [50] P. N. Dobrodeyev, S. A. Volokhov, A. V. Kildishev, and J. A. Nyenhuis, "Method for Detection of Broken Bars in Induction Motors," *IEEE Transactions on Magnetics*, Vol. 36, No. 5, pp. 3608-3610, September 2000.
- [51] J. S. Hsu, "Monitoring of Defects in Induction Motors Through Air-Gap Torque Observation," *IEEE Transactions on Industry Applications*, Vol. 31, No. 5, September/October 1995.
- [52] A. M. da Silva, R. J. Povinelli, and N. A. O. Demerdash, "Induction Machine Broken Bar and Stator Short-Circuit Fault Diagnostics Based on Three Phase Stator Current Envelopes," *IEEE Transactions on Industrial Electronics*, (in press).
- [53] N. A. O. Demerdash, "Advanced Electric Machines" class notes for EECE 281, Department of Electrical and Computer Engineering, Marquette University, Milwaukee, Wisconsin, Spring 2007.
- [54] N. A. O. Demerdash, "Advanced Concepts in Analysis and Design of Electric Machines and Drives" class notes for EECE 285, Department of Electrical and Computer Engineering, Marquette University, Milwaukee, Wisconsin, Spring 2006.
- [55] A. E. Fitzgerald, C. Kingsley, S. D. Umans, *Electric Machinery*. 6<sup>th</sup> Edition, New York, McGraw-Hill, 2003.

- [56] M. G. Say, *Alternating Current Machines*. New York, John Wiley and Sons, 1976.
- [57] P. L. Alger, *Induction Machine: Their Behavior and Uses*. 2<sup>nd</sup> Edition, Switzerland, Gordon and Breach Science Publishers SA, 1995.
- [58] A. S. Langsdorf, *Theory of Alternating Current Machinery*. 2<sup>nd</sup> Edition, New Delhi, McGraw-Hill, 1974.
- [59] P. C. Krause and O. Wasynczuk, *Electromechanical Motion Devices*. New York, McGraw-Hill, 1989.
- [60] M. L. Barnes and C. A. Gross, "Comparison of Induction Machine Equivalent Circuit Models, *System Theory, 1995*., *Proceedings of the Twenty-Seventh Southeastern Symposium on*, pp.14-17, 12-14 Mar 1995.
- [61] H. A. Toliyat and T. A. Lipo, "Transient Analysis of Cage Induction Machines Under Stator, Rotor, Bar and End Ring Faults," *IEEE Transactions on Energy Conversion*, Vol. 10, No. 2, pp.241-247, June 1995.
- [62] X. Luo, Y. Liao, H. A. Toliyat, A. El-Antably, and T. A. Lipo, "Multiple Coupled Circuit Modeling of Induction Machines," *IEEE Transactions on Industry Applications*, Vol. 31, No. 2, pp.203-210, March/April 1995.
- [63] A. R. Munoz and T. A. Lipo, "Complex Vector Model of the Squirrel-Cage Induction Machine Including Instantaneous Rotor Bar Currents," *IEEE Transactions on Industry Applications*, Vol. 35, No. 6, pp.57-64, November/December 1999.
- [64] B. Mirafzal and R. J. Povinelli, and N. A. O. Demerdash, "Interturn Fault Diagnosis in Induction Motors Using the Pendulous Oscillation Phenomenon," *IEEE Transactions on Energy Conversion*, Vol. 21, No. 4, pp.871-882, December 2006.

- [65] G. Bossio, C. De Angelo, J. Solsona, G. Garcia, and M. I. Valla, "A 2-D Model of the Induction Machine: An Extension of the Modified Winding Function Approach," *IEEE Transactions on Energy Conversion*, Vol. 19, No. 1, March 2004.
- [66] S. Nandi, "A Detailed Model of Induction Machines with Saturation Extendable for Fault Analysis," *IEEE Transactions on Industry Applications*, Vol. 40, No. 5, September/October 2004.
- [67] V. Ostovic "A Method For Evaluation of Transient and Steady State Performance in Saturated Squirrel-Cage Induction Machines," *IEEE Transactions on Energy Conversion*, Vol. EC-1, No. 3, September 1986.
- [68] V. Ostovic, *Dynamics of Saturated Electric Machines*. New York, Springer-Verlag, 1989.
- [69] V. Ostovic, "Magnetic Equivalent Circuit Presentation of Electric Machines," *Electric Machines and Power Systems*, Vol. 12, pp. 407-437, June 1987.
- [70] V. Ostovic "A Simplified Approach to Magnetic Equivalent-Circuit Modeling of Induction Machines," *IEEE Transactions on Industrial Applications*, Vol. 24, No. 2, March/April 1988.
- [71] C. Delforge and B. Lemaire-Semail, "Induction Machine Modeling Using Finite Element and Permeance Network Methods," *IEEE Transactions on Magnetics*, Vol. 31, No. 3, May 1995.
- [72] P. M. Leplat, B. Lemaire-Semail, S. Clenet, and F. Piriou, "Comparison between finite element method and magnetic equivalent scheme to model an induction machine," *COMPEL: The International Journal for Computation and Mathematics in Electrical and Electronic Engineering*, Vol. 15, No. 4, pp. 82-87, 1996.

- [73] H. Meshgin-Kelk, J. Milimonfared, and H. A. Toliyat, "Interbar Currents and Axial Fluxes in Healthy and Faulty Induction Motors," *IEEE Transactions on Industry Applications*, Vol. 40, No. 1, January/February 2004.
- [74] S. D. Sudhoff, B. T. Kuhn, K. A. Corzine, and B. T. Branecky, "Magnetic Equivalent Circuit Modeling of Induction Motors," *IEEE Transactions on Energy Conversion*, Vol. 22, No. 2, June 2007.
- [75] N. A. O. Demerdash, "Computer-Aided Field Calculations in Electrical Engineering Using Finite Elements" class notes for EECE 396, Department of Electrical and Computer Engineering, Marquette University, Milwaukee, Wisconsin, Spring 2006.
- [76] J. Pedro, A. Bastos, and N. Sadowski, *Electromagnetic Modeling by Finite Element Methods*. New York, Marcel Dekker, Inc., 2003.
- [77] J. F. Bangura, "Diagnosis of Normal and Abnormal Operations of Induction Motors in ASDS by a Coupled Finite Element-Network Technique," Ph.D. dissertation, Marquette University, Milwaukee, Wisconsin, USA, August 1999.
- [78] Measurement Specialties, *Piezo Film Sensors Technical Manual*, Measurement Specialties, Inc., Rev. B.
- [79] J. Kymissis, C. Kendall, J. Paradiso, and N. Gershenfeld, "Parasitic Power Harvesting in Shoes," *Proc. of the Second IEEE International Conference on Wearable Computing, (ISWC)*, IEEE Computer Society Press, pp. 132-139, October 1998.
- [80] A. Katz, "Residential Piezoelectric Energy Sources," Delta Smart House, Duke University, July 21, 2004.
- [81] P. Beccue, J. Neely, S. Pekarek, and D. Stutts, "Utilization of a Piezoelectric Polymer to Sense Harmonics of Electromagnetic Torque," *IEEE Power Electronics Letters*, Vol. 1, No. 3, September 2003.

- 
- [82] P. Beccue, J. Neely, S. Pekarek, and D. Stutts, "Measurement and Control of Torque Ripple-Induced Frame Torsional Vibration in a Surface Mount Permanent Magnet Machine," *IEEE Transactions on Power Electronics*, Vol. 20, No. 1, January 2005.
- [83] S. Pekarek and P. Beccue, "Using Torque-Ripple-Induced Vibration to Determine the Initial Rotor Position of a Permanent Magnet Synchronous Machine," *IEEE Transactions on Power Electronics*, Vol. 21, No. 3, May 2006.
- [84] D. Wu and S. D. Pekarek, "Using Mechanical Vibration to Estimate Rotor Speed in Induction Motor Drives," *2007 IEEE PESC Power Electronics Specialist Conference Proceedings*, pp. 2412-2417, Orlando, Florida, June 2007.
- [85] Measurement Specialties Application Note No. 01800004-000, *Interfacing Piezo Film Electronics*, Measurement Specialties, Inc., Rev. B., March 2006.
- [86] National Semiconductor Data Sheet, *TL082 Wide Bandwidth Dual J-FET Input Operational Amplifier*, August 2000.
- [87] Measurement Specialties Application Note No. 111398, *LDT0 Solid State Switch/Vibration Sensor*, Measurement Specialties, Inc., Rev. O.

## APPENDIX: MEC PARAMETER CALCULATION

---

### A.1 RESISTANCES

Stator phase resistance,  $r_s$ , can be calculated based on the knowledge of the cross-section, length, and resistivity of the type of wire used in a stator winding. For this case study motor the stator phase resistance has been calculated as follows:

$$r_s = \rho_{Cu} \left( \frac{L_{wire / phase}}{A_{wire}} \right) = 1.342 \Omega / \text{phase} \quad (\text{A.1})$$

Considering a simplified rotor slot cross-section of Figure A-1 the dc rotor bar resistance can be estimated as shown in (A.2). Similarly, the resistance of the part of the end ring connecting two bars can be estimated as given in (A.3):

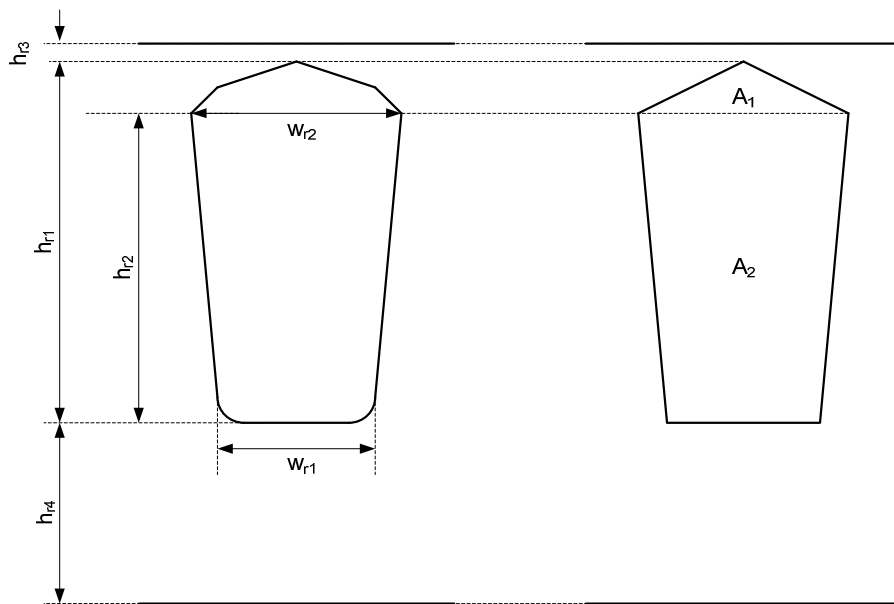


**Figure A-1.** Rotor slot cross-section.

$$r_{dc} = \rho_{Al} \left( \frac{L_{bar}}{A_1 + A_2} \right) = 57.1 \mu\Omega \quad (\text{A.2})$$

$$r_{er} = \rho_{Al} \left( \frac{L}{A} \right) = 3.2 \mu\Omega \quad (\text{A.3})$$

where,  $A_1$  and  $A_2$  are defined in Figure A-1,  $L_{bar}$ , is the axial length of the bar,  $\rho_{Al}$ , is the resistivity of aluminum, while  $A$  and  $L$  are the cross-sectional area of the end-ring and the length between the adjacent bars, respectively. It should be noted that resistivity values of copper and aluminum used in the above calculations are based on the measurements at room temperature of 25°C.

## A.2 RELUCTANCES/PERMEANCES

Based on Figure A-2 it should be noticed that the air gap permeance is a function of the rotor and stator teeth overlap area, which in turn is a function of rotor position. Hence, the air gap permeance of a pair of stator and rotor teeth can be modeled as shown in Figure A-3. As has been shown in [68] in a real situation the air gap permeance is a smoother function of the rotor position angle than the one shown in A-3 because of the fringing flux that exists between a pair of stator and rotor teeth. This can also be explained by the fact that mmf is not constant along the length of the tooth tip.

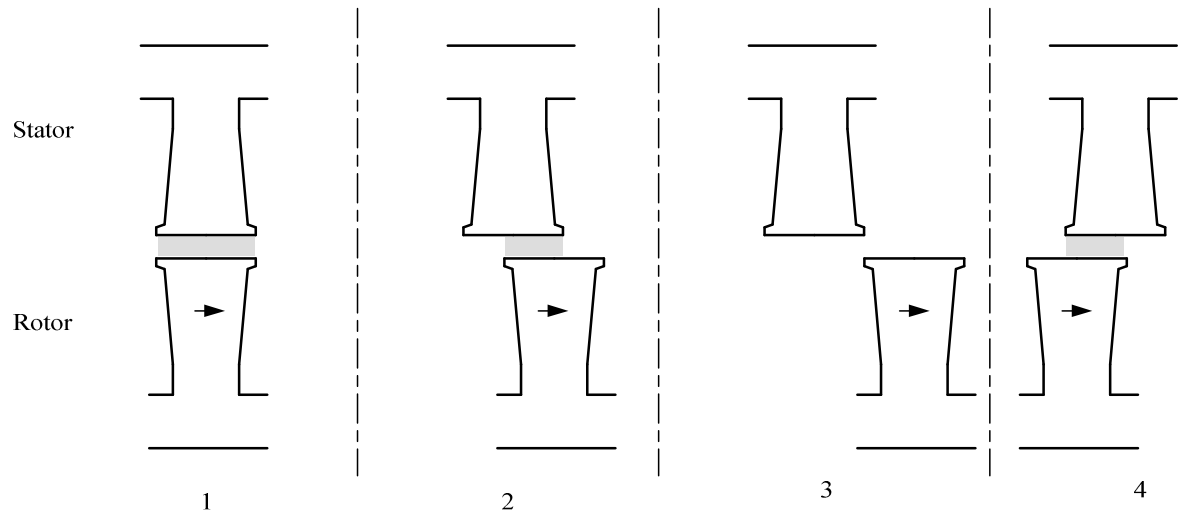


**Figure A-2.** Stator and rotor teeth relative position and overlap area.

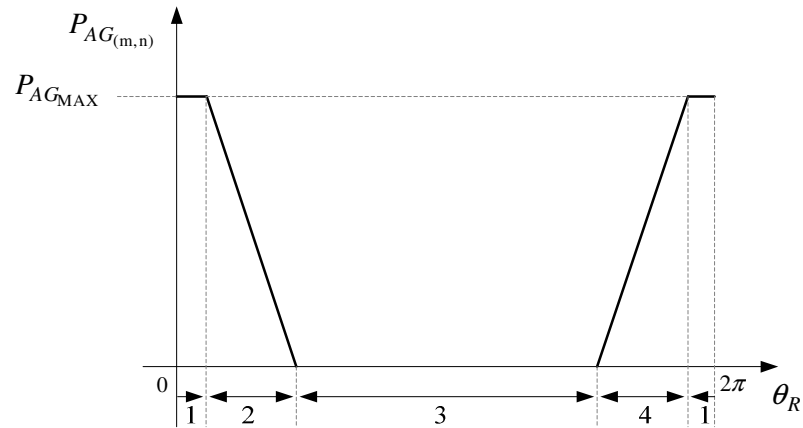


**Figure A-3.** Air gap permeance for a pair of stator and rotor teeth.

This smoothing effect can be approximated by taking only the first two terms of the Fourier series in  $P_{AG(m,n)}$  and is depicted in A-4.

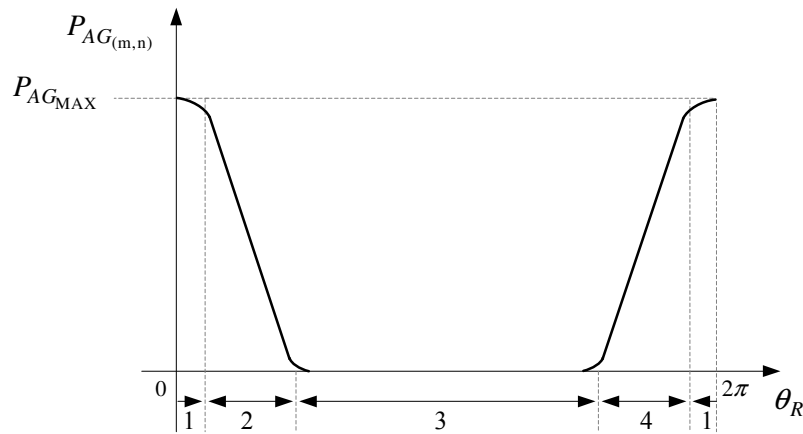


**Figure A-4.** Smoothed air gap permeance for a pair of stator and rotor teeth.

It should also be mentioned that the skewing effect can be modeled by including it in the air gap permeance function as has been done in [68].

Based on the simplified cross-section of a stator slot depicted in Figure A-5 one can redraw stator teeth as shown in Figure A-6.

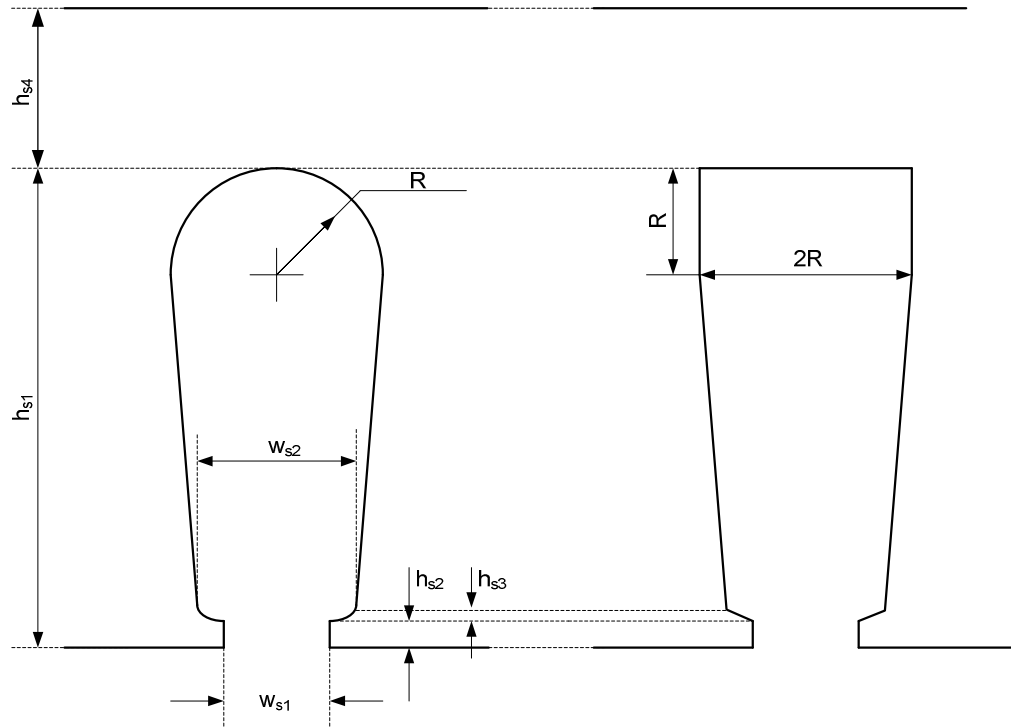


Figure A-5. Stator slot with dimensions.

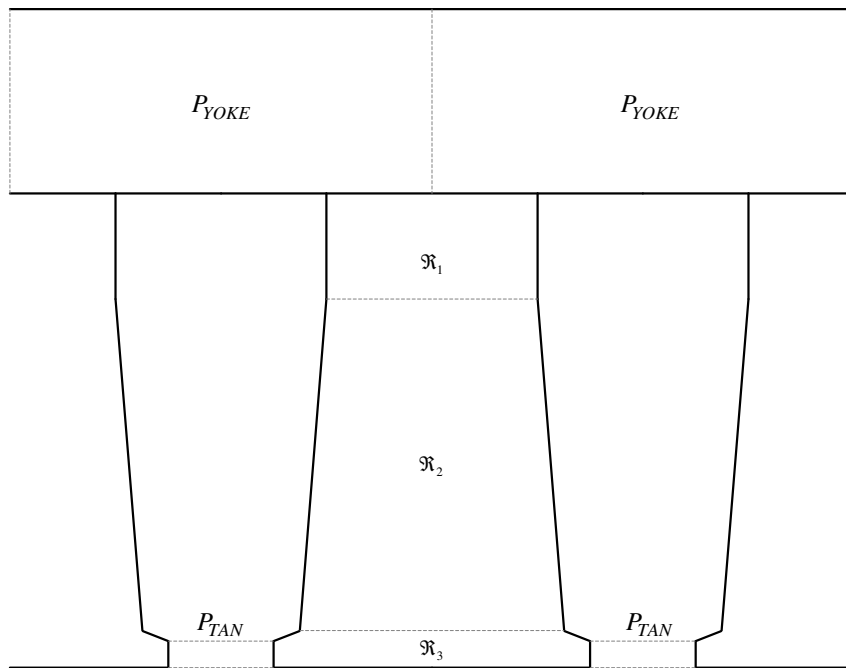


Figure A-6. Stator tooth with various reluctances and permeances.

From A-6 it should be observed that the stator core consists of permeances of two shapes. Stator backiron/yoke permeances,  $P_{YOKE}$ , tangential leakages,  $P_{TAN}$ , and the reluctance of top teeth sections,  $\mathfrak{R}_1$ , can be approximated by rectangular blocks depicted in Figure A-7. Meanwhile, the stator teeth sections  $\mathfrak{R}_2$  and  $\mathfrak{R}_3$  can be approximated by trapezoidal blocks shown in A-8.

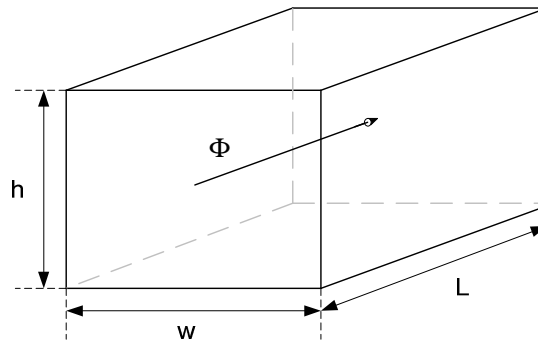


Figure A-7. Rectangular permeance block.

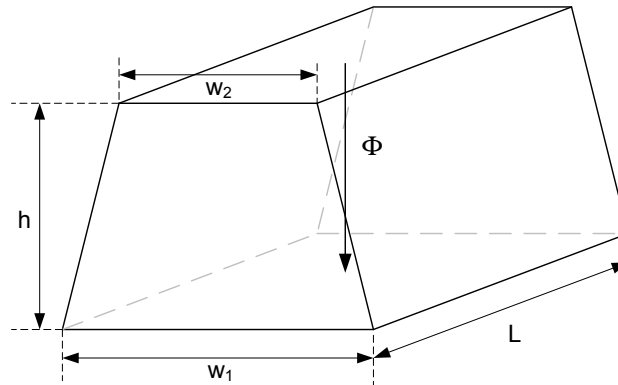


Figure A-8. Trapezoidal permeance block.

Permeance of the rectangular blocks shown in A-7 can be calculated using (A.4)

$$P = \mu_o \mu_R \left( \frac{wh}{L} \right) \tag{A.4}$$

Reluctances of the regions approximated by trapezoidal shapes can be calculated using the following:

$$\mathfrak{R} = \frac{1}{\mu_o \mu_R} \left( \frac{h}{L(w_2 - w_1)} \right) \ln \left( \frac{w_2}{w_1} \right) \quad (\text{A.5}).$$

The parameters of the case-study 5-hp squirrel cage induction machine used in this investigation and associated model are summarized in table T-A-1. It should be noted that if saturation of the magnetic material does not need to be considered, the value of relative permeability,  $\mu_R$ , in linear region of the B-H curve can be used for parameter calculation. For this machine this value has been approximated as  $\mu_{R_{LIN}} = 11000$ .

	STATOR	ROTOR
STATOR RESISTANCE, $r_s$ , [ $\Omega$ /phase]	1.342	
ROTOR DC BAR RESISTANCE, $r_{dc}$ , [ $\mu\Omega$ ]		57.1
ROTOR END RING RESISTANCE, $r_{er}$ , [ $\mu\Omega$ ]		3.2
TOOTH RELUCTANCE, $\mathfrak{R}$ , [ $H^{-1}$ ]	$(2.70787 \times 10^7) / \mu_R$	$(2.689137 \times 10^7) / \mu_R$
TANGENTIAL LEAKAGE PERMEANCE, $P_{TAN}$ , [H]	$4.44 \times 10^{-7}$	$2.7 \times 10^{-7}$
YOKE PERMEANCE, $P_{YOKE}$ , [H]	$\mu_R (1.266 \times 10^{-3})$	$\mu_R (1.2 \times 10^{-2})$

**T-A-1.** MEC model parameters of the 5-hp induction motor.